The Pennsylvania State University

The Graduate School

John and Willie Leone Family Department of Energy and Mineral Engineering

FUNDAMENTAL INVESTIGATION OF GAS STORAGE AND TRANSPORT IN SHALES

A Dissertation in

Energy and Mineral Engineering

by

Nirjhor Chakraborty

Submitted in Partial Fulfillment

of the Requirements

for the Degree of

Doctor of Philosophy

May 2019

The dissertation of Nirjhor Chakraborty was reviewed and approved* by the following:

Zuleima Karpyn

Professor of Petroleum and Natural Gas Engineering
Quentin E. and Louise L. Wood Faculty Fellow in Petroleum and Natural Gas Engineering
Dissertation Adviser
Chair of Committee

Shimin Liu

Associate Professor of Energy and Mineral Engineering

Hamid Emami-Meybodi

Assistant Professor of Energy and Mineral Engineering

Michael Charles Hillman

L. Robert and Mary L. Kimball Assistant Professor
Civil and Environmental Engineering Department

Luis F. Ayala H.

Professor of Petroleum and Natural Gas Engineering
Associate Department Head for Graduate Education

*Signatures are on file in the Graduate School

Abstract

Gas storage and transport in shales is very different from sandstones or limestones. This is not only due to their inherently lower porosity and substantially lower permeability, but also because more complex and fundamentally different physical mechanistic phenomena govern both storage and transport. We use gas injection porosimetry to measure the storage of several single-component gases at supercritical pressures and temperatures on whole core plugs of Marcellus, Haynesville, Mancos, and Bakken shales. We find that the storage capacities of all gases far exceed helium storage in most shales. This is indicative of densification of gas that is taken up by the samples. Possible mechanisms for this densification such as confinement induced-supercriticality, adsorption, and capillary condensation are evaluated and the case for each is presented. Assuming the excess storage, beyond helium derived pore or free-gas volumes, is adsorption, adsorbed methane gas is found to account for between 12-75% of total gas-in-place (GIP) and is more than 40% of GIP in most cases. Despite being a noble gas, argon storage is found to be almost the same as methane. Ethylene gas storage in the Marcellus sample is found to be over 96% of GIP. Closer analysis of the data in conjunction with pore surface area estimates from LPSA measurements indicates a multilayer adsorption mechanism. This raises questions on the applicability of the Langmuir monolayer-model to describe storage in shales. Compositional and textural characterization indicates that organic content is a moderately important factor controlling gas storage behavior. However, three-dimensional spatial maps indicate that high storage is not limited to organic-rich regions. Pore size, rather than composition, appears to be a better predictor of storage behavior, with storage being proportional to the prevalence of nanopores and to total pore surface area. Gas transport in shale is also multi-mechanistic and cannot be separated from the underlying storage mechanisms. A numerical model is developed accounting for free-gas and adsorbed-phase diffusion, as well as adsorption-desorption kinetics. The model is validated on dynamic in-situ gas concentration data obtained via x-ray CT imaging of the Marcellus Shale. Modeling results suggest that concentration-dependent surface diffusion is the dominant mechanism controlling gas transport in the Marcellus. It is observed that the surface diffusion coefficient can exceed the free-gas diffusion coefficient by up to ten times.

Table of Contents

List of Figures

List of Tables

Acknowledgements

Five years, seven months and two weeks is how long, as of this writing, Penn State has been home. As someone who moved every couple of years as a child, this is where I have now spent the most time and grown some of my deepest roots. Thank you, dear old State, for a most beautiful experience, and the numerous important life lessons.

My advisor, Professor Zuleima Karpyn, more than anyone else has exemplified the welcoming, encouraging, and supportive spirit at Penn State that is needed to bring out the best in people. Her guidance, patience, and ability to foster calm were absolutely critical to keep me going through the most difficult portions of my graduate studies. It has been a privilege to work with her.

My Ph.D. research may have taken a lot longer without Dr. Phil Halleck. I met Dr. Halleck only a few times, but those occasions were a massive download of years of technical and non-technical wisdom essential to my Ph.D. work. His vast knowledge and specific inputs on X-ray CT technology are fundamental to this work. His perspective on grad school also helped me approach my Ph.D. with maturity for which I will always be grateful.

Tim Stecko, resident genius, has been an inspiration. He is a polymath and I am incredibly privileged to have had the chance to work with him, to observe his ways of solving problems, and to learn from him. I have asked him to document his wonderful, eclectic invention ideas, and little lab gadgets and tools because I do believe that very many are likely to be substantially useful outside the original scope of his inventions. His humility, hard work, and willingness to help, is something I will try to emulate.

I would like to extend my deep gratitude to Professor Luis Ayala and Dr. Miao Zhang for their time and technical input on numerical simulations, as well as to Dr. Tim Ryan of the Department of Anthropology for his help with 3D image processing. I'd like to thank my committee Dr. Liu, Dr. Emami-Meybodi and Dr. Hillman for their valuable inputs in improving this research.

I am deeply grateful to my best friend and partner for the last four years, Dr. Madhu Singh for her immense support, not just emotionally but also for her practical, intellectual, and logistical help with my research. As my human 'leak-detector' in lab, as a patient sounding board to my difficulties, and as an active partner in problem-solving, her contributions to this research must be acknowledged.

I regret that I cannot name all my teachers, friends, and colleagues about whom I'd have to write a book longer than this document to describe all the love and support received. Thank you for your friendship and for welcoming me into your homes, families and your hearts.

Lastly, I must thank my family – my father, mother, and grandfather, for keeping me going with their unending reservoir of faith in me. Perhaps most importantly, I'd like to thank my father for his vision and many sacrifices made so that I would come to Penn State. I cannot repay this debt but I will strive to pay it forward.

Acknowledgement of Financial and Material Support

This work received funding support from the U.S. Department of Energy, the Office of Science, Basic Energy Sciences program under Award Number DE-SC0006883. Sandia National Laboratories is a multi-program laboratory managed and operated by Sandia Corporation, a wholly owned subsidiary of Lockheed Martin Corporation, for the U.S. Department of Energy's National Nuclear Security Administration under contract DE-AC04 94AL85000. Support from Tim Beattie of Shell Appalachia, and the Unconventional Natural Resources Consortium (UNRC) is gratefully acknowledged for facilitating Marcellus shale samples for this study. The contribution of Bakken shale samples for this study by Hess Corp is also gratefully acknowledged.

Introduction

Problem Statement

The resource base of natural gas from shale reservoirs is enormous, with proven reserves of 464.3tcf in the United States, according to the US Energy Information Agency (EIA) (November, 2018). At 16.86tcf, shale gas production accounted for 62% of domestic natural gas production in 2017 and helped the US meet its entire domestic demand. The importance of shale is only going to grow as the US positions itself as a net exporter of gas in the decades to come (EIA Annual Energy Outlook 2019). However, recovery efficiencies remain low at about 10%, and production strategies that prove successful in one shale do not translate well to other shales (Seales, Ertekin, and Wang 2017; King 2010).

Gas storage in shales is fundamentally different and more complex than in conventional sandstones or limestones. Where gas storage in conventional rocks is a simple function of pore volume and pressure, adsorption is thought to play an important role in shale (Ambrose et al. 2010; Clarkson et al. 2016). However, given the low organic content of shales some researchers claim adsorption levels are both low as well as insignificant from a commercial production point of view (Vega, Dutta, and Kovscek 2013; Heller and Zoback 2014; Seales, Ertekin, and Wang 2017). On the other hand, recent work by Wang et al. (2017) reported that adsorbed gas could account for up to 80% of Gas-In-Place (GIP) in Barnett shale samples for pressures up 13.8MPa [2000psi]. Xiong et al. (2016) collated the results from a series of adsorption studies on different shales and found that adsorbed gas accounted for between 20-85% of GIP.

Given the substantial presence of pores in the nanometer range, other physical phenomenon such as bubble point suppression (Nojabaei, Johns, and Chu 2013; Pathak et al. 2017; Kamari, Li, and Sheng 2018), induced-supercriticality (Luo, Lutkenhaus, and Nasrabadi 2016), and general differences in fluid phase behavior (Jin and Firoozabadi 2016) may also affect both gas storage and transport in many shales. However, all too often the industrial petrophysical analysis of shales remains restricted to porosity and permeability estimations, which are unlikely to

meaningfully describe storage and transport behavior in shales as effectively as they do for conventional rocks.

Most studies on the process of gas storage in shales haven't been comprehensive. Some studies focus on investigating storage behaviors in shale surrogates such as nano-porous silica-glass (e.g., Parsa, Yin, and Ozkan 2015; Luo, Lutkenhaus, and Nasrabadi 2016). Other studies with actual shale specimens tend to measure either only adsorption of hydrocarbon gases or CO_2 (e.g., Busch et al. 2008; Kang et al. 2011), or, only helium pore volumes. What is missing is efforts to observe storage behaviors of different types of gases in shale specimens and connect observations with fabric characteristics.

Numerical models that attempt to describe gas transport in shale also need to account for the multi-mechanistic nature of flow in nanoporous media, as well as the peculiarities of gas storage. Models of this type include the Dusty Gas Model (Mason and Malinauskas 1983), the coupled viscous flow and diffusion model of Ertekin et al. (1986), and the diffusion based model of Fathi and Akkutlu (2012) that also accounts for non-linear sorption kinetics. However, most of these models are validated using pressure and rate data that are only indirect indicators of underlying storage and transport mechanics. There is a lack of good quality experimental data, especially of transient in-situ gas concentrations, to constrain and rigorously validate these models.

Although the gases of broad interest in the context of shales are hydrocarbons for production and CO_2 for EOR/sequestration, the understanding of gas storage in shales is, in general, incomplete. How different gases behave in the nano-porous environment of natural shales is an open research question. The answer to this is inextricably linked with rock properties and needs a more detailed description of the rock composition and texture than is typically undertaken. Finally, storage and transport behaviors go hand-in-hand and description of transport requires a clear understanding of what the dominant storage and transport mechanisms are in a given shale system.

Research Objectives

The purpose of this research is to investigate the fundamentals of gas storage and transport in shales through both experimental and numerical means. The first three chapters are predominantly experimental and focused on gas storage behavior, while the fourth is predominantly numerical and focused on transport behavior. Specific research goals are as follows,

1. *Investigate the mechanics of storage of different types of gases in shales.*
2. *Investigate the relationship between gas storage characteristics and physical and compositional characteristics of different shales.*
3. *Explore the consequences of complex gas storage behavior on transport behavior.*

1: Storage of Real Gases (Part 1): Storage Capacities

1.1 Background

The study of gas storage in shales has historically evolved out of the understanding of gas storage in conventional sandstone and limestone reservoirs, which essentially expects 'free gas' in the pore space of the reservoir rock. However, since the early 1980s several studies have estimated that more than 50% of gas storage in shales is, in fact, adsorbed gas (Lu, Li, and Watson 1995; Lane, Watson, and Lancaster 1989). An example of such a study is Lane *et. al* (1989) who used production data analysis from 8 Devonian shale fields and estimated that on average around 85% gas-in-place (GIP) as being adsorbed.

Since then, the role of adsorption has been a major point of debate in industry and the research community. The experience and learning of the coalbed methane community has been an important source of understanding gas adsorption in shales. However, shales are fundamentally different from coals in the fact that total organic content (TOC) even in the best of cases tends to be only 10% whereas coals are predominantly organic matter. This has led many to expect that the quantities of adsorbed gas in shale cannot be very high compared to free gas. Lab-based core analysis studies such as Vega *et. al* (2013), and Heller and Zoback (2014) have indeed appeared to confirm this perception. Furthermore, numerical simulation studies such as those by Pan and Connell (2015) and Seales *et. al* (2017) have shown that sorbed quantities are unlikely to make a meaningful impact on ultimate recovery efficiencies. As such, the importance of adsorption is currently considered to be low by many in the shale gas community.

Other mechanisms of storage, such as dissolved gas in organic matter, oil and water, or trapped by the molecular sieving effect of clays, have been proposed by some authors, but the relative contributions of these modalities is also considered to be low (Ross and Bustin 2009; Ambrose et al. 2010; Gensterblum et al. 2015). This automatically implies under our current understanding of gas storage in shales that free gas must be the bulk of both GIP and produced gas. There are

plenty of studies that investigate the volumetric capacity for gas storage in shales by measuring porosity using either helium porosimetry and pycnometry, or mercury intrusion porosimetry (MIP) (Yang and Aplin 2007; Ross and Bustin 2009; Chalmers, Bustin, and Power 2012; Sun et al. 2016). Helium is a low sorbing gas and mercury is a liquid at measurement conditions, and therefore these are excellent approaches towards measuring pore volume. However, there is a dearth of studies that systematically investigate the storage capacity of real gases in shales. The purpose of the experiments presented in this chapter is to investigate the storage capacity of different gases in samples from four different shales reservoirs. The principal goal is to quantify the proportions of free gas in the rock pores relative to total sample storage.

1.2 Methodology

1.2.1 Gas Porosimetry

1.2.1.1 Experimental Protocol

Gas porosimetry is a technique where the pore volume of a rock is determined by measuring the magnitude of the pressure drop caused by the expansion of gas from a chamber of known volume kept initially at a high gas pressure, into the pore space of a sample specimen maintained initially at a low pressure inside a pressure vessel. Rock pore space will hereafter be referred to as Pore Volume (PV) in this document. Figure 1 shows the pressure vessel and ancillary setup built for the experiment. In the context of this experimental setup, the initial high-pressure volume was the free space or annular volume surrounding the shale rock specimen mounted inside the pressure vessel, plus the volume of the tubing and fitting connections up to the pressure transducer on one end of the pressure vessel and the ball valve at the other end. The annular volume plus tubing volumes will hereafter collectively be referred to as Dead Volume (DV). The experimental steps followed for pore volume measurements are as follows:

1. The rock specimen is mounted into the pressure vessel, and the pressure vessel is closed. One port of the pressure vessel is connected to a pressure transducer and another port to a ball valve.

Pressure Decline Porosimetry

2. A gas line from the analysis gas cylinder is connected to the ball valve, and the ball valve is opened for approximately 1-2 seconds during which time the gas fills up the entire dead volume. This results in a nearly instantaneous rise in pressure inside the pressure vessel, which is registered and recorded by the pressure transducer. The magnitude of the pressure rise is approximately equal to the delivery pressure from the gas cylinder regulator, and in almost all cases was around 6.9MPa [1000psi], except in the case of Ethylene where it was 0.7MPa [111psi]. Due to the low permeability of shales, the assumption is that negligible quantities of gas enter the pore volume during this time.
3. Next, the ball valve is closed, thus creating a closed system downstream of the valve.
    a. Over time, the pressure inside the vessel drops because gas from the dead volume permeates into the pore volume. This pressure fall-off is recorded until pressure stabilizes.

Dead Volume Estimation

    b. Upstream to the ball valve, the gas line is disconnected and replaced with a connection to a small, known reference volume.
4. After the pressure stabilizes for a reasonable amount of time, the ball valve is opened again for 1 to 2 seconds. This causes the gas to expand into the reference volume, and the pressure drops. Once again, the assumption is that the gas within the PV is not involved in this expansion, because of the low permeability of shale. This drop in pressure provides an estimate of the DV of the system.

Pressure Buildup Porosimetry

5. The ball valve is then shut again and the reference volume disconnected, a process that takes no more than about 5 seconds.

6. The ball valve is then opened once more, this time to the atmosphere for 1 to 2 seconds. This causes the pressure to drop to around atmospheric pressure 0.1Mpa [14.7psi].
7. Lastly, the ball valve is shut. This causes the pressure in the vessel to rise over time, due to the expansion of gas from the PV into the DV. The experiment is considered concluded when this buildup of pressure stabilizes.

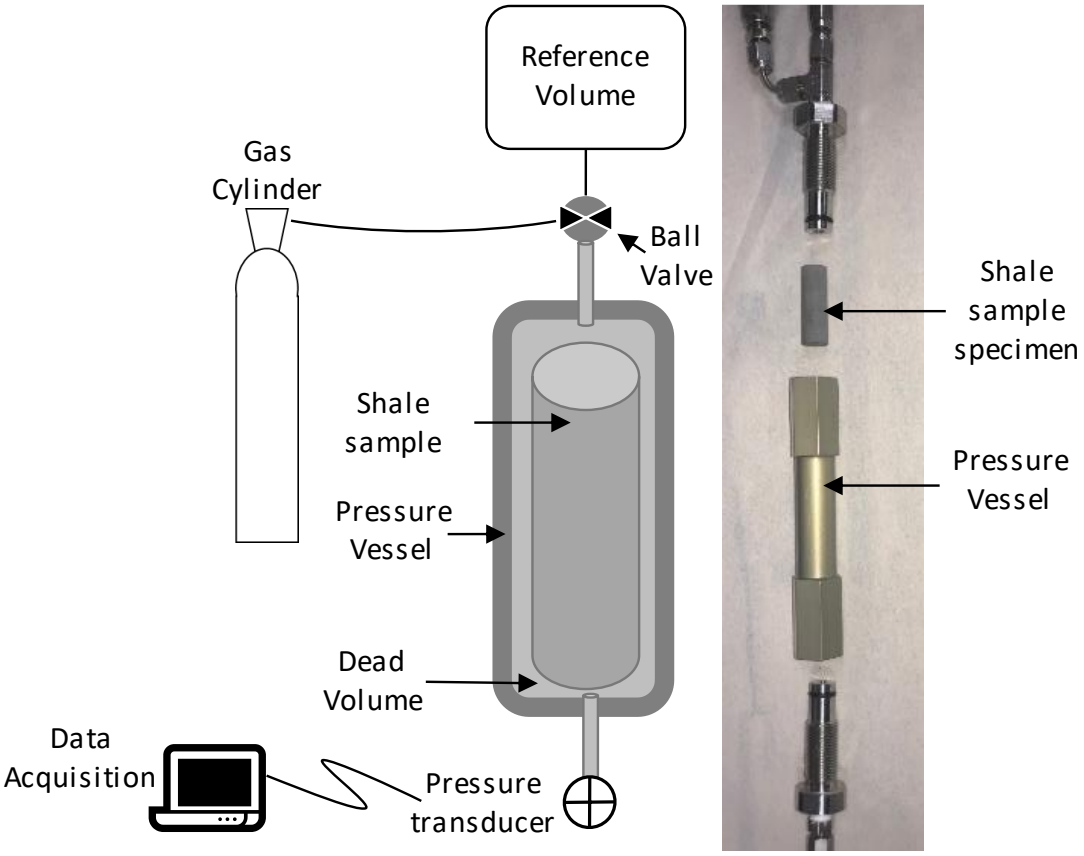

Figure 1: Experimental setup used for Gas Porosimetry. Left - Schematic drawing, Right - Enlarged image of the pressure vessel and shale sample specimen.

1.2.1.2 Measurement Principles

The main principle behind Gas Porosimetry is Boyle's Law as given by,

$$pv = k \tag{1.1}$$

Where p, and v are pressure and volume, and k is a constant. Equation 1.1 describes the behavior of an ideal gas in a closed isothermal system. This equation is really a special case of the real gas law given by,

$$pv = ZnRT \tag{1.2}$$

where, Z is the real gas compressibility factor or Z-factor, n is the number of moles of real-gas in the system, R is the universal gas constant and T is temperature.

For the purposes of estimating PV from the *Pressure Decline Porosimetry* phase of the experiment, hereafter referred to simply as the decline phase, the following relationship can be derived from equation 1.2,

$$PV = \left(\frac{\left(\frac{p}{Z}\right)_f - \left(\frac{p}{Z}\right)_i + p_{atm}}{\frac{p_f}{Z_f} * DV} \right)_{decline} \tag{1.3}$$

Where p_i, p_f, and p_{atm} are initial, final and atmospheric pressures respectively.

The DV required in equation 1.3, is estimated from data from the *Dead Volume Estimation* phase of the experiment, hereafter referred to as the DVE phase by,

$$DV = \left(\frac{\left(\frac{p}{Z}\right)_f * v_{reference}}{\left(\frac{p}{Z}\right)_i - \left(\frac{p}{Z}\right)_f} \right)_{DVE} \tag{1.4}$$

The PV can also be estimated from the *Pressure Buildup Porosimetry* phase of the experiment, hereafter referred to simply as the buildup phase, as follows,

$$PV = \left(\frac{\left(\left(\frac{p}{Z}\right)_f - p_{atm}\right) * DV}{\left(\frac{p}{Z}\right)_i - \left(\frac{p}{Z}\right)_f} \right)_{buildup} \tag{1.5}$$

The Pressure–Z-factor relationship for all the gases studied was obtained from the National Institute for Standards and Technology (NIST) webbook (https://webbook.nist.gov/).

The bulk volume (BV) of the rock samples was calculated based on the dimensions of the samples. Porosity (ϕ) was calculated as,

$$\phi = PV/BV \tag{1.6}$$

1.2.1.3 Sample Preparation and Fluids Selection

Four different shale samples were used in this study. The physical properties of each of the shale is given in Table 1.

Table 1: Physical properties of shale samples used in this study

Sample	Diameter (mm)	Length (mm)	Total Weight (g)	Expected Porosity	Expected Permeability (nd)
Bakken	11.74	32	8.5	10-15%	500-5000
Marcellus	11.8,11.8,12.1	9.5,12,10.7	8.9	2-12%	1-50
Haynesville	12	35.7	11	5-15%	100-500
Mancos	12,12	12.3,23.5	11.4	2-10%	500-10000

Before every analysis, each sample was dried in a vacuum oven at 99°C for 24 to 48hours and additionally kept under vacuum for an additional 2 to 4 hours without heat.

Porosimetry measurements on all samples was conducted with Helium and Methane gas, thus providing a comparison between a theoretically non-sorbing, near-ideal gas in Helium, and a highly sorbing real gas in Methane. In addition, measurements with Argon were conducted on the Bakken and Marcellus samples to investigate the behavior of a theoretically inert noble gas. Separate characterization on the Marcellus using Xenon and Ethylene gases is discussed in Chapter 2.

1.2.1.4 Experiment Design

It is relevant to point out here some of the considerations and physical constraints related specifically to shales that guided the design of the above-mentioned experimental protocol. Shales are extremely low in permeability. Prior estimates of permeability for the Bakken and Mancos samples were in the 0.5-2μd range, and for the Haynesville samples were in the 50-250nd range and for the Marcellus sample was in the 1-50nd range. Such low permeabilities mean that pressure decline and buildup equilibration durations on large diameter cores can become very long, on the order of several days to even weeks. Shales are also highly laminated and friable along laminations. This makes coring long intact cores a challenge. Finally, the pressure vessels available for this study had a maximum sample length capacity of 38mm. A protocol with sample diameter around 12mm and length around 35mm was selected in an effort to balance competing constraints. In the case of the Marcellus and the Mancos, it was not possible to core an intact 35mm long sample. Instead, multiple shorter fragments were stacked to increase the amount of sample material used in an experiment. In the case of the Marcellus, this was an advantage given its ultra-low permeability. The additional surface area available for gas penetration from having multiple samples further helped to reduce measurement times. Despite this, the Marcellus was the tightest samples, with equilibration taking more than a day in almost every case.

Shales often are associated with low porosity, in addition to low permeability. Given the already small rock volume, the magnitude of pressure change during porosimetry was expected to be small, and the rate of change slow. In order to ensure measurable pressure changes, i.e. sufficiently large pressure drops, it was imperative to minimize the DV. This is why the DV is merely the annular volume and tubing volume, and no calibrated reference volume is used for the PV calculations as shown in equations 1.3 and 1.5. Having a separate reference volume in addition to the DV, as in more conventional porosimetry setups would have resulted in a smaller and possibly immeasurable pressure changes. Instead, a calibrated reference volume was used for high accuracy measurement of the DV itself (equation 1.4).

The challenge of small expected pressure changes in shales is further exacerbated by the ultra-slow rate of changes. This necessitates a high degree of gas leak resistance. For this purpose, it is very important to keep testing the tubing and fitting connections for leaks. On a couple occasions, fittings or connections had to be changed out to ensure continued measurement integrity. These changes affect the overall DV. This is the main reason why the DV measurement was conducted during every single trial. The buildup measurements of PV are an additional and, to an extent, redundant source of confirmation of the PV measured during decline.

1.2.2 Gas Adsorption

1.2.2.1 Low-Pressure Surface Adsorption (LPSA)

Gas adsorption measurements, as the name suggests, are designed to estimate an adsorbed gas isotherm for a given rock sample. Room temperature gas adsorption measurements were carried out on a Micromeritics ASAP 2040 instrument and cryogenic measurements on a Micromeritics Tristar II instrument. Both instruments utilize a volumetric methodology to measure sorbed gas quantities. The complete details of the measurement methodology are too involved to be described here and are outside the scope of this document. The reader is referred to the manufacturer – Micromeritics, for complete details. However, in order to help the reader develop an appreciation of the implications of these measurements, a brief and simplified overview of the methodology is covered in this section.

Figure 2 shows a schematic of a general gas adsorption setup. At the heart of the system is a gas reservoir including plumbing to pumps, valves, and temperature-pressure measurement devices. The volume of this reservoir plus plumbing manifold, hereafter referred to as the *manifold*, is manufacturer calibrated and known with high precision. Electronic actuators can independently open and close all valves in the system and are precisely controlled by a computer system. Before measurements of sorbed gas capacity are made, the volume inside the sample holder, including

sample pore volume needs to be measured. This volume is referred to as the '*free space*' and the steps for this are as follows:

1. The manifold and sample holder are evacuated.
2. The manifold is then charged to a certain pre-specified pressure, typically close to atmospheric with helium gas. During this time, the sample holder is maintained in an evacuated state.
3. Once charging is complete, the valve connecting the manifold to the sample holder is opened, and gas from the manifold is allowed to expand into the sample holder. This causes the pressure to drop. The magnitude of the drop can be used to calculate the volume available to free gas in the sample holder. This includes the sample pore volume. Helium gas is used for this calculation because the assumption is that Helium is non-sorbing, and therefore, all the helium in the sample holder exists in a free state.

The steps towards estimation of sorbed gas capacity at discrete pressures are similar to the measurement of free space. First, the sample holder is evacuated. The steps thereafter are as follows:

1. The manifold is evacuated.
2. The manifold is then charged with the probe gas to a pressure typically slightly higher than the specified pressure at which the adsorption capacity is desired.
3. Once charging is complete, the valve connecting the manifold to the sample holder is opened, and gas from the manifold is allowed to expand into the sample holder. This causes the pressure to drop.
4. The drop in pressure is used to calculate the number of moles of gas introduced into the sample holder.

$$n = \frac{v_m}{RT}\left(\frac{p_i}{Z_i} - \frac{p_f}{Z_f}\right) \tag{1.7}$$

where, v_m is manifold volume.

5. If the equilibrium pressure is not within a pre-specified tolerance to the desired equilibrium pressure, then steps 1-4 are repeated and the moles introduced are added up.
6. Once the equilibrium pressure is within tolerance of the desired equilibrium pressure, the quantity adsorbed is calculated as follows,

$$n_{ads} = n_T - \frac{p_{sp} v_f}{Z_{sp} RT} \tag{1.8}$$

where, p_{sp} is the specified pressure for which adsorbed moles are to be measured; n_T are the total moles of gas introduced at the end of step 5; v_f is the *free space* volume.

7. The moles introduced are reset to zero and steps 1 through 6 are repeated for the next specified pressure on the desired isotherm.

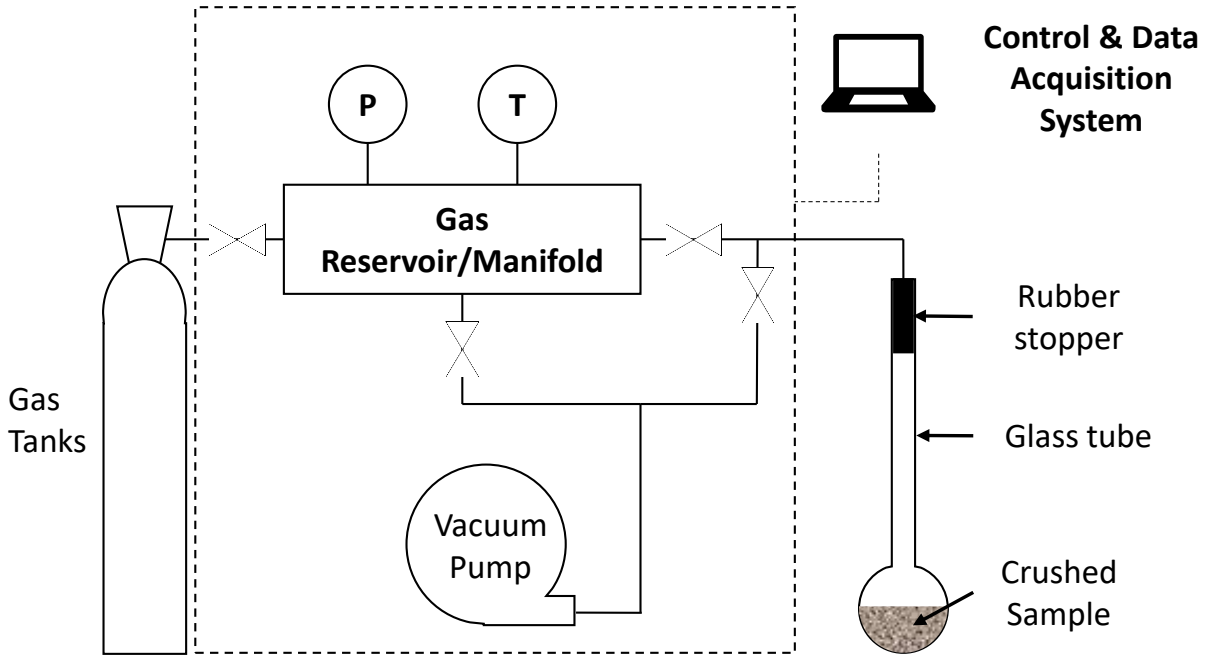

Figure 2: Schematic of gas adsorption instrument

1.2.2.1.1 Sample Preparation

Three shales samples – the Bakken, Marcellus, and Haynesville were analyzed using LPSA. Samples were crushed and sieved through an 80-mesh filter to make sure there were no large grains, and all particles were less than 200μm in size. This was done in order to facilitate access of gas to porosity. Due to scheduling constraints on the gas adsorption systems, all samples could not be tested. Given the mineralogically complex, heterogeneous and layered structure of the Mancos it was difficult to create a truly representative powder. Therefore, it was considered low in priority and not included in the analysis.

The carcass of the core used to extract plugs for gas porosimetry (section 1.2.1) was used as the initial rock material for the crushing and filtering process. In the case of the Bakken and Marcellus, this initial material was obtained from the vicinity (adjacent to a few centimeters) of the core plug. However, for the Haynesville sample core plug extraction was done by a third-party vendor and the proximity of the pre-crushed material to the core plugs could not be fully confirmed. However, even in the case of the Haynesville, the gas porosimetry plug and the material used for powdering and LPSA analysis were from the same sample parent whole-core.

All sample powders were 'degassed' before LPSA analysis by placing them in the sample tube and gas adsorption machine. This included evacuation and heating of samples to 99°C for 4 to 12 hours and maintenance under evacuation for another 1 to 4 hours at room temperature. The extent of degassing was checked periodically by suspending vacuum and measuring the rate of rise of pressure in the sample tube. The sample was considered degassed and "clean" when the rate of rise of pressure was less than 10μbar over a 3min testing interval.

1.2.2.2 Sorption from Porosimetry

In addition to the above-described methods of measuring gas adsorption isotherms, adsorbed gas quantities were also estimated from the gas porosimetry experiment. The total moles of gas introduced into the sample were calculated as,

$$n_T = \left[\frac{DV}{RT}\left(\frac{p_i}{Z_i} - \frac{p_f}{Z_f}\right)\right]_{decline} \tag{1.9}$$

The sorbed moles were then calculated as,

$$n_{ads} = \left[n_T - \frac{p_f PV_{helium}}{Z_{sp}RT}\right]_{decline} \tag{1.10}$$

The assumption once again is that the pore volume as measured by helium decline porosimetry is the true pore volume. For any other gas, the difference between the moles introduced during decline and the moles expected at the equilibrium pressure ($\left[p_f\right]_{decline}$) represents sorbed moles. It is important to note over here that this assumption that excess gas uptake relative to free gas uptake represents sorbed gas is widely practiced. Moreover, it is identical and fundamental to the way in which adsorbed gas is estimated via equation 1.8 based on LPSA data. Nevertheless, excess uptake is merely indicative of more moles of gas being present than would be expected based on the measured pressure-volume-temperature (PVT) data and assumed equation-of-state (EOS) for the gas. Therefore, this excess uptake is actually indicative only of a denser state of gas than expected based on PVT-EOS data and model. There are other possible mechanisms, besides adsorption, that might explain this densification of gas such as induced supercriticality or, more generally, confinement induced alterations to fluid behavior that lead to densification. Such mechanisms, if indeed prevalent, should be incorporated into improved EOS models that are capable of predicting the so-called 'excess uptake'. We shall explore some of these alternate mechanisms of gas densification in Chapter 2. Despite this awareness that sorption is only one possible manifestation of the broader phenomenon of gas densification, in this chapter we choose to follow convention, and consider all excess uptake (same as 'densified gas') as sorbed gas.

1.3 Results and Discussion

1.3.1 Porosimetry

Figure 3 shows the results of porosity estimation from the gas intrusion porosimetry experiment. In all, 26 porosity measurements were conducted, 24 of which are reported in Figure 3. In all cases, the buildup porosity was found to be lower than the decline porosity. The reason for this discrepancy is thought to be errors introduced by the assumption in the experimental protocol. In contrast to the decline measurements which take 1-2 seconds to begin, before beginning the buildup measurements, the dead volume measurement steps, as well as the depressurization of pressure vessel to near atmospheric pressure, takes close to 10seconds. It is possible that this is sufficient time for the pore pressure to drop, especially for the higher permeability Bakken and Mancos samples, thus violating the assumption that pore fluid is not involved during these steps. In addition, some of the difference between gas intake during decline, and output during buildup, may be attributed to residual sorption, i.e., some of the gas entering the sample during decline may remain behind in the sample as sorbed gas at the buildup equilibrium pressure. This latter possibility will be explored in later sections of the document. On the basis of the above-mentioned reasons, in the forthcoming discussion, we will consider the decline porosity numbers to be more accurate and a better representation of true storage capacity of the sample for any given gas.

A key observation from Figure 3 is the large difference between porosity derived using helium as probe gas and methane, in the case of the Marcellus and Haynesville samples. Based on initial expectations of porosity as shown in Table 1, the methane porosities of 43.7% and 37.0% and argon porosities of 43.5% and 27.8%, in the Marcellus and Haynesville samples respectively, are unexpectedly high. It is unreasonable to expect that such numbers represent actual pore volume within the sample. The reader may recall from Section 1.2.1 that these estimations of porosity are based upon the assumption that the stored gas in the sample pore space exists as free gas at the measured experimental equilibrium pressure. The higher than expected numbers strongly

indicate that this assumption is likely to be incorrect for almost all cases given that the methane porosity numbers for all samples were higher than the helium porosity. However, the free gas assumption may be a particular departure from reality in the case of the Marcellus and Haynesville samples. For this reason, the results from the gas porosimetry experiments are reported as "Equivalent Porosity", to indicate storage capacity as equivalent volumes of free gas. The measured porosity will hereafter be referred to as ϕ_{eq}.

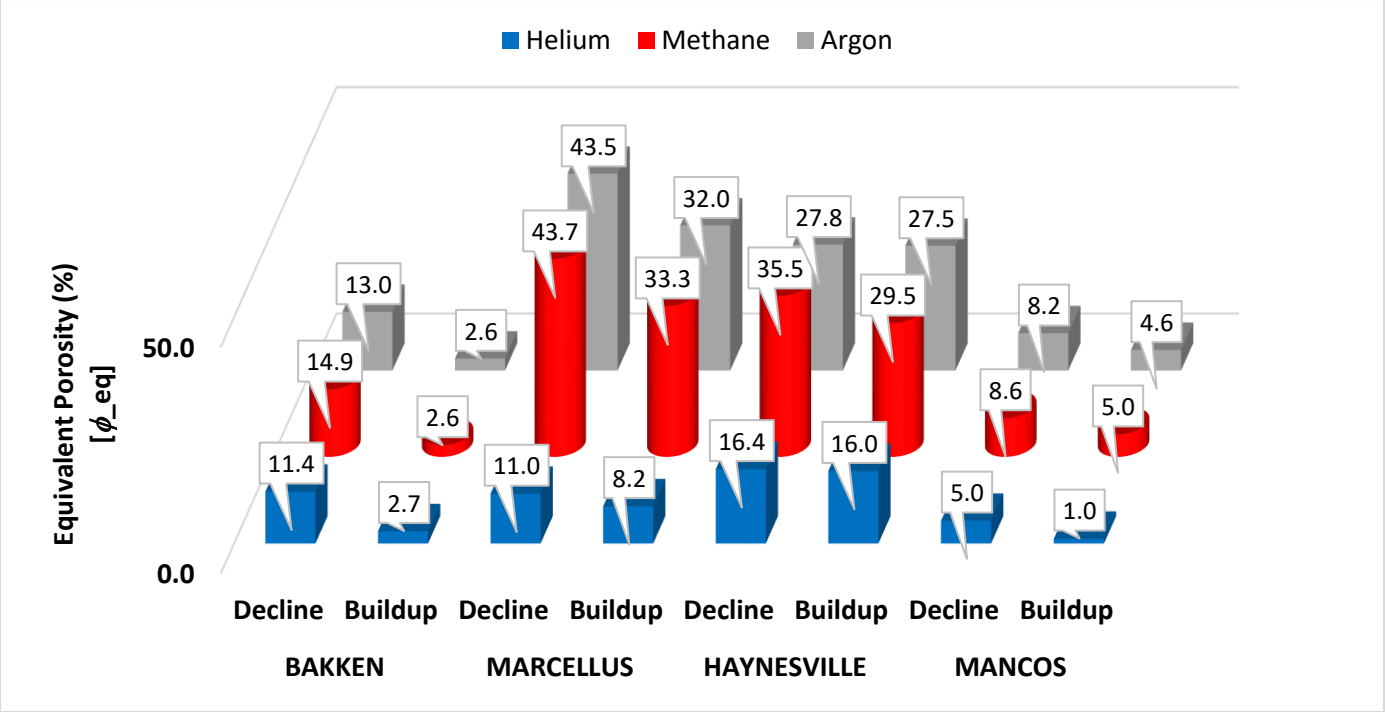

Figure 3: Equivalent porosity ($\boldsymbol{\phi_{eq}}$) estimates from gas intrusion porosimetry experiments on four different shale samples using helium, methane and argon gas.

Another interesting observation from Figure 3 is that the argon ϕ_{eq} results appear to mirror the methane results. For instance, the smallest percentage difference between helium and methane ϕ_{eq} was in the case of the Bakken sample (11.4% vs. 14.9%) and the largest difference in the Marcellus sample (11.0% vs. 43.7%). The same pattern was observed from the helium vs argon.

data – little difference compared to helium in the Bakken sample (11.4% vs. 13.0%) and a large difference in the Marcellus (11.0% vs. 43.5%). This is interesting because one might expect high storage in an organic rich sample due to the preferential sorption of a hydrocarbon gas, such as methane to organic matter, whereas argon, as a nobel gas, might be expected to behave more similarly to helium. The counterindications to such intuition suggests that there may be more to gas storage than rock composition-controlled adsorption. Furthermore, the vast differences in gas storage capacity within and across shale for different gases indicate that storage behavior may be a unique function of the specific form of interaction between a rock and fluid, and it cannot simply be characterized based on measurement of pore volume. The similarities between the storage behavior in the case of the Marcellus and Haynesville samples are noteworthy. Detailed characterization has been done on each sample to investigate the potential reasons for such similarities and differences. This characterization-based analysis is discussed in chapter 3.

1.3.2 Sorption

Based on the standard assumptions of equations 1.8 and 1.10, any gas that is not free gas is automatically considered sorbed gas. For the purposes of discussion in the rest of this chapter, this assumption shall be maintained, and no other possibility will be considered. Instead, possible alternate mechanisms for the excess storage capacity of gases compared to the helium storage capacity will be explored in detail in Chapter 2.

Figure 4 shows the proportion of sorbed gas to total storage as calculated from the porosimetry experiment equations 1.9 and 1.10. This is described by the sorbed gas ratio Rs, which is defined as,

$$R_s = (n_{ads}/n_T) \tag{1.11}$$

The Marcellus sample showed the highest levels of methane sorption relative to total storage at around 75%, while the Bakken had the lowest at ~24%. The Haynesville and Mancos samples also

had around half their stored gas exist as sorbed gas. Once again, the storage of argon was very similar to the storage of methane. These results indicate that the sorption capacities of all, but the Bakken shale, are quite large relative to their overall gas storage capacity. Therefore, this aspect of storage cannot be ignored from the perspective of Gas-in-Place (GIP) measurements. Further studies at higher pressures and with larger samples are justified in order to evaluate the relevance of these results at larger scales. Chapter 4 will look into the mobility of this sorbed component of storage and implications of this sorbed gas on transport.

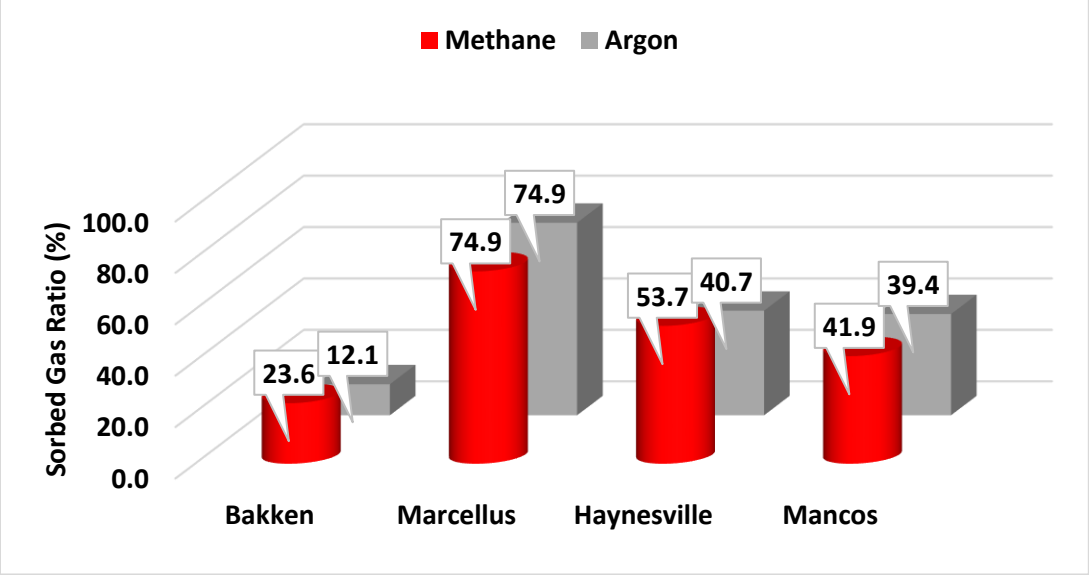

Figure 4: Proportion of sorbed gas relative to total storage

Low-pressure gas adsorption or LPSA isotherm measurements were also carried out in order to provide independent estimates of sorption capacities. The results of methane adsorption on the Bakken, Marcellus and Haynesville samples are shown in Figure 5. As mentioned in section 1.2.2.1.1, the Mancos sample could not be analyzed. The LPSA results indicate the same behavior as indicated by Figure 4 in the sense that the Marcellus had the largest uptake capacity, while the Bakken had the lowest. The Haynesville results were intermediate to the Bakken and Marcellus.

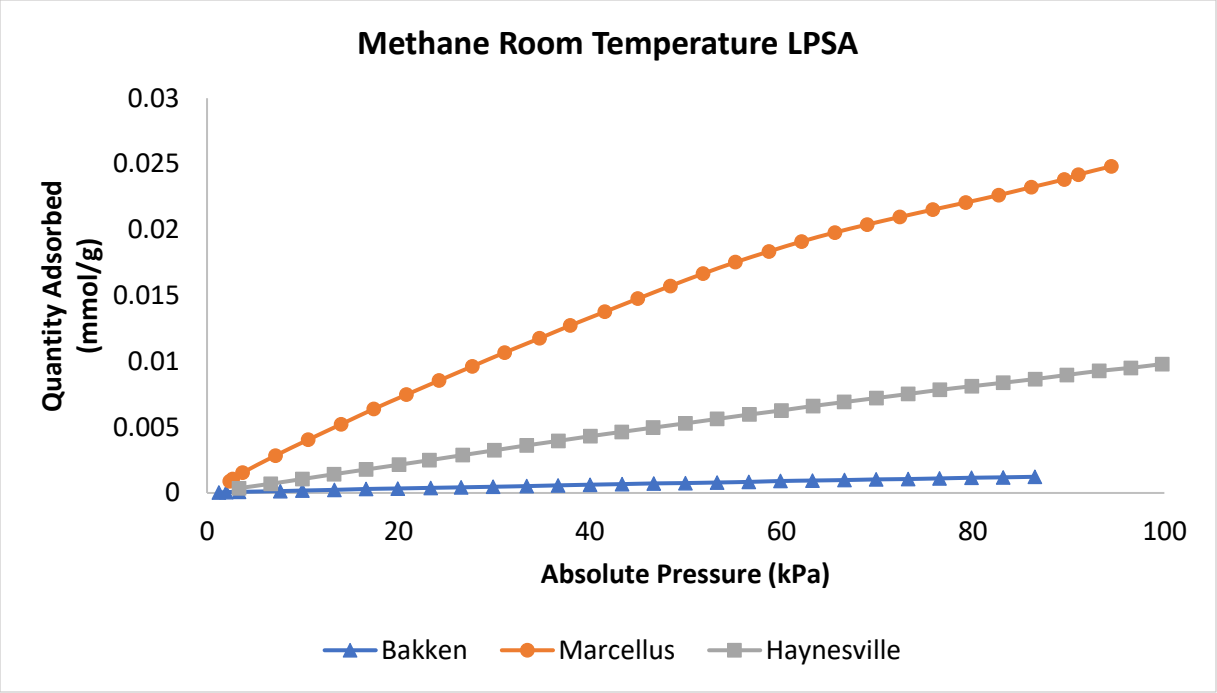

Figure 5: Methane adsorption isotherm derived from LPSA

Figure 6 is an attempt to compare the methane sorption capacity results obtained from porosimetry on whole core vs. LPSA on powdered sample. The LPSA adsorption isotherm has been extrapolated to porosimetry pressures of around 6.9MPa [1000psi] in two ways – 1. Linear extrapolation, and 2. Langmuir extrapolation.

Linear extrapolation as the name suggests is a straight line fit of the Quantity Adsorbed vs Absolute Pressure data are shown in Figure 5, and extrapolated to 6.9MPa.

Langmuir fit of the data, on the other hand, is a linear fit of the data in the following form,

$$\frac{p}{v_a} = \frac{1}{v_m b} + \frac{p}{v_m} \tag{1.12}$$

where, v_a is the adsorbed gas volume at a given pressure; v_m is the volume of a monolayer; and b is a constant.

The p/v_a vs p plot is extrapolated to 6.9MPa. The adsorbed quantity is then given by,

$$v_a = \left[\frac{p}{\frac{p}{v_a}}\right]_{@6.9MPa} \tag{1.13}$$

The results of Figure 6 show that the general trend of sorption capacities to be lowest in the Bakken, higher in the Haynesville, and highest in the Marcellus, using all three methodologies. However, the results from the LPSA analysis are inconclusive when it comes to confirming the porosimetry results. The LPSA Linear Extrapolation estimates higher sorption than the measured porosimetry results whereas the Langmuir model greatly underestimates it. There are a few possibilities to explain this discrepancy. The linear extrapolation may not be the most accurate model because as surface sites are saturated at higher pressures, the rate of sorption vs. pressure is likely to drop. This may explain the over-estimation from the Linear Extrapolation model at high pressures. The Langmuir model is generally considered to be a better model for fitting sorption data. However, it is possible that the LPSA sorption data itself is not equilibrated. Pores in shales are extremely small and the permeability really low. Given this fact, it may be that the particle sizes were too large and the tolerance on pressure change was too generous during the sorption capacity measurements. Therefore, data may have been collected before pressure equilibrium at every step along the acquisition of the adsorption isotherm leading to a general underestimation of sorbed capacities. However, this is unlikely to be the case for the Bakken sample given its higher permeability. One more possibility is that the Langmuir model, or the assumption of surface adsorption in the first place is incorrect, and the mechanism of 'sorption' itself is different. This is what will be explored in the next chapter.

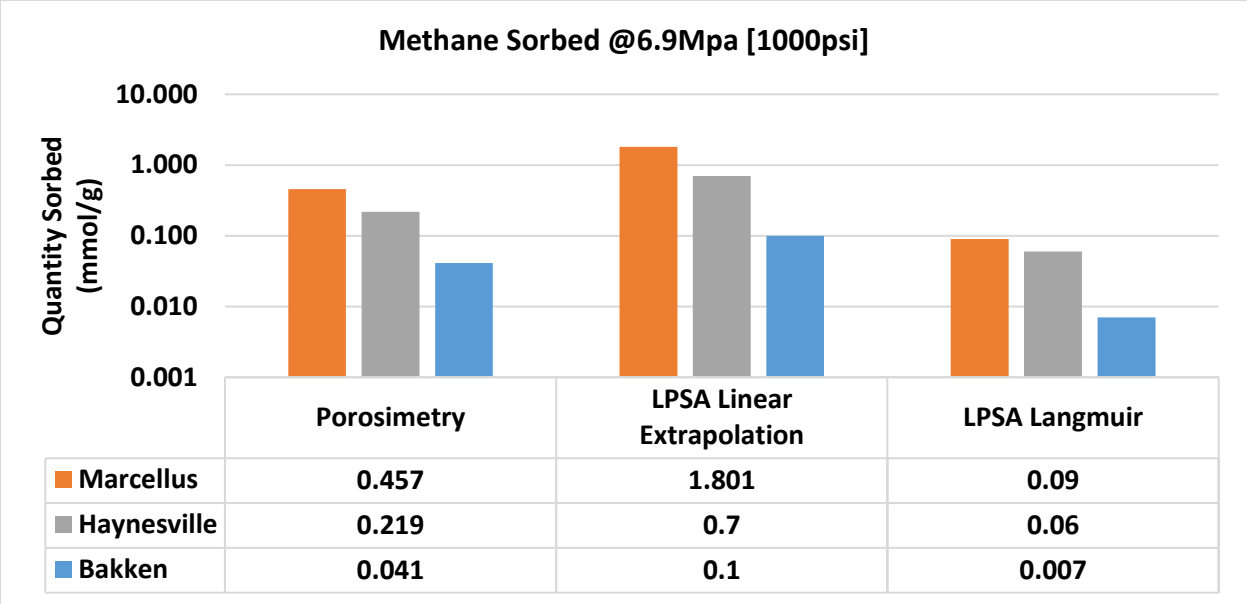

Figure 6: Methane sorption capacities @6.9Mpa as measured by porosimetry compare against estimates of methane sorption from the LPSA data.

1.4 Conclusions

This chapter described a series of experiments to estimate the storage capacity of a few different gases in 4 shales – the Bakken, Marcellus, Haynesville, and Mancos. The assumption was that gas would be stored as either free gas or sorbed gas. The porosimetry experiment was designed to reveal both the total storage and the relative proportion of sorbed gas to total storage. Separate low-pressure sorption experiments were also conducted to provide independent estimates of sorption capacity.

1. The results of porosimetry experiments indicate that the gas storage capacity of several shales for methane and argon is significantly higher than their storage capacity for helium. This implies that pore volume measurements are not a good indicator of potential storage capacities and specific rock and fluid interactions must be considered.
2. A large fraction, greater than 40% of the stored gas in all the samples except the Bakken is sorbed gas. The Marcellus sample had the highest proportion of sorbed gas to total storage at around 75%.

3. LPSA measurements qualitatively follow the trends in sorption capacity observed from porosimetry measurements. However, there are discrepancies between the porosimetry and LPSA measurements when the LPSA data is extrapolated to the porosimetry pressure of 6.9MPa. Depending on model selection, Linear extrapolation vs. Langmuir, the LPSA data can be extrapolated to overestimate or underestimate the porosimetry data. This raises questions over the assumption that the mechanism of gas storage is indeed surface adsorption.

2: Storage of Real Gases (Part 2): Fluid Behavior

2.1 Background

In recent years there is a growing consensus among shale oil and gas researchers that the properties of fluids in shale pore systems are different from bulk or free fluids. These differences include reduced bubble points, increased dew points, and differences in density, viscosity and interfacial tension (Nojabaei, Johns, and Chu 2013; Luo, Lutkenhaus, and Nasrabadi 2016; Jin and Firoozabadi 2016; Pathak et al. 2017; Kamari, Li, and Sheng 2018).

Nojabaei, Johns, and Chu 2013 were the first to demonstrate from field production data the lowered bubble point in a Bakken oil reservoir, and that this behavior could be explained by high capillary pressures. They were able to show this using thermodynamic modeling that accounted for nano-porosity in the Bakken shale and therefore, high capillary pressures. A more recent study by Kamari, Li, and Sheng 2018 used a similar approach and reached similar conclusions based on a model of an Eagleford shale reservoir. They further expanded their analysis to report differences in density, viscosity and interfacial tension as a function of pore size.

Most studies focused on fluid behavior in shales are interested in two-phase shale oil and retrograde condensate systems. Framing the problem in terms of capillary pressure inherently means assuming that the changes in fluid behavior are due to the presence of a gas and liquid interface. However, it has been known for a few decades now that even single phase fluid behavior is altered by residence in nano-pores. Thommes and Findenegg 1994 ran experiments by using pure fluid SF_6 in controlled pore glasses with pore width of 24nm to 31nm. They found that the critical temperature of the fluid was shifted downward relative to the bulk critical temperature and that fluid density was elevated. Morishige et al. 1997 showed similar results of lowered critical temperature for Ar, N_2, O_2, C_2H_4 and CO_2 gases on mesoporous molecular sieves. These results may have a significant bearing on fluid behavior in single phase dry shale gas reservoirs and raises questions on the mechanistic underpinnings of altered fluid properties.

Research into the fluid phase behavior of single-phase gas in natural shale systems is limited. Recent efforts to understand single phase behavior in shales includes primarily molecular modeling efforts (Perez and Devegowda 2017; Herdes et al. 2018) and some experimental effort on proxies such as silica glass or pure clay minerals (Cole et al. 2010; Luo, Lutkenhaus, and Nasrabadi 2016).

In this chapter, we will take a deeper look into the results of fluid uptake in the shales described in the previous chapter in order to uncover more information about their properties. X-ray micro-CT imaging results using a radio-opaque probe gas xenon will be presented that allows direct calculation of in-situ fluid density. These results will be compared against the average fluid density estimated from porosimetry. The results will be analyzed to explore alternate possibilities to surface adsorption in order to explain the enhanced storage observed.

2.2 Experiments

2.2.1 X-ray Computed Tomography (CT)

X-ray CT is a non-destructive imaging technique that can be used to generate three-dimensional (3D) maps of an object. The CT system consists of an ionized x-ray source, a detector, a translation system, and a computer system that controls motions and data acquisition. X-rays from the source pass through the object being imaged and are picked up by a detector resulting in a 2D projection of the object. The 3D image reconstruction is based on multiple X-ray measurements made through a specimen along different paths, which allow the visualization of its interior (Wellington and Vinegar 1987). The resultant images are 3D maps of the object X-ray attenuation which is proportional to sample density and atomic number. In a standard grayscale image, dark regions indicate materials of low density and atomic number while bright regions indicate high density and atomic number. CT images are useful in identifying bedding patterns, fractures, and dynamic observation of in-situ fluid transport in natural porous materials and shales. CT images in this study were acquired on a GE Phoenix V-TOME X L300 industrial CT scanner. The images were reconstructed using GE DatOS software and post-processing was done using Avizo® 9.3.

CT imaging was conducted to get direct visual and quantitative evidence of the gas storage and transport process in the shale matrix. Figure 7 is a schematic of the experimental setup for the gas transport and imaging experiments. The sample was mounted in a specially designed pressure vessel made of thin aluminum walls for high X-ray transparency. The physical setup was very similar to the porosimetry setup described in section 1.2.1. The arrangement of gas flow lines was slightly different in order to mount the setup in the CT scanner as shown in Figure 7. The pressure vessel containing the sample had only one port of entry which was connected via a T-junction to a ball valve and a pressure transducer. Xenon was used as probe gas because of its high X-ray opacity and contrast character. No confining stress was applied in order to maximize overall X-ray signal to noise ratio. Gas was injected as a single pulse and the valve then shut. From this point on the sample and surrounding gas became a closed system. Gas from the annular space flowed into the pore space within the sample until the pore, and annular pressure-concentrations reached equilibrium. The small annular and dead space made for a very sensitive system allowing for pressure fall-off measurements on samples with extremely low porosity. Samples were not jacketed in order to reach full saturation in the shortest possible time which in the case of ultra-tight shales can take several days to weeks.

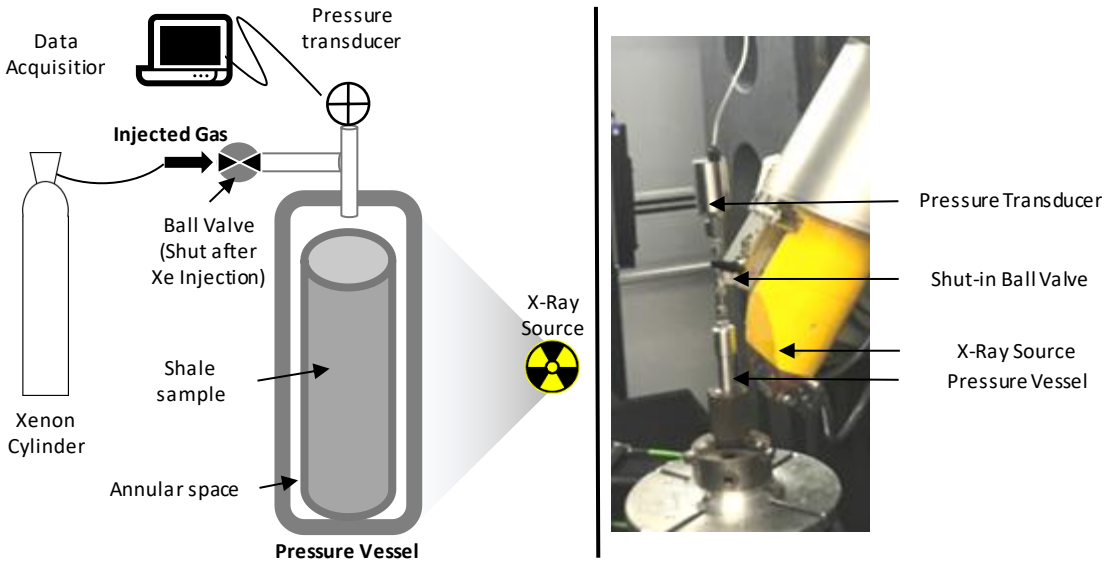

Figure 7: (left) Schematic of the pressure vessel containing the sample. (right) Pressure vessel and transducer assembly placed inside CT scanner

2.2.1.1 Sample Preparation and Imaging

The shale used for the gas injection and CT imaging experiment that will be discussed in this chapter was the Marcellus. Additional imaging was performed on the Bakken and Mancos samples. However, these will be described in chapters 3 and 4.

The sample in this case was two whole 12mm diameter cylindrical core plugs. The plugs had been cored using water as the lubricating fluid and dried at room temperature over several months. After the two plugs separated by the O-ring spacer had been set inside the pressure vessel, a vacuum was applied to the assembly via the ball valve for 30 hours to evacuate the annular space and fractures. At this stage, the first CT image of the assembly was acquired. The X-ray energy was 200kV, voxel size 13.8µm, and scan duration 1.35hrs. Next, the 2.84Mpa pulse of Xenon was introduced into the vessel, and the valve was shut off. The assembly was imaged immediately and then again every few hours for up to 58 hours. After 58 hours the assembly was removed from the CT scanner due to scheduling reasons and unavailability of the scanner. The assembly was imaged once more a month later to capture the final pressure-concentration equilibrium

state. Altogether ten image data sets were collected: *fresh* (pre-Xenon injection), after Xenon injection at *0, 3, 14, 19, 26, 39, 48, 58 hours*, and at *equilibrium* (one month). The pressure fall-off data was measured continuously for the first 58 hours from Xenon injection. Pressure data was also collected for the subsequent 10 days, and it was observed that the pressure reached equilibration in about 7 to 10 days. However, due to a computer error, the 58hour to 10day data could not be saved.

2.2.1.2 Porosity and In-Situ Density Calculation

The only explicit form of porosity detected through imaging of the shale core plugs were some occasional fractures. Due to ultra-small pore sizes, almost all the porosity in shale is well below image resolution. Porosity calculation was therefore done using image subtractions of initial (fresh) and gas saturated (equilibrium) images.

X-ray CT images are a map of the attenuation of the X-ray beam coming from the source, by objects within the beam's field of view (FOV). Since X-ray attenuation is largely a function of the density of the objects within its FOV, the attenuation of a porous medium can be described by the following equation,

$$CT_{matrix} = CT_{solids} * (1 - \phi) + CT_{gas} * \phi \tag{2.1}$$

Where, CT_{matrix} is the actual measured CT number, CT_{solids} is the CT number of the solid grains in the rock matrix, CT_{gas} is the CT number of the gas occupying the pore space, and ϕ is porosity.

Assuming that the only change between each image is the type and quantity of gas inside the pore space, porosity can be derived using the fresh and equilibrium datasets as follows:

$$\phi = \frac{CT_{matrix}^{@\text{equilibrium}} - CT_{matrix}^{@fresh}}{CT_{Xenon}^{@equilibrium} - CT_{air}^{@fresh}} \tag{2.2}$$

Where, $CT_{matrix}^{@\text{equilibrium}}$ is the measured CT number of the rock matrix filled with Xenon at equilibrium conditions, $CT_{matrix}^{@fresh}$ is the CT number at fresh conditions, $CT_{Xenon}^{@equilibrium}$ is the CT number of the free Xenon phase at equilibrium, and $CT_{air}^{@fresh}$ is the CT number of the free space at fresh conditions. The porosity estimate obtained in this way was 51%. This number is too high to represent actual porosity given that porosity estimates from other independent techniques including, among others, MIP and Helium Porosimetry was in the 1.5-11% range. Just as in section 1.3.1, this estimation of porosity is, in reality, the equivalent porosity indicating total uptake of xenon by the sample.

To begin to understand the high ϕ_{eq} estimation from CT data, one needs to first take a closer look at the physics governing X-ray CT numbers. CT numbers are proportional to X-ray beam attenuation and are given by the following equation:

$$CT = \rho(a + b * Z^3) \tag{2.3}$$

where ρ is the density of the material, a and b are proportionality constants related to the Compton Scattering and Photoelectric cross-sections of the material and Z is the atomic number of the material being imaged.

It can be seen from equation 2.3 that the CT number of the material being measured is a function of material density and atomic number. Since the atomic number of a material does not change, it follows that the high porosity given by equation 2.2 is due to - 1.) a large density difference between the matrix at equilibrium and fresh conditions i.e., a large numerator; and 2.) due to a small relative difference between xenon and air CT numbers, i.e., a small numerator. Now the numerator data is directly measured in via imaging. The numerator data, on the other hand, uses the CT numbers for free-xenon and air in the annular space as an approximation for the CT numbers of xenon and air in the pore space. Figure 8 shows the measured CT numbers of free-xenon for all the images and shows a clear linear relationship with pressure. This is to be expected because gas density is also a linear function of pressure. However, in order for the attenuation of the matrix to be as high as observed, at a porosity closer to those independently measured,

the density of the xenon within the pore space must be higher than the density of free-xenon phase, i.e., the numerator in equation 2.2 should be larger than our previous assumption using free-xenon CT number.

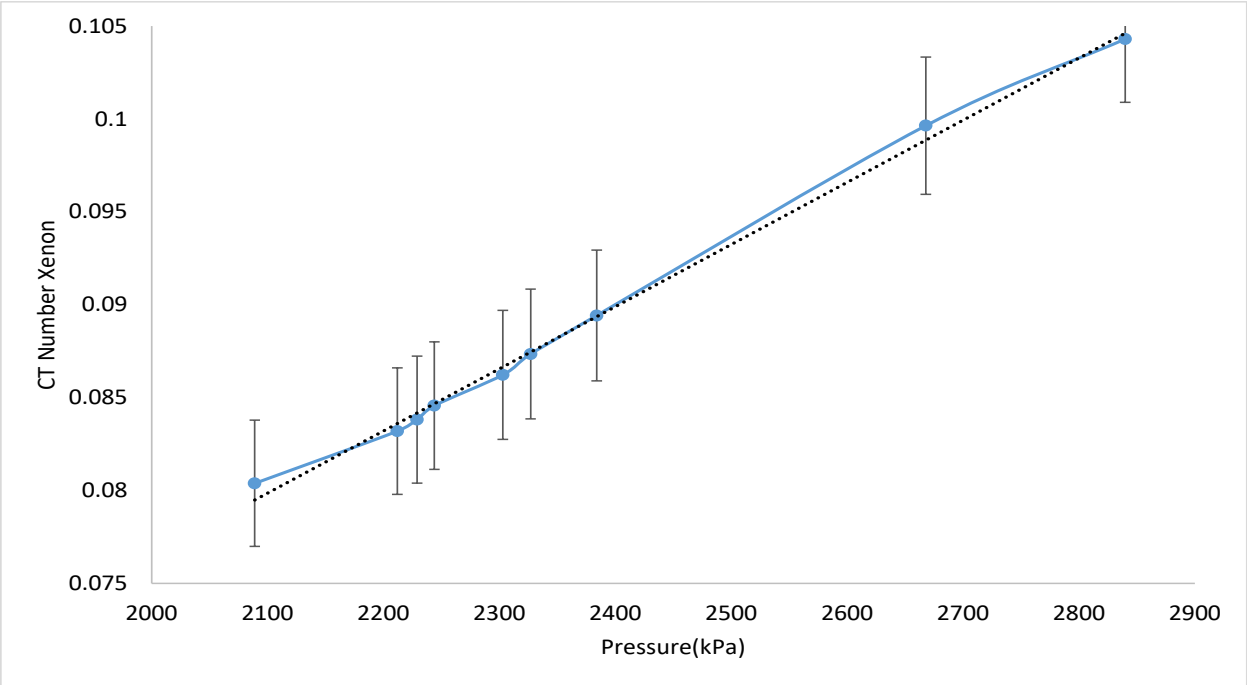

Figure 8: Measured CT numbers of xenon in free-gas phase within the annular and hollow spacer regions are linearly proportional to pressure because gas phase density is a linear function of pressure.

From equations 2.1 – 2.3, the following expression can be derived for the true in-situ density of xenon in the pore-space

$$\rho_{Xenon}^{@\text{equilibrium}} = \frac{\left(CT_{matrix}^{@\text{equilibrium}} - CT_{matrix}^{@fresh}\right)}{(a + b * Z_{Xenon}^{3}) * \phi} \qquad (2.4)$$

The complete derivation of equation 2.4 as well as the proportionality constants a and b are given in Appendix A of this document.

2.2.2 Fluid Densities from Porosimetry

In addition to X-ray CT, densities of pore fluids can also be estimated from the Porosimetry experiment described in section 1.2.1. The key assumption here that enables one to calculate fluid density is that the true pore volume of a given shale sample is the pore volume estimated from helium decline data. Once the moles of *gas of interest*, say methane or argon, in the pore space, has been calculated using equation 1.9 with the decline data for the *gas of interest,* and the pore volume using equation 1.3 has been calculated using *helium* decline data, the density of the gas of interest can be calculated as follows,

$$\rho_g^p = \left(\frac{n_T|_g * MW_g}{PV_{helium}} \right)_{decline} \tag{2.5}$$

Where, ρ_g^{p} is the in-situ density of the *gas of interest in the pore space;* n_T is the total moles of the *gas of interest* in the pore space at pressure decline equilibrium; MW_g is the molecular weight of the *gas of interest*; and PV_{helium} is the pore volume estimate for the sample obtained from *helium* decline data.

2.3 Results

2.3.1 X-ray Computed Tomography (CT)

Figure 9 shows vertical cross-sectional slices of the sample at *fresh* and *equilibrium* states. Both images are visualized using the same brightness-contrast setting, and the relative brightness of the *equilibrium* image is due to the presence of xenon in the sample. No image enhancement or post-processing has been done to these images. The distinct presence of Xenon is only apparent because of the high signal to noise ratio achieved during image acquisition. A strongly attenuating material such as Xenon will often cause major beam hardening artifacts, which can make the

sample look much darker in the center, gradually brightening towards the outer radius, giving the illusion of radial fluid influx(Wellington and Vinegar 1987). However, due to the small diameter of the sample and minimal non-sample beam attenuation, the effect of beam hardening was negligible.

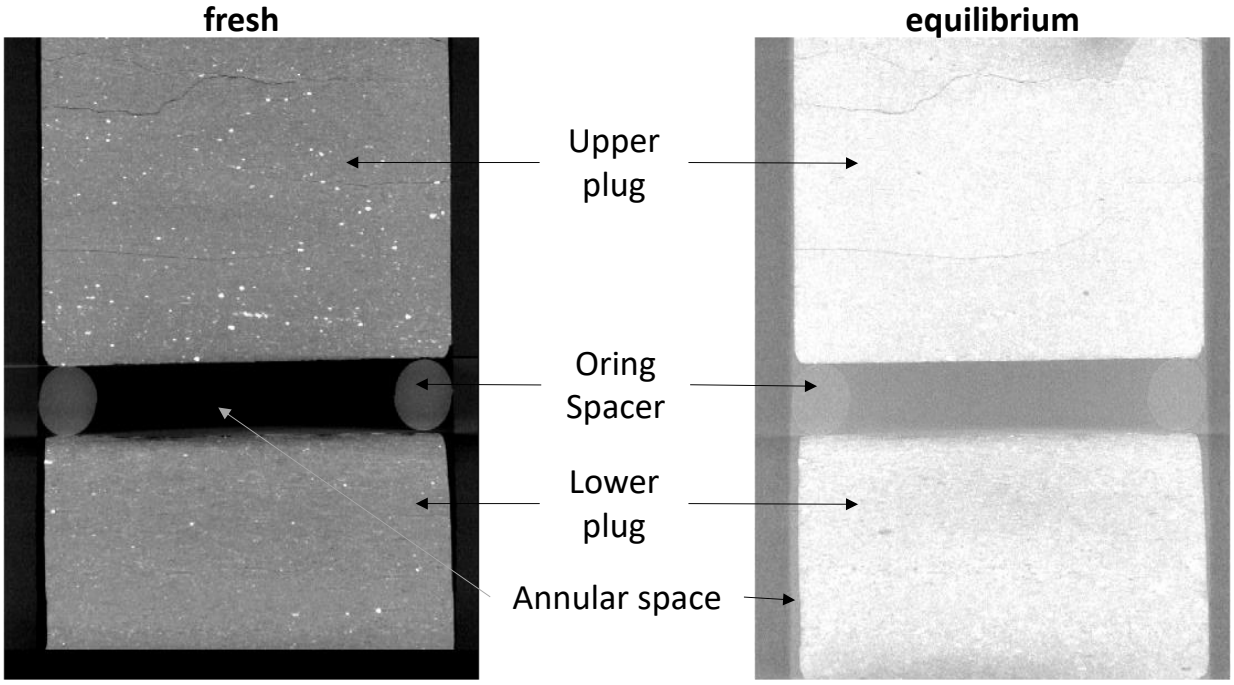

Figure 9: Vertical cross-sections of the Marcellus sample at the same visualization brightness-contrast setting. The final *equilibrium* state is brighter than the *fresh* (before gas injection) state because of the presence of xenon.

The degree of brightening relative to the fresh state is a function of the concentration or density of xenon occupying the pore space of the sample at any given voxel location. Assuming a porosity of 7% at every voxel location, this density of xenon was computed using equation 2.4. The mean density of xenon in the pore space calculated this way was 947.1kg/m^3. The probability distribution of xenon density at all sample locations is given in Figure 10. Vertical lines indicating the free-gas density of xenon at 2.8MPa and 22^{o}C, and the liquid density at boiling point (-108.1^{o}C) are provided for reference. The vast majority of data is significantly higher than the expected free-gas density of 181kg/m^3. This indicates widespread densification of most of the

pore fluid. At the same time, the vast majority of data is also significantly lower than the boiling point liquid density of 3100kg/m^3. Adsorbed gas is often considered to have the density of the liquid phase at boiling point. If this is true, then our data indicates that the pore fluid may not actually be adsorbed gas. However, it is also possible that a part of the fluid is adsorbed whilst a portion remains in the free gas phase, potentially resulting in an average density intermediate to the two phases. The current measurement protocol does not allow the clear and explicit differentiation of the densities of the two phases. Another possibility is that the adsorbed gas actually has a density lower than boiling point liquid density. For example, the Van der Waal's constant b is often used as an alternative (Heller and Zoback 2014). But even this value of 2568kg/m3 is much higher than most of the measured distribution. Taking these results with xenon as a proxy for other real gases indicates that the excess storage capacity for real gases may be explained by densification of gas within the pore space. However, the results also call into question our assumptions about adsorbed phase properties and raise the question as to whether the densification observed is mechanistically adsorption at all.

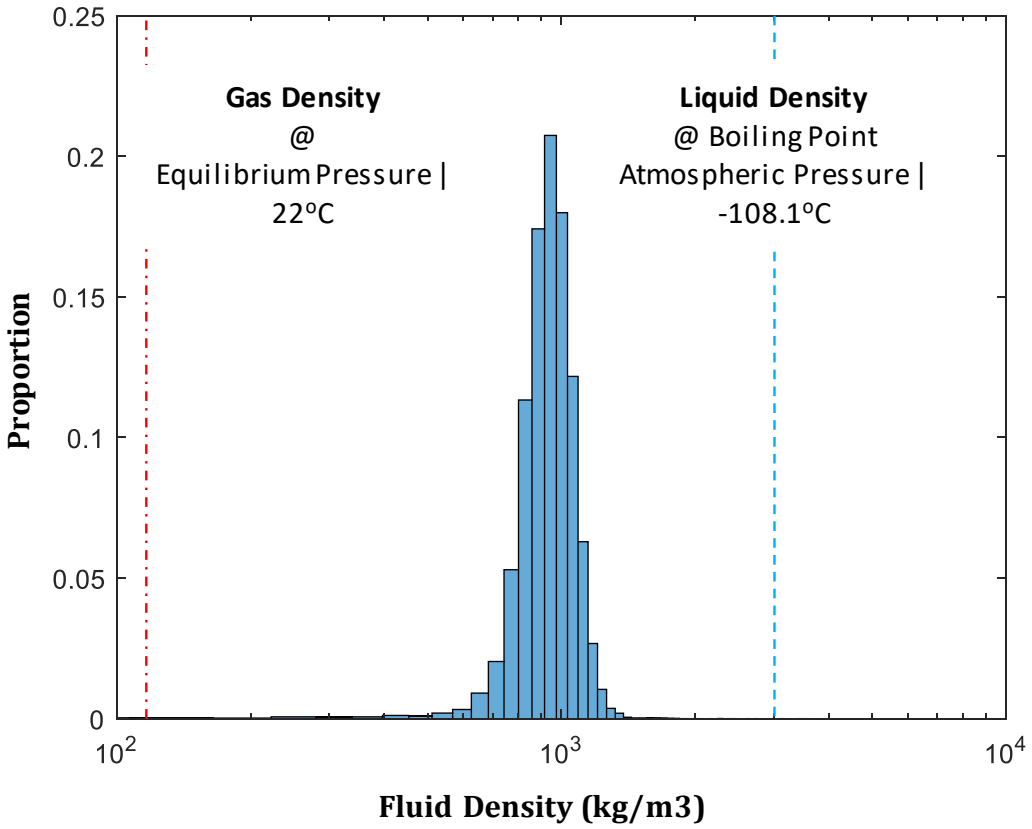

Figure 10: Distribution of xenon density at every voxel location of the Marcellus sample at equilibrium conditions

2.3.2 Porosimetry

Results of pore fluid densities as derived from both porosimetry and CT experiments are discussed in this section. Table 2 lists the expected *free* gas phase densities based on the decline equilibration pressure, as well as the actual *measured* pore fluid density estimated using equation 2.5 (except for xenon, which is estimated using equation 2.4). The densities at critical point (Pc) for the gases used are also provided for reference, as well as the gas relative temperatures (T/Tc) at experimental conditions.

Table 2: Reference and measured fluid densities from porosimetry experiment

	Fluid Density (kg/m3)							
	Methane (T/Tc = 1.55)		Argon (T/Tc = 1.96)		Ethylene (T/Tc = 1.04)		Xenon* (T/Tc = 1.02)	
	ρ_c	162.7	ρ_c	535.9	ρ_c	214.0	ρ_c	1100.0
	free	measured	free	measured	free	measured	free	measured (*from CT)
Bakken	43.5	56.8	103.4	111.7				
Marcellus	55.7	222.7	122.6	486.6	5.7	162.2	128.0	947.0
Haynesville	50.2	108.7	116.0	196.0				
Mancos	54.1	92.9	114.9	184.3				

It can be seen from Table 2 that in all cases the measured density was higher than the reference free gas density at equilibrium pressure. In order to make the results more intuitive, the extent of densification is characterized by a 'densification ratio' given by,

$$\text{Densification ratio } (R_D) = \left(\frac{\rho_g^p}{\rho_g^{free}}\right)_{decline} \tag{2.6}$$

The densification ratio for the different samples for different gases is shown in Figure 11 (A.). A densification ratio of 1 would mean no densification. The lowest amount of densification was observed in the Bakken sample with 30% higher and only 10% higher than expected densities for methane and argon respectively. In all other cases, densification was far more significant and greater than 60%. The greatest extent of densification was observed in the Marcellus sample with measured fluid density in all cases being at least four times higher than expected free gas density. However, the most interesting result was that of ethylene gas which was over 28 times the free gas density. This seems anomalously high at first glance and begs the question as to whether comparing measured density with the expected free-gas density is the most meaningful way of analyzing the data? Figure 11 B. shows the proximity of the measured fluid density to critical density as given by,

$$\text{Critical Proximity } (R_C) = \frac{\rho_g^p}{\rho_g^{critical}} \tag{2.7}$$

Indeed Figure 11 (B.) shows a very different trend especially in the case of the Marcellus sample. For argon, ethylene, and xenon, the ratio is quite similar and close to 1. In fact, it is the methane result that appears anomalously high. One possible reason to explain this behavior might be that the pore fluid is in a near critical state rather than in an adsorbed state. The apparent sorption mentioned previously may actually be due to the densification of the gas in the pore space due to cohesive forces rather than true adsorption where fluid molecules are adhesively attracted to the solid walls. The methane may additionally have a significant component of adhesively sorbed gas at a higher density than the rest of the pore fluid (which might be closer to the critical density). For all other samples the R_C is far below 1. This also raises the question as to whether the mechanism of densification in the Marcellus is different from the mechanism of densification in the Haynesville and Mancos samples, as well as the related question of whether the mechanism of densification of hydrocarbon gases like methane is the same or different from other gases such as noble gases like argon and xenon?

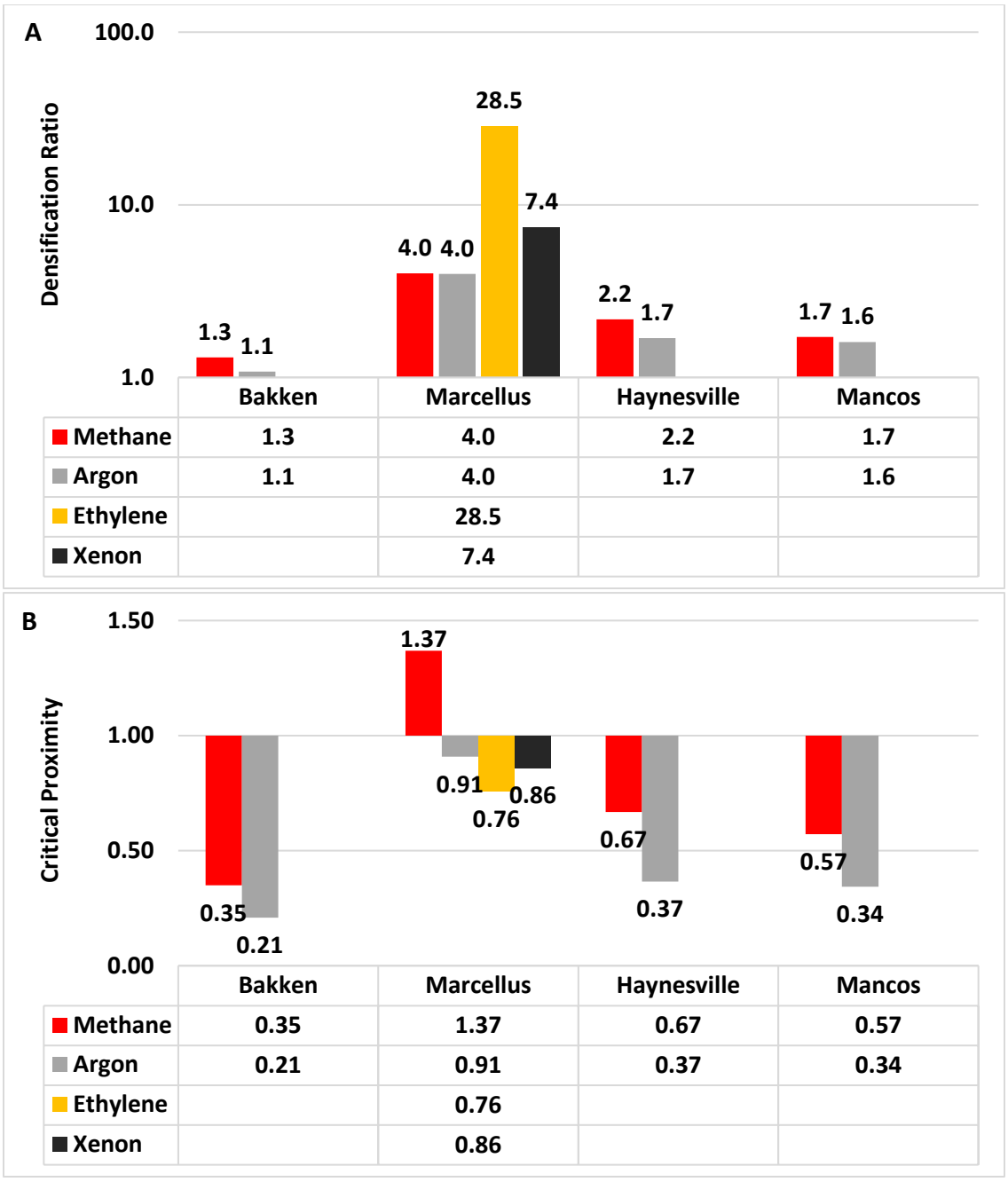

Figure 11: A. (above) Densification ratio; B. (Below) Critical proximity.

2.4 Discussion

Adsorption is defined as the adhesion of fluid molecules to a solid surface. In practice, any quantity of gas uptake by a sample that is in excess of free-gas quantities is considered 'adsorbed.' However, the reality is that excess fluid uptake can take multiple forms. One well-known form of fluid uptake is capillary condensation, wherein gas condenses into a liquid phase at pressures lower than saturation pressure when placed in a confined environment such as in nano-pores (<1μm). This behavior has been clearly and visually demonstrated to occur for single component hydrocarbon gases in mesopores (5-50nm) and even in small macropores (>50nm) in the range of a few hundred nanometers (e.g., Wang et al. 2014; Parsa, Yin, and Ozkan 2015). However, capillary condensation is not adsorption even though it may begin in many cases from local sites of solid-fluid adhesion. Fundamentally, capillary condensation is the predominance of cohesive forces between fluid molecules in confined environments that results in the densification of gas into a liquid state.

Capillary condensation is a good example of altered fluid behavior in confined environments, i.e., condensation at sub-saturation pressures. It has also been shown to be reasonably well predicted by the Kelvin equation (L. Wang et al. 2014; Parsa, Yin, and Ozkan 2015). For shales with predominantly nanopores, clearly, it is important that one considers these differences in fluid properties compared to macroscopic or free fluids. However, the Kelvin equation is only valid for fluids at sub-critical temperatures for which the saturation pressures are well defined. What about fluids above critical temperature where saturation pressure is not defined? What about supercritical fluids which constitute the majority of fluids in an oil or gas reservoir? Does alteration of fluid properties due to confinement stop happening? On the contrary, although a clear interface between the liquid and gas phase does not exist at super-critical temperatures, there continues to exist a transition between gas-like and liquid-like states which can be described by the Frenkel line as shown in Figure 12 (Ghosh and Krishnamurthy 2018).

Another form of excess gas storage or fluid densification is 'Induced-supercriticality'. Induced-supercriticality is the alteration of fluid properties as a whole towards the properties of

supercritical fluids at sub-critical conditions. This has been demonstrated to happen in mesoporous materials by Thommes and Findenegg, 1994 who reported an effective reduction in critical temperature for gaseous SF_6 in mesoporous glasses of 24nm to 31nm. Similar results for several hydrocarbon gases were demonstrated by Luo, Lutkenhaus, and Nasrabadi, 2016.

One way to think about the alteration of fluid properties during either capillary condensation or induced-supercriticality is that the effect of fluid confinement is equivalent to either the reduction in critical temperature or the elevation of experienced pressure. The densification of fluids observed in this study can also be explained in this way, i.e., by assuming that the effect of nanopores is to raise the experienced pressure of pore fluid. This would also be consistent with the basic intuitions of altered fluid properties predicted based on high capillary forces, such as the model proposed by Nojabaei, Johns, and Chu 2013, but without imagining a gas and liquid interface. If indeed the equivalent effect of nanopores is to suppress temperature or elevate pressure then even supercritical fluids at conditions around the Frenkel line are likely to see significant variations in density and storativity within nanoporous shales.

We are thus left with two questions – 1. What mechanism or mechanisms is/are responsible for ‘sorption’ in the context of gas storage in shale?, and 2. Should altered fluid properties in shales be attributed only to capillary forces? More research in these areas is advisable which could have a significant bearing on estimations of gas in place.

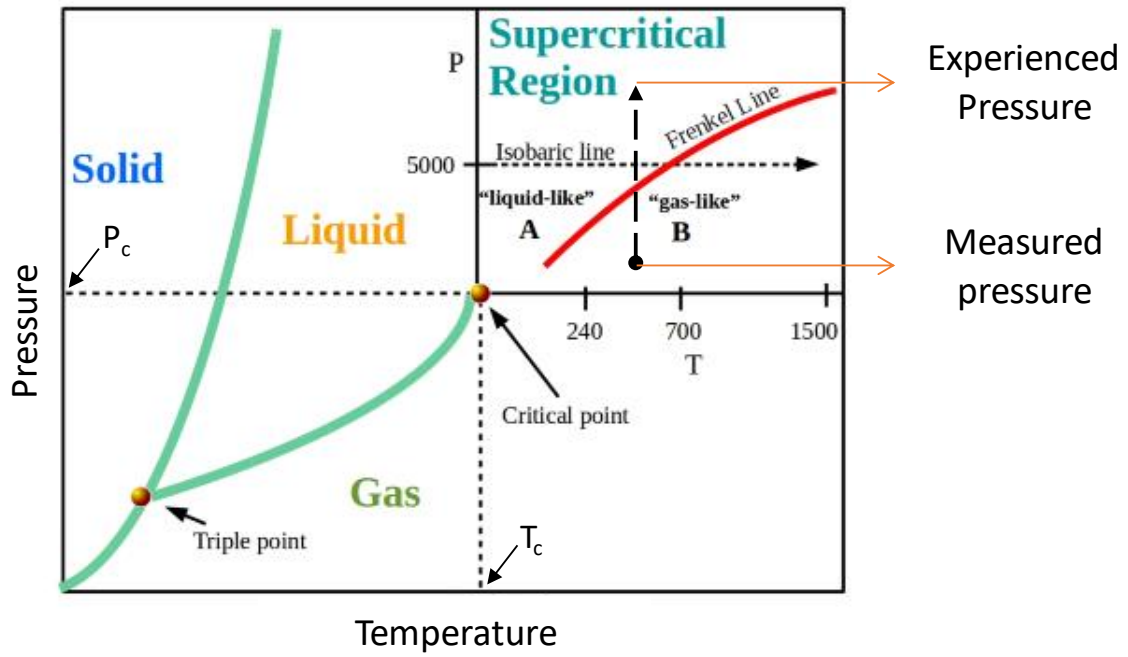

Figure 12: Single component fluid phase behavior diagram modified from Ghosh and Krishnamurthy 2018. One way to explain the densification of pore fluid is that the experienced pressure at equilibrium of pore fluids in higher than surrounding free fluid.

2.5 Conclusions

In this chapter, we investigated the storage behavior of different gaseous fluids in Bakken, Marcellus, Haynesville, and Mancos Shale samples. We demonstrated that the densities of fluid in all cases are higher than would be expected if the fluids were in gas phase at the measured equilibrium conditions. A detailed analysis based on CT data using xenon in the Marcellus sample revealed that the average fluid densities at almost every voxel location of the sample were not only higher than the expected gas density, but also lower than typical assumptions of adsorbed phase density.

The gas densification was characterized in terms of two metrics – the densification ratio, and critical proximity. The results of these metrics varied greatly across shales, and even within the same shale across different gases. This could be indicative of different mechanisms of

densification in the various shale-fluid cases. One notable example was ethylene gas in the Marcellus sample which showed an anomalously high densification ratio of 28.5, whereas other gases were between 4 and 5.2, but critical proximity of 0.76 which was similar to argon and xenon at 0.91 and 0.86 respectively. This suggests that the mode of densification in the Marcellus sample for ethylene, argon, and xenon gases may be induced-supercriticality. These results provoke consideration of the meaning of sorption when evaluating gas storage in nanoporous shales. Results are also indicative of altered fluid properties of single-component fluids within shales. A matter of significance for the industrial exploitation of shale gas is that these observations were made on supercritical fluids and therefore, the underlying mechanisms are likely to be consequential for reservoir conditions.

In the next chapter, we will further characterize the rock fabric and explore underlying compositional or structural reasons that explain the densification of pore fluids in shales.

3: Rock and Fluids Characterization

3.1 Background

In Chapter 1 we learned that the storage of gas in shales extends beyond the quantification of rock porosity, and that sorption could be responsible for significant excess storage capacity. In chapter 2 we learned that the excess storage capacity of shales can express itself in different modalities: adsorption, induced-supercriticality or capillary condensation brought about by pore confinement, which are mechanistically different processes. Adsorption is the result of adhesive forces between fluid molecules and the solid surface and, it is therefore a strong function of the chemical composition of adsorbate fluids and the adsorbent solid. On the other hand, the effects of pore confinement are a function of pore topology and size distribution.

In the past, there have been large scale studies analyzing the petrophysical properties of shales, such as Yang and Aplin 2007 who studied 30 different shale and mudstone formations. However, these studies usually lack a characterization of pore topology and size distribution. Instead, most studies measure traditional petrophysical parameters such as porosity and permeability and some measure adsorption capacities as well. Adsorption capacities have been shown to be high in organic matter surrogates such as coals, charcoals and activated carbons and correlations between high TOC shales and adsorption capacities have been reported (Busch et al. 2008; Ross and Bustin 2009; Kang et al. 2011; Heller and Zoback 2014). Adsorption capacities of clays have also been found to be very high (Busch et al. 2008; Heller and Zoback 2014). The overall consensus currently is that kerogen and organic matter really drives overall fluid storativity in shales. Although a study by Schettler and Parmely 1991 has shown adsorption capacity of kerogens to be much higher than quartz, it isn't clear if this is a chemical effect or a consequence of the microporosity in organic matter. Indeed, a recent more comprehensive study on organic rich shales by Wang et al. 2016 found that microporosity was the key factor controlling methane adsorption and storage.

Even when quantifications of pore size distribution (PSD) are conducted, the most common methods are Cryo-LPSA and MIP. These methods rely on basic assumptions about the state and properties of fluid in the pore space, which as discussed in chapters 1 and 2, may or may not be appropriate. Furthermore, Cryo-LPSA measurements are inapplicable to characterizing large macropores while MIP is a destructive process whose accuracy with fragile and ductile materials like shale, is questionable, especially for nanoporosity. In this chapter, an alternate method using SEM imaging at multiple scales is presented to estimate PSD.

The goal of this chapter is to provide detailed characterization of the shale samples that are the subject of this study. This includes mineralogic composition (XRD), organic content, and pore size distribution (SEM), and surface area (Cryo-LPSA) measurements. The results of the characterization is presented to contextualize the fluid storage results observed in chapters 1 and 2. Finally, CT imaging is used to directly correlate regions of high and low storage with underlying rock composition.

3.2 Compositional Analysis

Compositional analysis consisted of two primary characterization modalities:

1. X-ray Diffraction (XRD), and
2. Total Organic Carbon (TOC)

3.2.1 Mineralogy – X-ray Diffraction (XRD)

In preparation for compositional analysis, each rock type was crushed into two sizes - 270 and 325 mesh - corresponding to maximum particle diameters of less than 53µm and 44µm respectively.

XRD was used to identify mineralogical composition. The diffraction spectra were measured on a PANalytic X-Pert PRO MPD instrument with beam energy set at 45kv-40ma, for a scan range (2θ) of 5-70° and scan time of 20 minutes. The spectra of each rock for 270 mesh and 325 mesh

samples were virtually identical and therefore quantitative analysis of spectrum was only conducted for the 270 mesh. Quantitative analysis was done on Jade software via whole pattern fitting (WPF).

The XRD results are shown in the form of a ternary diagram in Figure 13. Most clay minerals have very similar peak locations on the XRD spectra which makes it challenging to differentiate between various clays in mixed layer clay materials such as shale. Therefore, further differentiation is not presented here. Any minerals, such as dolomites and salts are grouped along with carbonates. The results indicate that all of the samples other than the Mancos were clay rich. The Mancos was structurally the strongest of the shales with almost no fissility and had core integrity similar to a tight sandstone. The XRD also shows a low proportion of clay which explains the structural integrity.

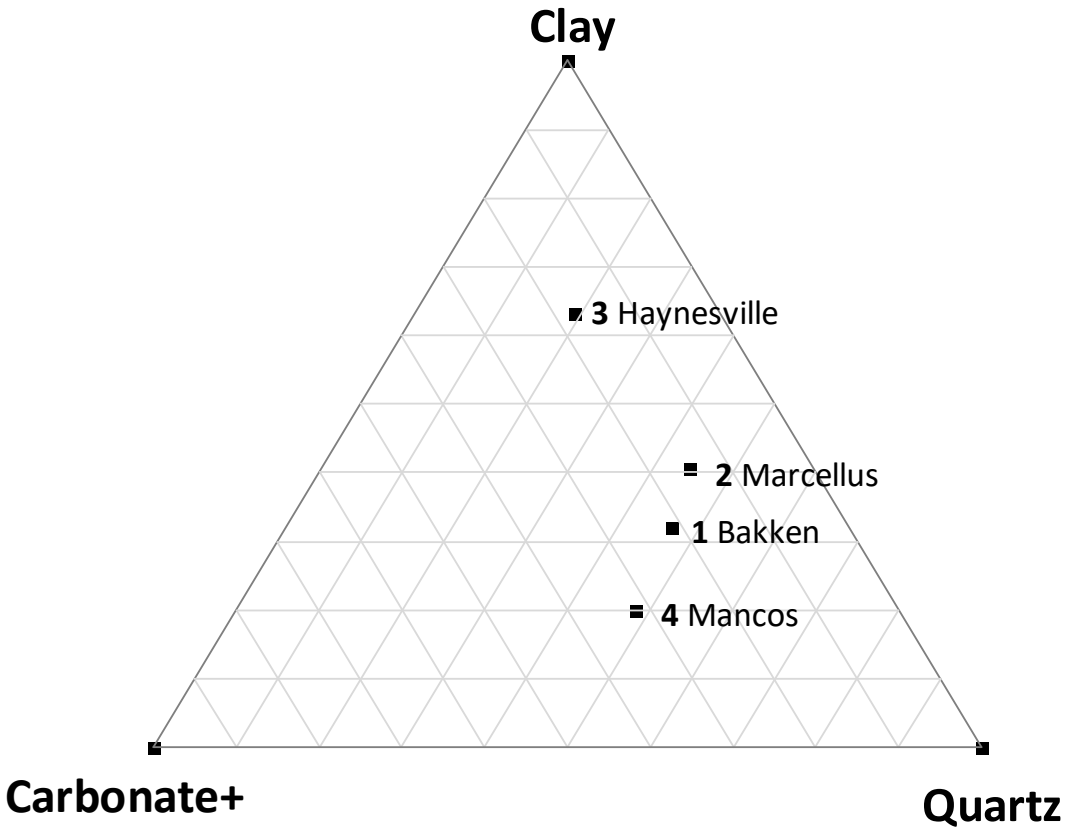

Figure 13: Ternary diagram showing mineralogic composition

3.2.2 Organic Content

Organic content or total organic carbon (TOC) was measured on a Shimadzu TOC analyzer. The crushed rock powder prepared for mineralogy was used as feed for this analysis. All measurements were conducted twice, and the average TOC is reported in Table 3. In general, there was little to no difference between the first and second readings.

It was found that the TOC measured on the Marcellus, Haynesville and Mancos samples were between 3.8 and 5.6%. The Bakken, on the other hand, had almost no organic content. The correlation between sorbed methane measured as measured in section 1.3.2 and of the measured organic content in graphically represented in Figure 14. The correlation was weak with a coefficient of only 0.38.

Table 3: Average TOC Measurements

Sample	TOC%
Marcellus	3.8
Bakken	0.1
Haynesville	5.6
Mancos	4.8

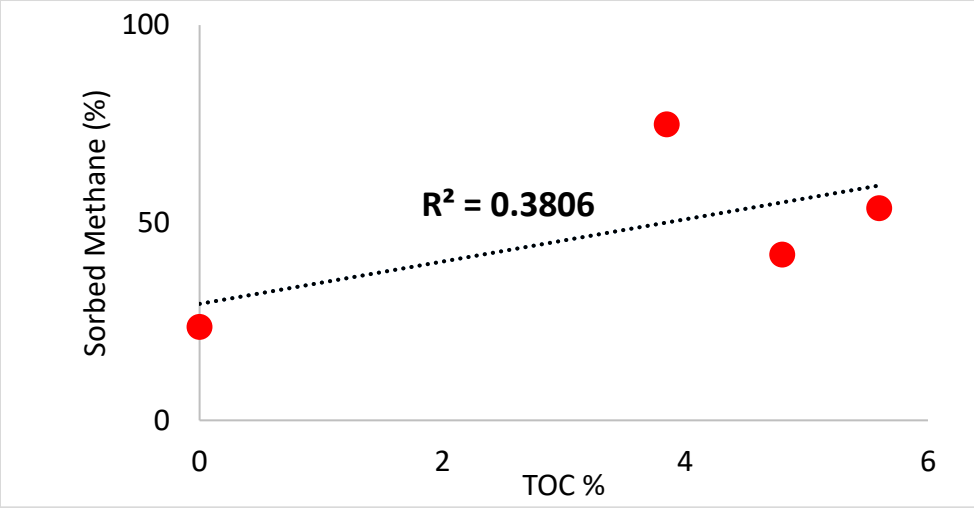

Figure 14: Correlation between sorbed methane content and measured TOC across all four samples indicates a weak correlation

3.3 Pore Structure Analysis

3.3.1 Scanning Electron Microscopy (SEM) Imaging

Given the extremely small particle and pore sizes in shale, SEM imaging is a necessary tool for visual inspection of samples.

Image formation in an SEM is similar to regular visible light images as formed by the human eye or an optical microscope. The key difference is that the wavelength of photons of visible light ranges from 400 to 700nm while electrons range from 0.001 to 1nm. This allows SEM images to have a far greater spatial resolution than optical microscopes. The imaging involves the focusing of a beam of electrons onto the target material to be imaged, and the reflections of the electrons are captured by the detector. The electron beam is continuously steered across the field of view of interest and is why the instrument is called a "Scanning" electron microscope. The electron reflection intensity data is collected by a detector and associated with the corresponding location of the scanning electron beam at any given moment. In this way, a map of the electron reflection intensity is created for the user's region of interest which is the resultant SEM image. In this way, the SEM imaging modality makes no assumptions about sample character, and there is little to no alteration of raw intensity data in the process of image formation. It is, therefore, an excellent starting point for the inspection and characterization of shales. Figure 15 (a) is an image of a Marcellus shale sample. Clay platelets are visible as preferentially oriented parallel sheets or collapsed sheets that form curtains obscuring the view of most framework minerals. To overcome this problem, samples used for quantitative analysis were cured in low exothermic clear transparent epoxy for 24hours and mechanically polished with alumina micro-polish of 0.05um. This helped maintain sample integrity whilst creating a smooth surface for imaging. This method of polishing also provided a wide area available for quantitative imaging compared to other approaches like Focused-Ion-Beam (FIB) milling which only yield a few square microns of polished

surface. Figure 15 (b) is a panel of images from a polished Marcellus shale sample acquired at different scales with compositional features and porosity clearly visible.

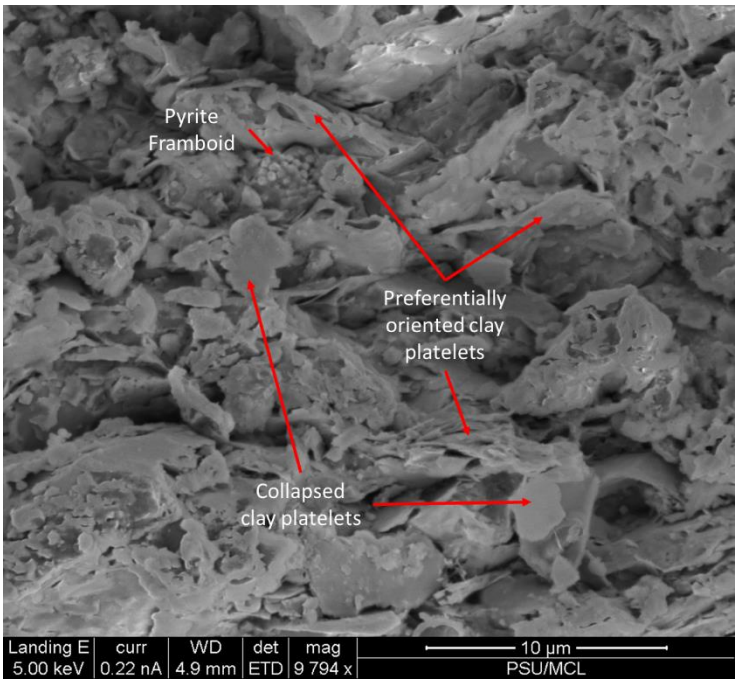

(a)

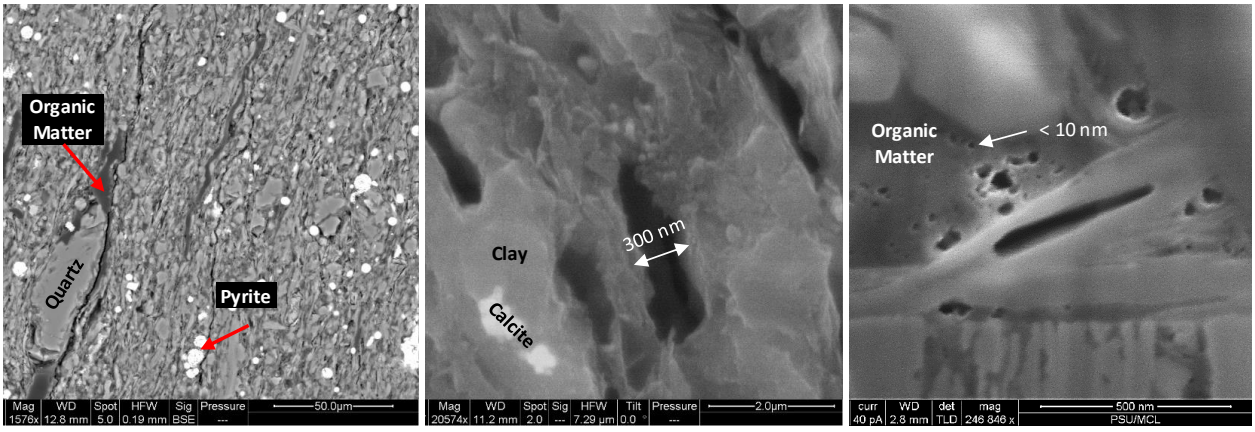

(b)

Figure 15: (a) SEM image of an unpolished Marcellus sample. Collapsed clay platelets (curtains) obscure the view of larger minerals and pores; (b) Images from a polished Marcellus shale sample at different length scales including distinctive porosity at high resolutions.

In addition to helping with qualitative visual interpretations, digital images can also be used to derive quantitative information through the use of image processing techniques. The study of pores in porous materials such as rock is one such example of quantitative information from images. Pores can be seen on well-polished SEM images, and the image processing techniques can be used to infer quantitative information about them, such as size, prevalence, variety etc. Although pores and porosity are inherently 3D features, SEM images nevertheless provide a good first estimate of pore size and structure. SEM images are significantly quicker and cheaper to acquire than 3D CT images and, with current technology, can provide far greater spatial resolution (up to 1nm).

The SEM images acquired in this study were processed using the image processing software Avizo. Three primary processing steps were applied as follows,

1. The images were filtered to reduce image noise. The non-local means filter was found to be the most suitable because the amount of real information lost in the filtration process was negligible.
2. Portions (pixels) of the image that indicated porosity were identified and marked out in a binarization process called *segmentation*. Each image was different and, accordingly, the details of segmentation varied as needed. In general, some combination of *interactive thresholding* and *Sobel filtering* was applied, as needed, to achieve the most accurate segmentation of pores. This process was subjective as it relied on the interpretation of the operator to visually confirm that the pores had been correctly identified. Figure 16 shows the original image and results at the end of steps 1 and 2.
3. The sizes of the segmented pores were calculated by computing the equivalent diameter of continuous regions of connected areal porosity.

Since pores in shale can be as small as a few nanometers, it was important to get images at high spatial resolution. However, in order to obtain higher resolution images, one has to zoom into smaller regions of the sample, thereby reducing the overall field of view (FOV). This can mean that large macropores may not be fully captured by high-resolution images. For this reason,

zoomed-in images at high resolution, as well as images with wider FOV were acquired for every sample.

It is also important to point out here that spatial resolution is not the same as the pixel resolution of an image. In order to differentiate between image noise artifacts and true image features with reasonable confidence, a clearly observable spatial object should ideally be at least 5 pixels long. This sets a lower threshold to the smallest reliably identifiable (after segmentation) pore at greater than approximately 5 times the pixel resolution. The highest resolution image acquired was on a zoomed-in Haynesville image, at 2.3nm. Therefore, only pore sizes larger than 10nm are reported. Unfortunately, this means that micropores and small mesopores (<10nm) were not quantitatively identifiable in this study.

Figure 17 shows the PSD obtained at each scale for each shale sample analyzed. For the Marcellus and Haynesville samples, no pores were visible at very wide FOVs (>1mm). However, the Bakken did have extremely large macropores, of the order of several microns. For this reason, an 'ultra-wide' scale of imaging was required to capture the full range of pore sizes in the Bakken.

Results from Mancos sample are not presented here. This is because the Mancos was a highly heterogeneous sample and identifying representative 2D planar regions was a major challenge. Results from the Mancos sample are discussed in a different context in a later section on CT imaging.

MARCELLUS:

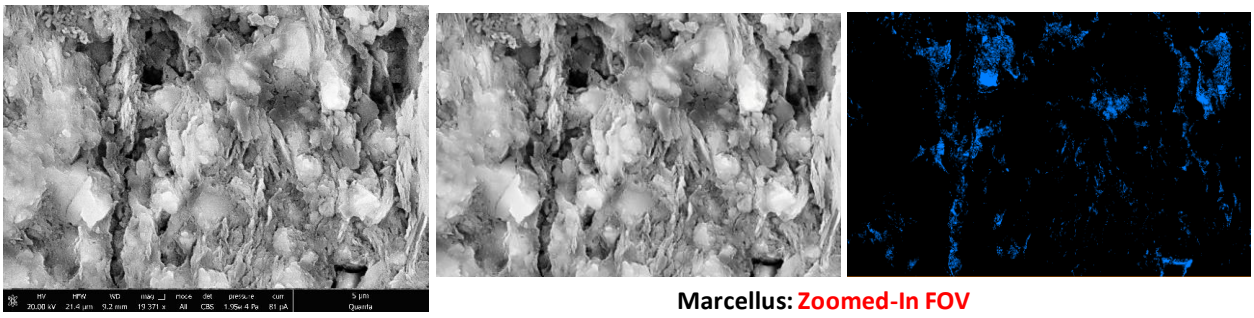

Marcellus: Zoomed-In FOV

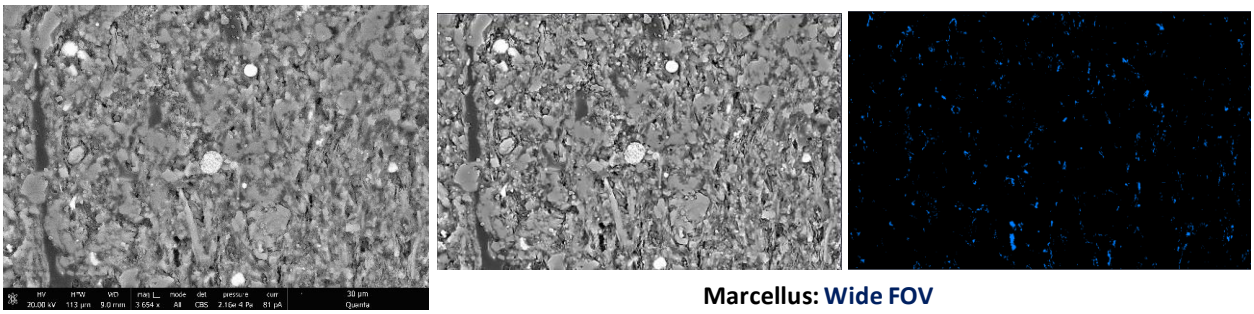

Marcellus: Wide FOV

HAYNESVILLE:

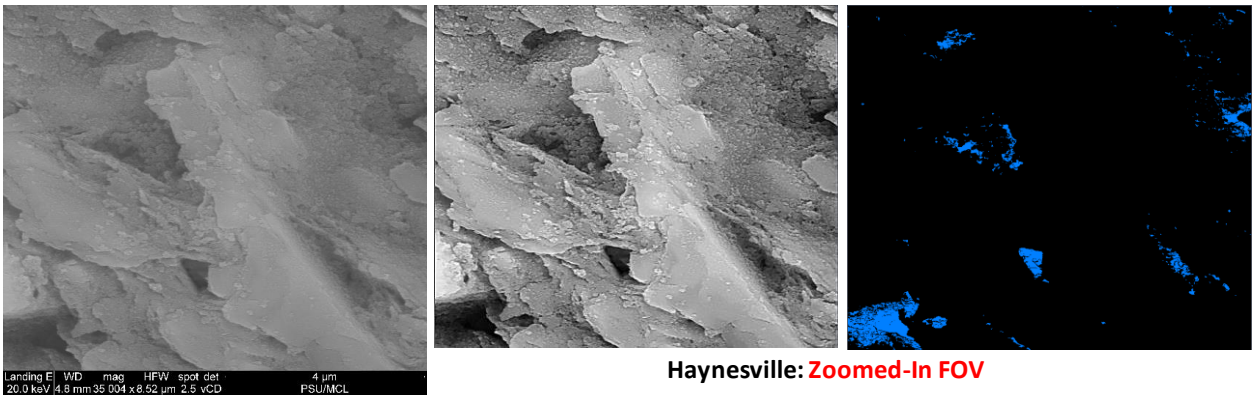

Haynesville: Zoomed-In FOV

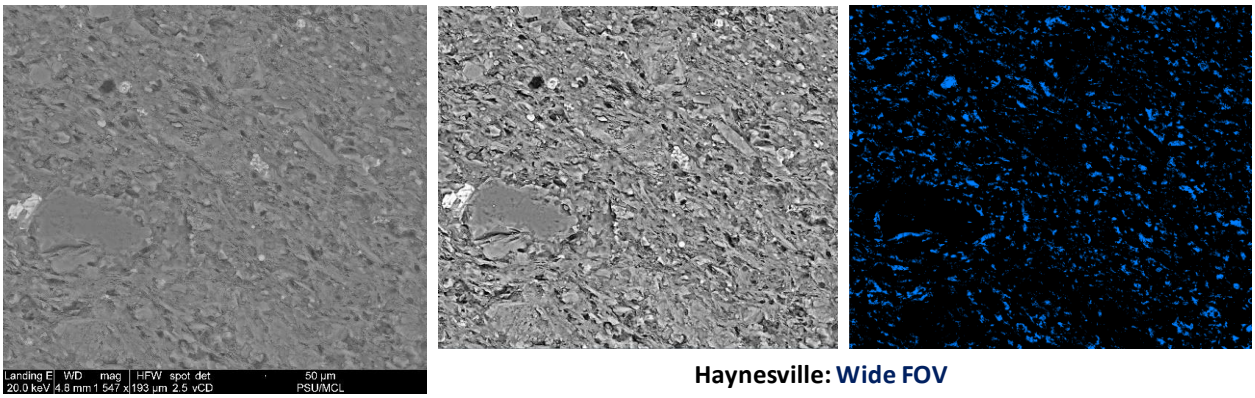

Haynesville: Wide FOV

BAKKEN:

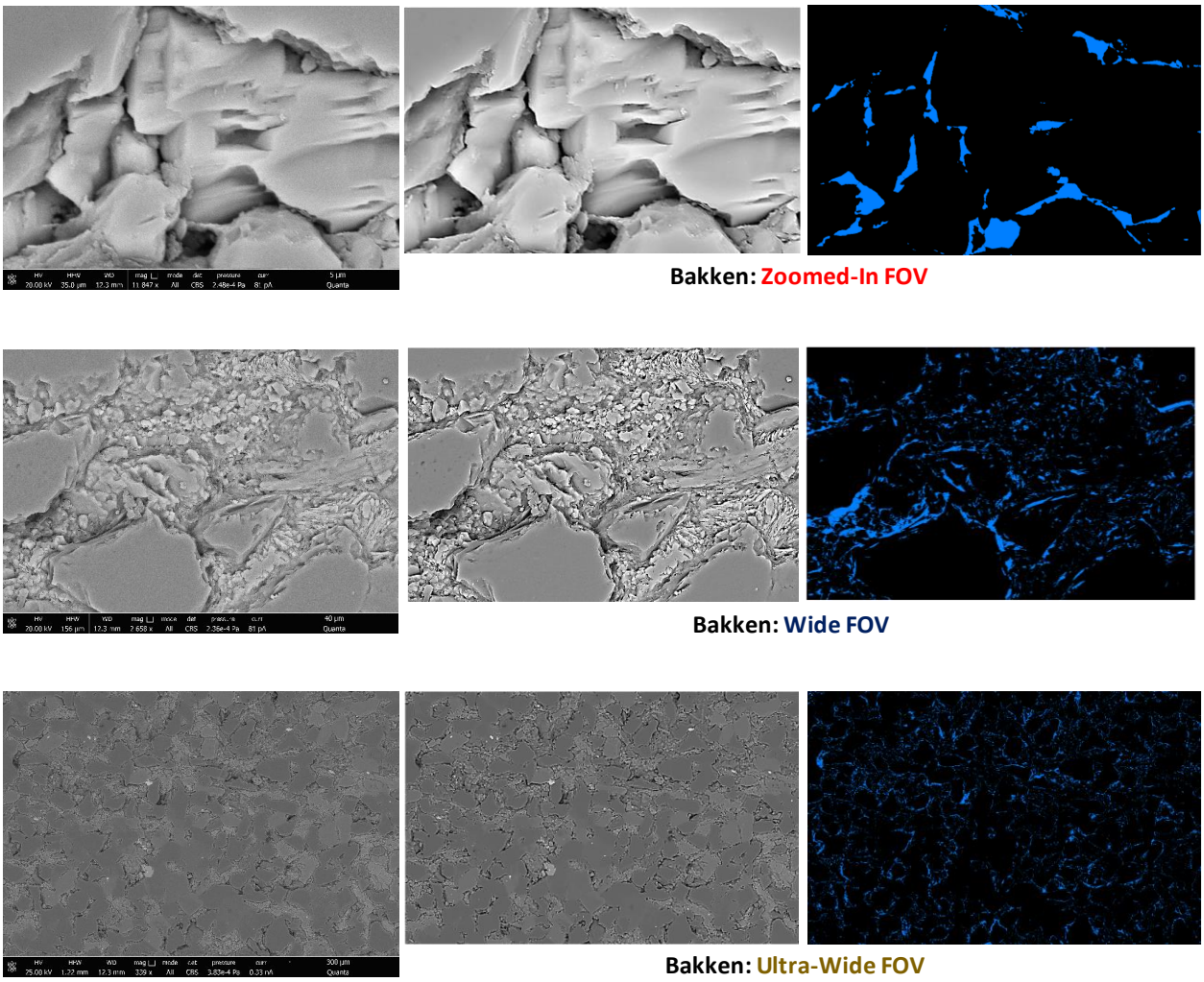

Figure 16: (left) Original image; (middle) Filtered image; (right) Blue regions indicating identified pore pixels

Figure 17 represents the PSD in the form of total area per pore size. In order to bring data from multiple scales of observation into a consistently comparable form, the areas have been normalized as follows,

$$(Normalized\ Area)_i = \frac{(Pore\ Area)_i}{Image\ Area} \tag{3.1}$$

Where, $(Pore\ Area)_i$ is the total area occupied by all pores of size i; $Image\ Area$ is the total areal FOV of the image.

The PSD was very different for the Marcellus and Haynesville samples with no obvious peaks appearing in the range of pore sizes identified. The largest propensity of pores were small mesopores. This is consistent with the observation of these samples being extremely low in permeability.

The Bakken sample had the largest pores with almost no nano-porosity. It had a bimodal distribution of pores around 1μm and 10μm. Both kinds of pores appeared to be intergranular with the latter appearing to be mostly pores between large quartz and feldspathic grains. The smaller pores appeared to be amongst the smaller carbonate grains.

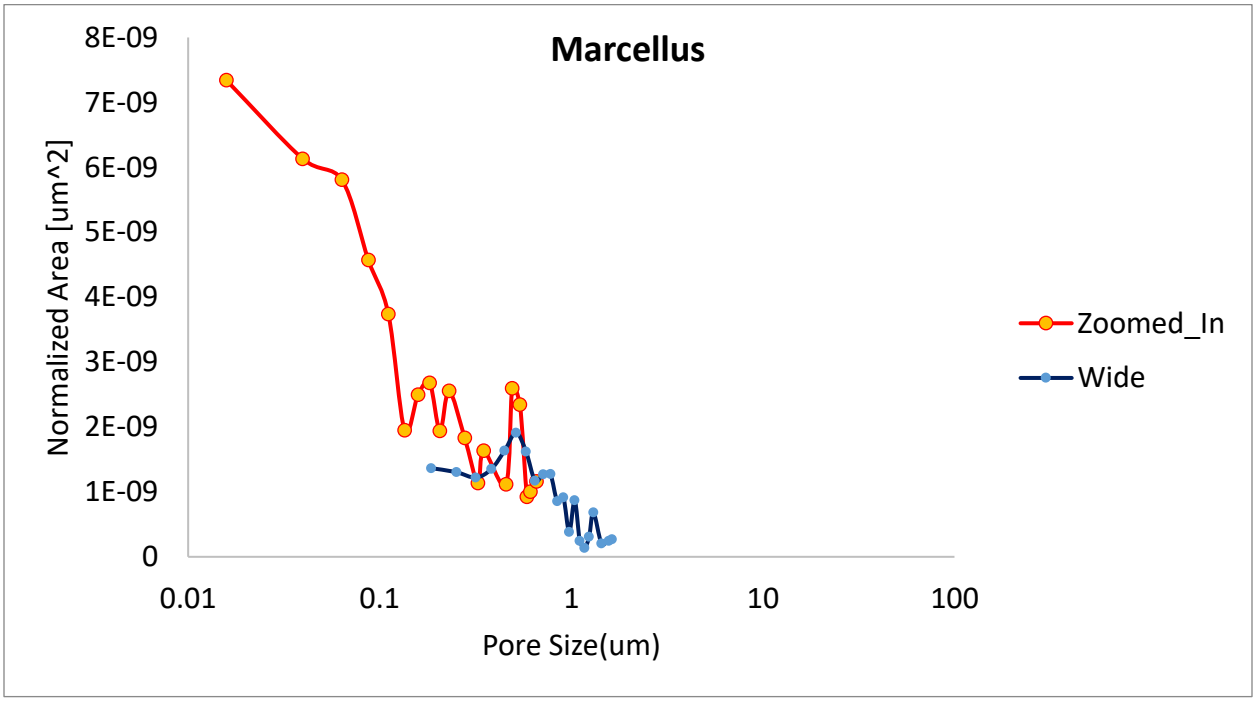

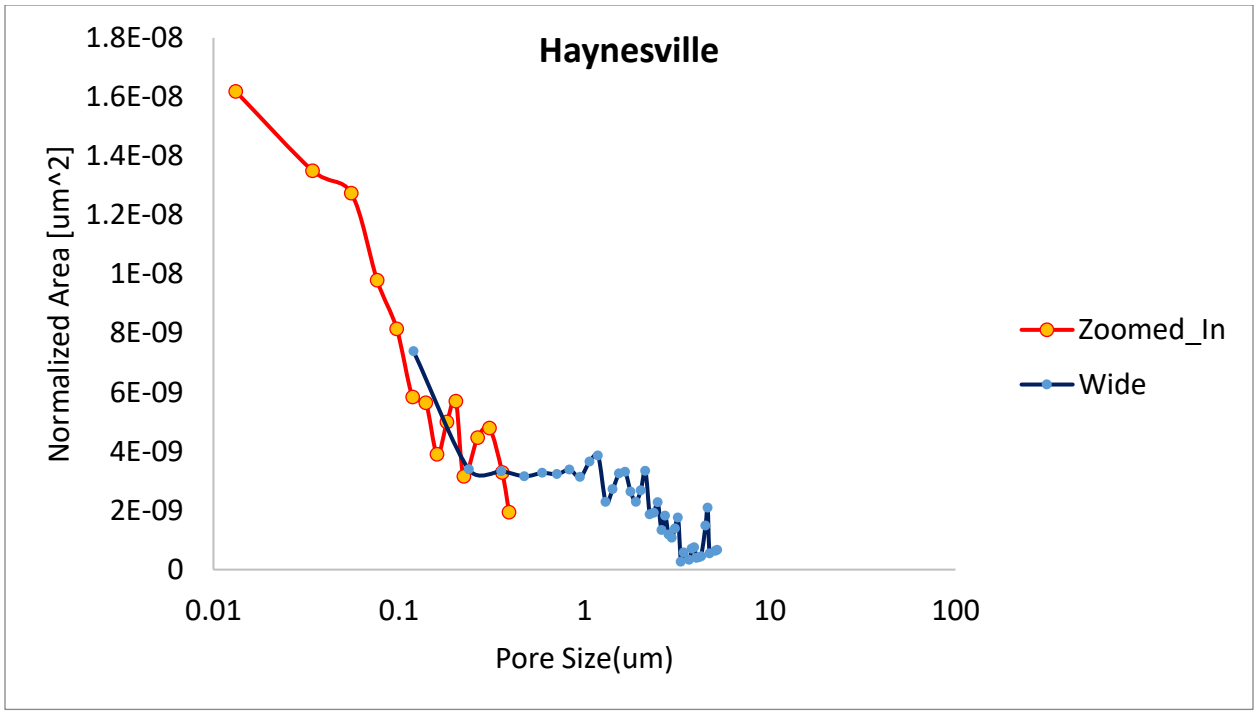

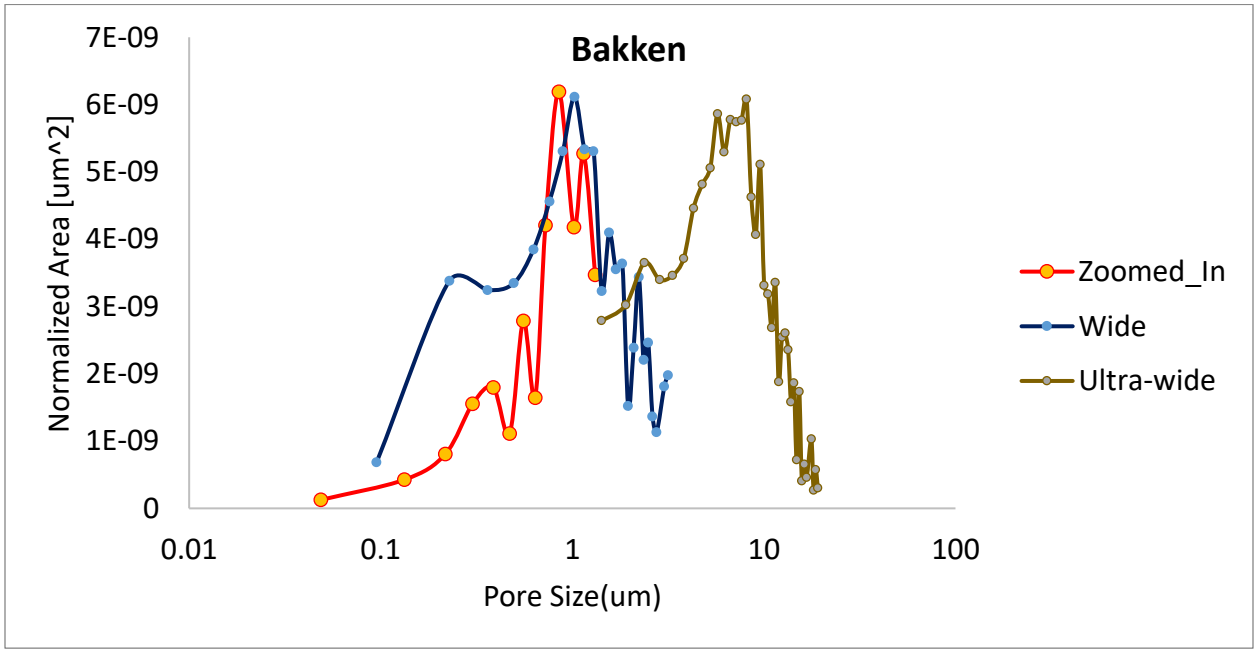

Figure 17: PSD acquired from SEM imaging

3.3.2 Cryo-LPSA

One of the most popular ways of characterizing nanoporosity in micro and mesoporous materials is Low-Pressure Surface Adsorption (LPSA) at boiling point temperature of nitrogen (Cychosz and Thommes 2018). The shape of the adsorption isotherm, as well as the hysteresis between the adsorption branch and desorption branches of the isotherm, reveal information about both pore characteristics as well as fluid behavior.

Figure 18 shows the classification of different types of adsorption isotherms as well as classifications of hysteresis loops. As per the IUPAC classification, adsorption isotherms of type I are indicative of microporous materials. Types II and IV are indicative of non-porous or macroporous materials. Types III and IV indicate materials with low adsorptions capacities wherein the adsorptive fluid molecules have a greater affinity for one another than for the solid adsorbent. Such isotherms provide little information about the underlying structure of the porous medium. Type VI is a theoretical isotherm corresponding to a nonporous material with a uniform surface (K. S. W. Sing et al. 1985; Webb and Orr 1997).

Figure 18 also shows the classification of different types of hysteresis loops related to isotherms of types I, II and IV. According to K. S. W. Sing and Williams 2004, hysteresis loops of types H1 and H2 are indicative of rigid mesoporous materials and have well-defined plateaus at high relative pressures. Types H3 are indicative of aggregates of platy particles such as clays and are linked with a non-rigid underlying pore structure. Type H4 loops are indicative of micropore filling followed by multilayer sorption and capillary condensation. In this way, they are indicative of materials that simultaneously have micro and macroporosity.

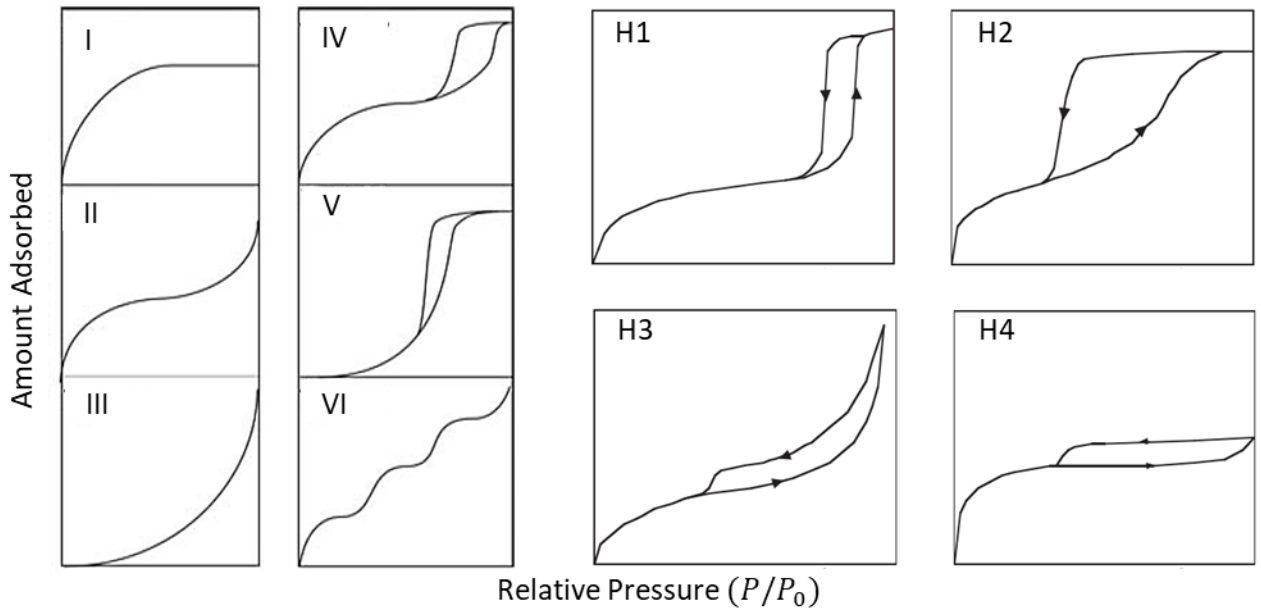

Figure 18: IUPAC classifications for: (left) types of Adsorption isotherms (modified from K. S. W. Sing et al. 1985); (right) types of Hysteresis loops (modified from Sing and Williams 2004)

The data acquisition process for the nitrogen adsorption-desorption isotherms (ADI) was similar to the process described in section 1.2.2. The only difference was that the measurements were carried out in a liquid nitrogen bath at 77K (-195.8°C). Figure 19 shows the measured ADIs for the Marcellus, Haynesville and Bakken samples. The Marcellus and Haynesville samples had qualitatively similar ADIs with hysteresis loop of type H3 indicating granular and platy pores. This fits with the high clay content estimated in these samples during compositional analysis in section 3.2.1 as well as with visual observation on SEM images. The Marcellus had a much greater initial rise in adsorbed content to around 6cm^3/g-STP compared to the Haynesville's 3cm^3/g-STP at P/P_0<0.1. This indicates a higher proportion of microporosity in the Marcellus than the Haynesville. As a general rule, a relative pressure of 0.3 is considered to be the upper limit for monolayer adsorption, and the adsorbed quantities at higher pressures are due to multilayer adsorption and capillary condensation. The hysteresis band, i.e. the difference between the

desorption and adsorption branches between $0.5 < P/P_0 < 0.8$ is indicative of mesoporosity. This band was narrower in the Marcellus sample compared to the Haynesville indicating a smaller proportion of mesoporosity in the Marcellus. At P/P_0 from 0.8 to 1 the rapid rise in adsorbed content due to pore filling from capillary condensation. This rise is slower in the Marcellus, going from around 9cm^3/g-STP to 11, whereas the Haynesville went from around 4cm^3/g-STP to 10cm^3/g-STP. This indicates lesser capillary condensation in the Marcellus than the Haynesville meaning that the Marcellus has less macroporosity than the Haynesville. The Bakken sample, on the other hand, had a completely different type of ADI resembling a type III isotherm. This indicates very low adsorption affinity for the underlying minerals. This too is consistent with the high quartz and carbonate, and low clay nature of the Bakken sample as reported in section 3.2.1. The Bakken sample has the most rapid rise in adsorbed content at high relative pressures 0.8 to 1 indicating that almost all the porosity is macroporosity.

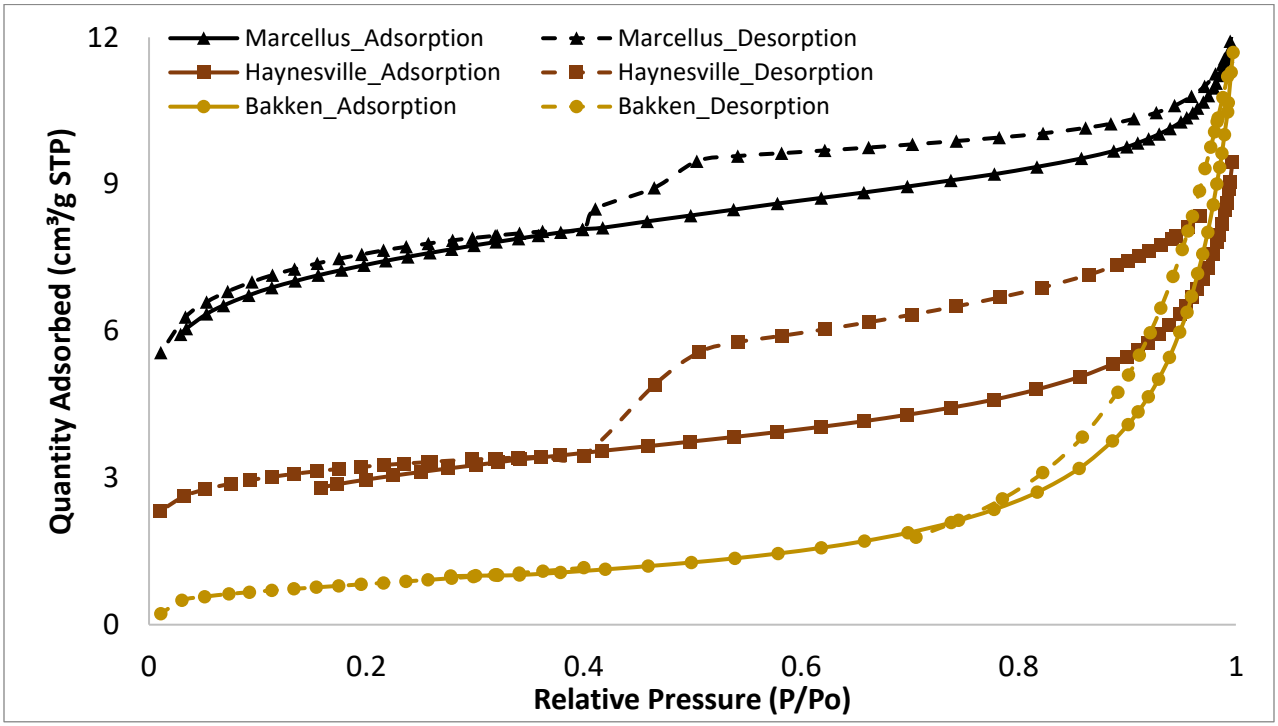

Figure 19: Cryo LPSA ADIs measured for the Marcellus, Haynesville and Bakken samples

In addition to the qualitative interpretations discussed above, ADIs can also be used to gather quantitative information about porosity. The Brunauer-Emmett-Teller (BET) model is a commonly applied model to estimate surface area from adsorption data. The BET model is a multilayer sorption model that assumes that the formation of the adsorbed monolayer can be followed by multiple layers of adsorbed fluid based on the latent heat of liquefaction of the adsorbate molecules. The model is mathematically described by the following equation,

$$\frac{1}{v_a\left(\frac{p_0}{p}-1\right)} = \frac{1}{v_m C} + \frac{C-1}{v_m C}\left(\frac{p}{p_0}\right) \tag{3.2}$$

where, v_a is the measured adsorbed gas specific volume at a given relative pressure; v_m is the specific volume of a monolayer; and C is a constant.

The specific surface area of the adsorbent can be calculated as follows,

$$SA = \left(\frac{v_m}{22.4}\right) * A_{MC} * N_A \tag{3.3}$$

where, SA is adsorbent specific surface area, A_{MC} is the molecular cross-sectional area of the adsorbate molecule ($A_{MC}^{nitrogen} = 0.162nm^2$), N_A is Avogadro's constant.

While applying the BET model, only relative pressure values less than 0.09 were used because using data up to 0.3 was resulting in negative C values. However, this did not make a major difference to the ultimate surface area calculations. The results of BET analysis is given in Table 4. The Marcellus had the highest surface area at 28.5m^2/g, most likely because of its high microporosity. The Haynesville with its higher meso and macro-porosity had a lower specific surface area of 12m^2/g, and the Bakken had a very low specific surface area of only 2.9m^2/g.

Table 4: Results of BET analysis

	Slope $\frac{C-1}{v_m C}$	**Intercept** $\frac{1}{v_m C}$	**C**	v_m **(cm^3/g)**	**SA (m^2/g)**
Marcellus	0.153	0.0004	381.0	6.533	28.5
Haynesville	0.361	0.0011	324.2	2.764	12.0

Bakken	1.499	0.0174	87.1	0.659	2.9

LPSA data can also be used to compute pore size distribution via Barrett-Joyner-Halenda (BJH) or Non-Local Density Functional Theory (NLDFT) models. This approach has been applied by some shale researchers (e.g., Alnoaimi and Kovscek 2013). However, it is extremely critical to point out here that LPSA isotherm data is not a reliable quantitative indicator of macropore sizes, and grossly underestimates their prevalence (J. Rouquerol et al. 1994; Jean Rouquerol et al. 2012). It is altogether inapplicable for pore size greater than 100nm because the pore size is much larger than the adsorbed layer thicknesses. Given the prevalence of macropores noted in all samples via direct SEM imaging (section 3.3.1), the application of LPSA for pore size distribution calculations is considered inaccurate and unreliable and is, therefore, not reported.

3.3.2.1 Relationship with Methane Sorption from Porosimetry

The surface area estimations from BET can help provide intuition for the room temperature methane sorption results presented in section 1.3.2.

The monolayer capacity for methane in the different shales can be calculated from their BET surface areas as follows,

$$q_m^{methane} = \frac{SA}{A_{MC}^{methane} * N_A} \tag{3.4}$$

Where, $q_m^{methane}$ is the monolayer capacity of methane in a particular shale, SA is the BET surface area of that shale sample, $A_{MC}^{methane}$ is the molecular cross-sectional area of methane ($A_{MC}^{methane} = 0.28nm^2$), N_A is Avogadro's constant.

Given the quantities adsorbed in a monolayer, the number of such layers required to explain the total quantities of sorbed methane observed in the porosimetry (section 1.3.2) experiments can be calculated as,

$$Layers\ Needed = \frac{(q_{total})_{porosimetry}}{q_m^{methane}} \quad (3.5)$$

Table 5 shows the summary of the sorption capacities estimated from porosimetry, as well as estimates based on a single monolayer coverage of methane molecules on the available surface area. The number of required layers based on equation 3.5 is also provided. The results indicate that the existence of between 2.35 layers for the Bakken to 3.69 layers for the Haynesville would explain the sorption quantities measured during porosimetry. A reference 'trilayer' calculation is provided for adsorbed quantities if there was full coverage of the available surface with exactly three layers. The trilayer calculation is a highly idealized estimate because subsequent layers following the monolayer usually don't result in complete surface coverage. In fact, the mathematical BET model is itself premised on the possibility of an infinite number of adsorbed layers. Therefore, the number of layers calculated do not explicitly represent physical reality. Nevertheless, it provides basic intuition for how the sorbed quantities might be distributed in the shales samples. This is represented graphically in Figure 20.

Table 5: Room temperature Methane adsorption capacity estimates:

Porosimetry vs. BET based

	Porosimetry (mmol/g)	**BET Area Based Monolayer [q_m] (mmol/g)**	**BET Area Based Trilayer [3*q_m] (mmol/g)**	**BET Layers needed**
Marcellus	0.457	0.160	0.480	2.85
Haynesville	0.219	0.059	0.178	3.69
Bakken	0.041	0.018	0.053	2.35

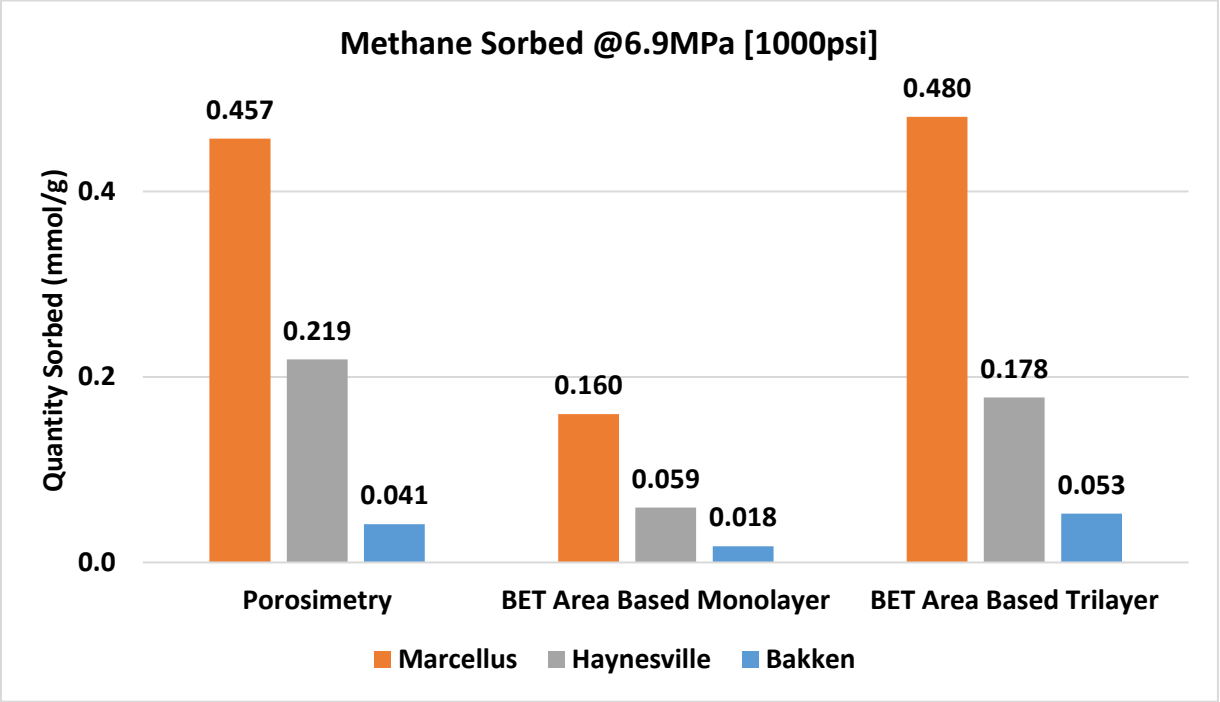

Figure 20: Estimates of sorbed gas quantities based on porosimetry and BET surface area.

3.3.3 CT Imaging

The experimental procedure for CT imaging has been described in section 2.2.1. In this section, we will discuss the results of imaging with xenon as probe gas on a Marcellus and a Mancos sample. The goal of imaging was to identify regions of gas storage and correlate it with underlying fabric.

Marcellus

Figure 21 shows a horizontal patch of the Marcellus sample in the *fresh* state and the computed xenon density for that patch at *equilibrium*. The darkest patches in the fresh grayscale image likely represent high organic content regions or high porosity regions. The corresponding xenon density map shows that these "black" patches are sites of maximum xenon density of over 1600kg/m^3. Intermediate grayscale regions which make up the majority of the map, and are likely clay rich, show densities over 800kg/m^3. Bright white regions indicating the presence of dense

minerals such as carbonates or pyrites appear to correspond to low xenon density. The reader will recall from section 2.3.1 that the expected xenon density was 181kg/m^3.

The results indicate that the carbonate-rich regions and pyrite framboids appear to have low gas storage. Carbonates and pyrites are typically macroporous with large intergranular porosity. The lack of gas uptake at these sites is also indicative of low adsorption capacities and the gas in these regions could be mostly free gas, hence the lower density. The high xenon densities in the organic-rich regions could be explained by both the high adsorption capacity expected of kerogen as well as their microporosity. The microporosity results in very high surface area to volume ratios in these regions, thus enhancing adsorption, thereby increasing xenon density. But the most interesting observation is the high xenon densities in the clay-quartz rich regions. Clay/quartz rich regions make up most of the matrix. High xenon density in these regions implies either that they too have high adsorption capacities. This is surprising because quartz minerals are generally known to have low adsorption capacities. Therefore, one way to explain the high storage is that the adsorption on the clays is very high. Another possibility is that the high gas uptake is a function of altered fluid behavior in the mesoporosity of the clay platelets and/or the fine-grained

quartz grains. In either case the high amounts of gas storage mean that the sorption capacity of these sites is an important component of overall GIP.

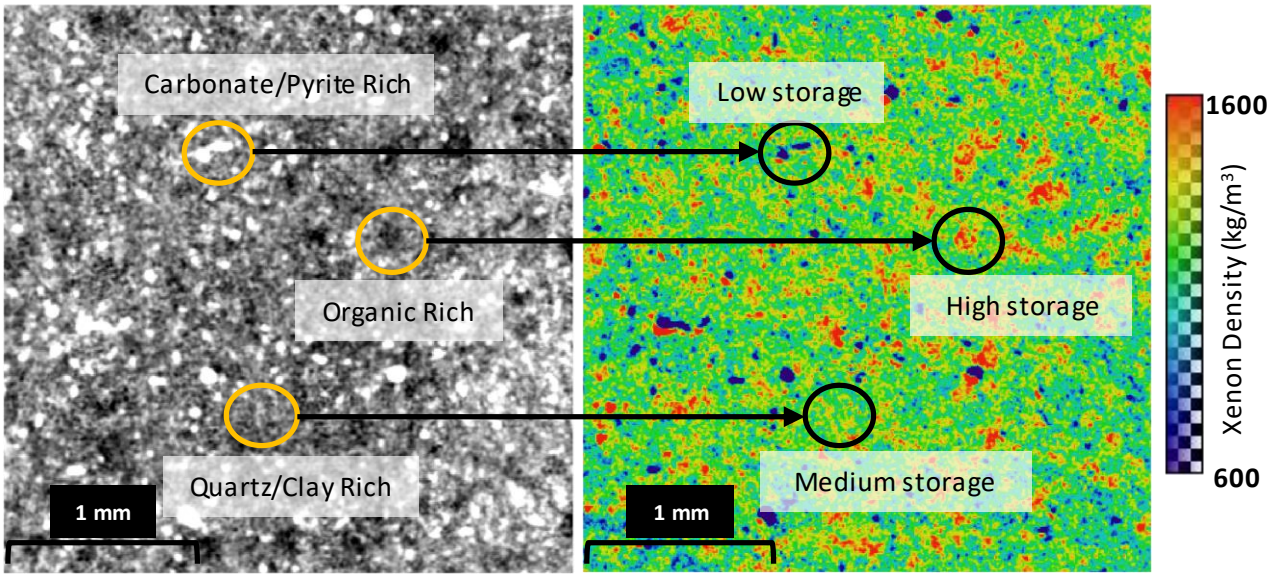

Figure 21: (left) CT slice of Marcellus sample at *fresh* conditions, (right) density map of xenon at *equilibrium* conditions

Mancos

Just like with the Marcellus, the Mancos too was imaged as a pair of stacked plugs separated by a hollow spacer. Figure 23 shows the results of CT imaging with xenon gas on a Mancos sample. The equivalent porosity was calculated using equation 2.2. The average equivalent porosity for the sample was 12.24%. The reader will recall that the porosity estimate from Helium porosimetry (section 1.3.1) was around 5%. This higher equivalent porosity calculated from X-ray CT could indicate densification of xenon in the Mancos pore system.

The Mancos was a layered system and finding a representative slice was challenging. Therefore, correlations of gas storage with underlying composition is shown in Figure 23 as a cross plot of the CT numbers (Linear Attenuation) before xenon injection (pre-injection) against the calculated xenon equivalent porosity. Each point on the graph is an average across a horizontal cross-sectional slice of the sample. Regions of high linear attenuation correspond to slices with more

dense minerals while lower linear attenuation corresponds to lighter layers such as highly porous or organic rich layers. In general, the cross-plot indicates high equivalent porosity in regions with low linear attenuation and lower equivalent porosity in regions with high linear attenuation. Assuming that dense minerals are associated with large macroporosity, the low equivalent porosities in these regions indicate that (1.) real macroscopic porosity is small, on the order of around 6%., which fits with the helium porosimetry results for the Mancos; and (2.) the adsorption capacities of dense minerals is likely low. High equivalent porosities in regions indicating lighter minerals and possibly high organic content, shows that sorption may be the key driver of xenon uptake.

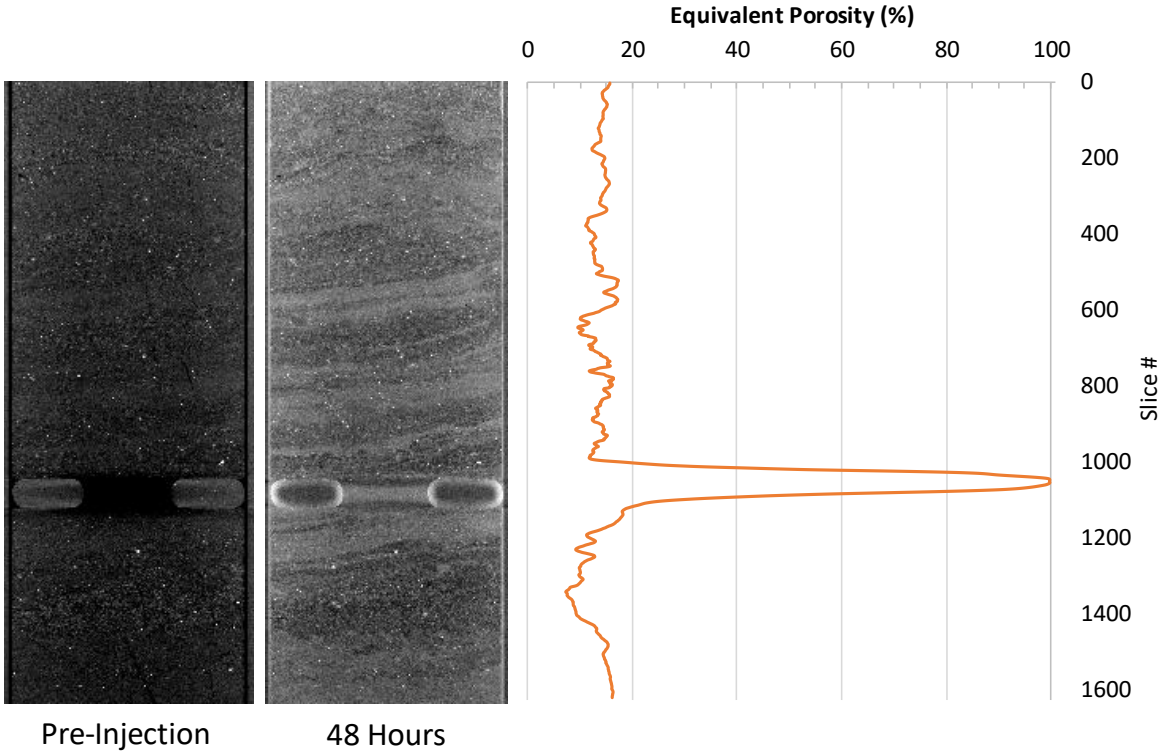

Figure 22: Results of CT imaging of the Mancos sample with xenon gas

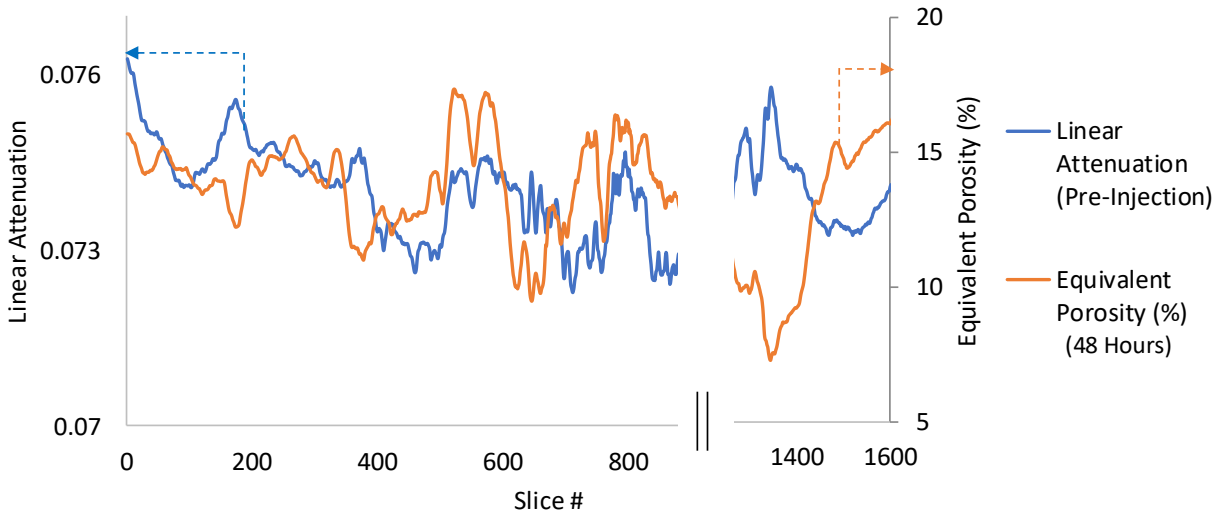

Figure 23: Cross plot between the raw CT number (linear attenuation) of the Mancos sample at pre-injection condition against the equivalent porosity calculated based on the xenon filled images at 48 hours. Regions with high linear attenuation indicate a predominance of dense minerals, while lower linear attenuation indicates organic rich layers.

3.4 Discussion

The main value of the results presented in this chapter is to contextualize the gas storage and phase behavior described in chapters 1 and 2. The reader will recall from chapter 1 that the highest storage capacities for real gases was found in the Marcellus sample due to enhanced gas uptake beyond free gas. The enhanced uptake was seen to a high but slightly lesser degree in the Hayneville, further less in the Mancos, and was minimal in the case of the Bakken.

Compositional analysis can explain this behavior to some extent. All the samples which showed enhanced gas uptake, i.e. the Marcellus, Haynesville, and Mancos, had significant amounts of organic content, whereas the Bakken didn't. However, this wasn't a perfect correlation because the Marcellus had lower TOC than both the Haynesville and the Mancos and yet had the highest gas storativity. This means that adsorption on organic content alone may not explain gas adsorption and enhanced storage in shales. Clay content was not good indicator either as Bakken

sample was comparable in mineralogy to the Mancos, yet showed extremely different gas storage behavior.

Pore structure analysis was a better explanator of storage. Both SEM and Cryo-LPSA indicated high proportion of nanoporosity in the Marcellus and Haynesville samples, and virtually no nanoporosity in the Bakken. This raises the possibility that available specific surface area may be one of the better indicators of sorption capacity. Indeed, BET surface areas covered in 2 to 4 layers of adsorbent was shown to explain perfectly the sorbed methane estimates reported in section 1.3.2. However, an important caveat is that the BET surface area estimate was derived from nitrogen gas adsorption at cryogenic temperature while the methane sorption measurements were conducted at room temperature. At room temperature, methane is above critical temperature and theoretically supercritical at experimental pressure and temperature conditions. The formation of multiple adsorbed layers is, in effect, a liquefaction process. This is conceptually tenuous for supercritical fluids. But do the results indicate that this is indeed the case? The highest number of layers required to explain the sorbed gas quantities was 3.7 for the Haynesville sample, which was also interpreted to have the highest proportion of mesoporosity. This leaves open the question raised in chapter 2 that the enhanced uptake could be due to a mechanistically different process to sorption. Such alternatives include induced-supercriticality in mesopores, or a process similar to capillary condensation but for supercritical fluids.

Large scale direct imaging using X-ray CT confirmed many of the interpretations drawn from compositional and pore size analysis. The regions with high probability of organic content in both the Marcellus and Mancos samples were the regions with the highest xenon uptake. However, excess uptake of gas was generally widespread, even in regions likely to be quartz/clay rich,

further fueling the speculation that pore size or surface area may be the primary driver to gas uptake.

3.5 Conclusions

In this chapter, we reported careful characterization of the shale samples used in this study in order to understand and contextualize the gas storage and fluid phase behaviors observed in chapters 1 and 2. The samples in this study were found to represent a fair amount of compositional diversity, including mineralogic and organic content diversity. The pore size distributions were also significantly different between Marcellus and Haynesville, and the Bakken. The key takeaways from the results reported in this chapter are,

1. In general, high organic content was found to be weakly correlated (R=0.36) with enhanced gas storage and there was no clear correlation with other mineralogy either. This was visually supported by CT imaging which indicated high storage in most parts of a Marcellus except at dense-mineral-rich sites.
2. Pore size distribution and pore surface areas were found to be good indicators of storage. However, porosity and pore volumes were not.
3. Cross-correlation of Nitrogen LPSA BET SSA data and porosimetry data indicated a multilayer sorption mechanism. However, questions on whether multilayer adsorption is really possible in supercritical fluids leaves room for alternate mechanistic explanations for the gas storage observed.

4: Impact of Gas Densification on Transport

Preface

Portions of the work presented in this chapter have been published in the following article,

> **Zhang, M., Chakraborty, N., Karpyn, Z., Emami-Meybodi, H., and Ayala, L. 2019** "Numerical and Experimental Analysis of Diffusion and Sorption Kinetics Effects in Marcellus Shale Gas Transport" in *SPE Reservoir Simulation Conference 2019*

The contributions of my co-authors are gratefully acknowledged.

4.1 Background

In the previous chapters, we have seen evidence of gas densification in most of the shales studied. Regardless of the mechanism of the densification process, it would seem reasonable to wonder about the implications of the densification process on fluid transport behavior in shales.

Normally, fluid transport in geologic materials is represented by the Darcy equation (Hubbert 1957). In reality, gas transport is a combination of at least four types of mechanisms (Mason and Malinauskas 1983): 1) Darcy flow - viscous flow in which gas flows as a continuum fluid driven by the total pressure gradient; 2) Continuum Diffusion - continuum transport of gas according to chemical potential gradients, such as temperature or concentration gradients, arising from collisions among fluid molecules of different types; 3) Knudsen Diffusion - Free molecular diffusion caused by collision of gas molecules with solid pore walls; 4) Surface Diffusion – adsorbed gas moves along the solid surface, and is usually a precursor to multilayer adsorption or capillary condensation (Caravella 2016).

Viscous flow dominates gas transport in large macropores where pore diameters are much larger than molecular mean free path. This makes up the vast majority of conventional oil and gas reservoir rock such as sandstones and limestones, as well as some shales such as the Bakken (with pores mostly >1μm). This is why the Darcy equation works so well in most hydrology and petroleum engineering related applications. As pore diameters start to get smaller, such as in

shales, molecular mean free path starts to become comparable to, or, larger than pore diameter, and Knudsen diffusion starts to play a more significant role. In micropores and mesopores with strong adsorption affinity, surface diffusion plays a critical role in total gas transport (Hwang and Kammermeyer 1966).

Given their nanoporous structure, there has been longstanding cognizance in the petroleum engineering community to account for the complexity of fluid transport phenomenon in unconventional tight reservoirs such as coalbed methane and shale (Thimons and Kissell 1973; Turgay Ertekin, King, and Schwerer 1986; Javadpour 2009; Wu et al. 2015). These studies have, in turn, drawn on the vast catalog of studies on gas transport behavior in microporous media in general (Carman and Raal 1951; Mason and Malinauskas 1983; Do 1998; Siemons, Wolf, and Bruining 2007; Fathi and Akkutlu 2012). The Dusty-Gas Model (DGM) (Mason and Malinauskas 1983) is a popular and comprehensive multi-mechanistic model for multicomponent fluid flow through porous membranes which treats the porous medium as simply the $N+1^{th}$ component consisting of large molecules fixed in space. The application of the DGM to geologic media has been historically limited although it has become more popular in recent years (Chen et al. 2015; Wang et al. 2016; Shen et al. 2018). Instead, a more common approach has been to modify the traditional diffusivity equation to account for apparent micro-scale effects (Ertekin, King, and Schwerer 1986; Javadpour 2009; Wu et al. 2015). For instance, Ertekin, King, and Schwerer, 1986, proposed a coupled viscous flow and diffusion model and suggested that Knudsen diffusion was the reason for the so-called Klinkenberg effect in natural gas engineering and proposed to model it by modifying the apparent permeability via an apparent gas slippage factor. Ertekin and Sung, 1989, also took into account adsorption by assuming it to always be at equilibrium and applying the adsorption isotherm. More recently Fathi and Akkutlu, 2009, 2012, introduced kinetic models of sorption and surface diffusion of sorbed gas to the gas transport equations.

A key issue with the development of models has been the lack of availability of appropriate experimental data on key parameters such as in-situ concentrations, surface diffusion coefficients, and adsorption kinetics. In addition to other parameters such as permeability and

bulk diffusion coefficients, most parameters have to be indirectly inferred from bulk pressure and flow rate data (Carman and Raal 1951; Thimons and Kissell 1973; Siemons, Wolf, and Bruining 2007). The sensitivity of X-ray attenuation to density and density changes makes it a promising tool to quantitatively analyze transport dynamics in shales. X-ray CT imaging has been successfully applied to quantitively evaluate adsorption kinetics for the case of CO_2 sequestration in coals (Karacan 2003) in which transport diffusivity was also estimated but in terms of a combined (surface and bulk) value based on an indirect method proposed by Gray and Do (1992).

In this current work, X-ray CT data has been purposefully acquired in order to develop a more direct method for the estimation of diffusion and sorption kinetic parameters with the help of a purpose-built numerical model. The proposed numerical model is a system of two governing equations written for free and sorbed gas phase transport. 3D transient in-situ pore fluid density propagation profiles obtained from CT imaging is used to match against the simulated density transients. Bulk diffusivity, surface diffusivity, as well as sorption rate coefficients are individually obtained from the history matching.

4.2 Methodology

4.2.1 Experimental Overview

The experimental data used in this chapter were obtained from the X-ray CT imaging of the Marcellus sample described in detail in section 2.2.1, and will be recapped briefly. Xenon gas was injected at 2.84MPa into a 12mm diameter Marcellus shale plug mounted in a pressure vessel. The pressure vessel was shut-in immediately upon injection of gas, and the resultant pressure fall-off over time was recorded as gas from the annular space was slowly taken up by the sample. X-ray CT images were periodically collected for the first 58hours in order to capture the transient stages of xenon propagation into the sample. Another single 3D image was collected after 30days in order to capture the complete pressure and concentration equilibrium state (Figure 9 in Section 2.3.1). Figure 24 shows vertical cross-sectional snapshots of the sample at different times following injection of xenon. The transient progression of xenon into the sample from the

sample's external faces and fractures can be seen in the form of regional brightening of the sample. For the first 58hours after xenon injection the propagation of xenon in a small, approximately 2mm tall, portion of the upper plug was observed to be almost radial. This region was numerically extracted for closer observation. Figure 25 shows horizontal cross-sections from this *extraction region*. It can be visually verified that the propagation of the xenon was indeed approximately radial for 58hours.

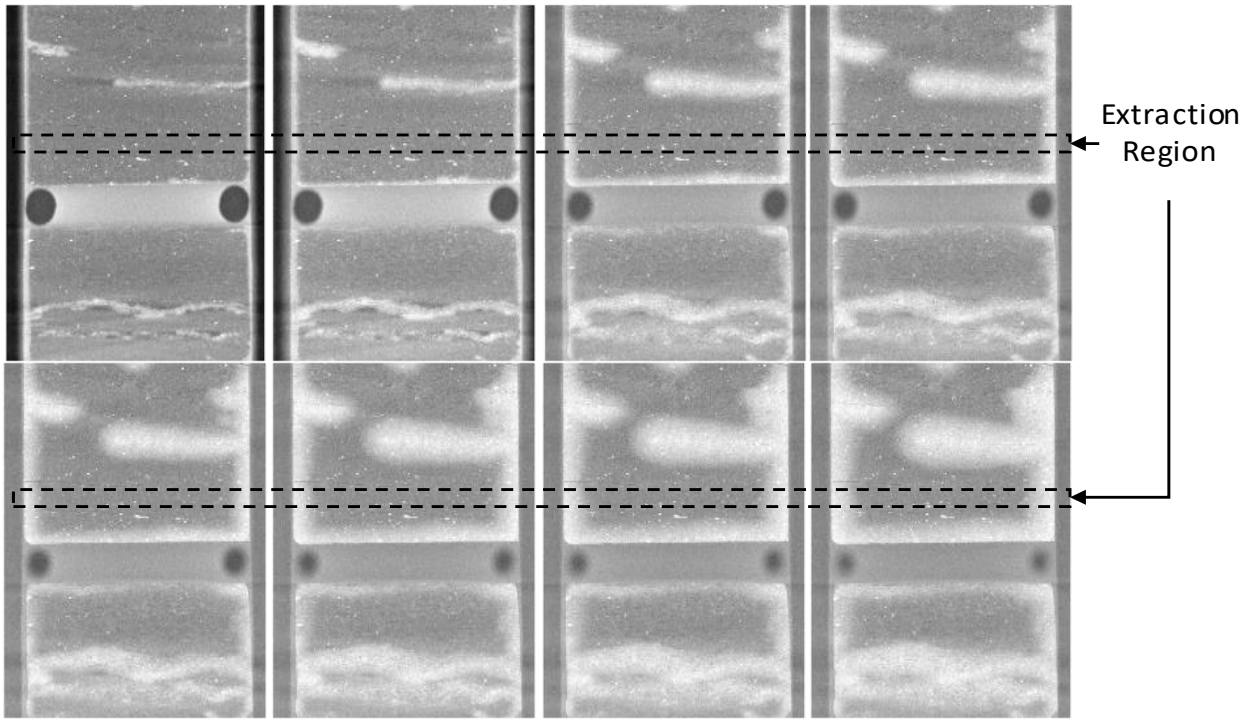

Figure 24: Vertical Cross-Section of the Marcellus sample after xenon injection at (from top left) 0, 5, 14, 19, 26, 39, 48, and 58hr, respectively. The continuous bright white regions indicate the presence of xenon. The black rectangle shows the numerically extracted region where xenon progression was approximately radial for 58hours (Figure 25)

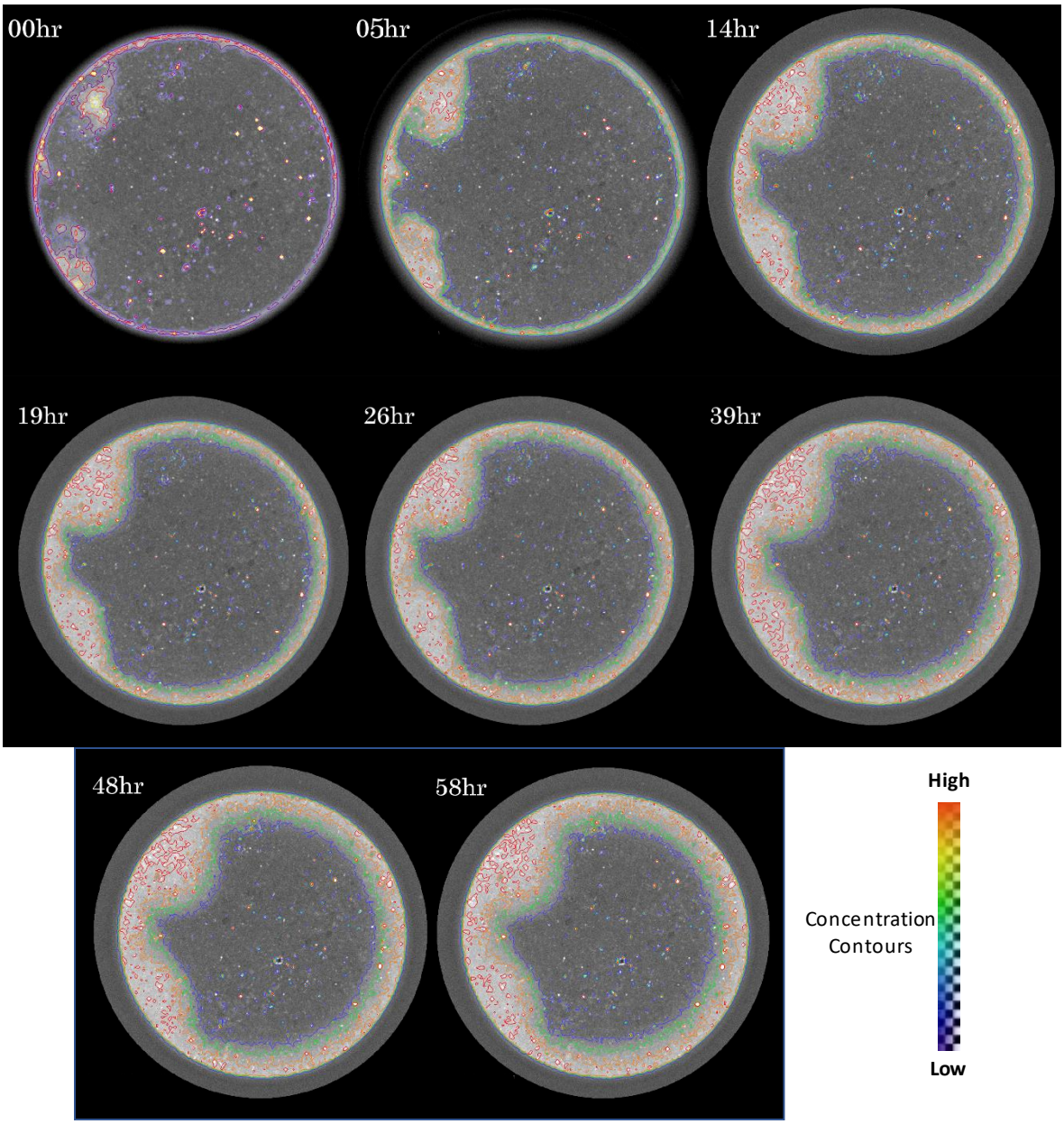

Figure 25: 2D horizontal cross-sections of the Marcellus sample from the 'extraction region shown in Figure 24. Contour lines represent xenon concentration at different times. The progression in this region was considered approximately radial for the first 58 hours after xenon injection.

Figure 26 shows the quantitative data acquired from the experiment – 1) the pressure fall-off over time, and 2) the fluid density as a function of radius. X-ray CT data is a function of the density of the material being imaged. Accordingly, the change in X-ray CT numbers between the fresh state (before xenon injection) image and the equilibrium state image is a function of xenon

density. Change in raw X-ray CT data was mapped to xenon density according to a modified version of equation 2.4 given by,

$$\rho_{\mathrm{Xenon}}^{\mathrm{t}} = \frac{\left(CT_{matrix}^{t} - CT_{matrix}^{@fresh}\right)}{(a + b * Z_{Xenon}^{3})} \tag{4.1}$$

Where, ρ_{Xenon}^{t} is the xenon density at time t; CT_{matrix}^{t} is the CT image for the corresponding time t.

As opposed to the real fluid density calculated according to equation 2.4, the density calculated by equation 4.1 is not corrected for sample porosity and as such represents density if xenon were to occupy the entire bulk volume of the sample. These are reported as average radial profiles shown in Figure 26. The average density was calculated along concentric vertical cylindrical surfaces of unit voxel (voxel size of 13.8μm) thickness. This simplifies the 3D data into an effective 1D radial system. The point of origin represents density data for a line passing vertically through the center of the sample, while the maximum value of the x-axis represents average density on the outer circular surface of a hollow cylinder passing along the radial edge of the sample. The reader will note that the measured density is highest a few millimeters inwards from the outer radius of the sample. This is because on the outer radius, gas within pores has closer proximity and even possible exposure to free gas in the annulus, and therefore, is likely to have a higher rate of desorption compared to gas deeper inside. This prevents the sorbed gas concentration on the boundary from rising to the same level as in deeper regions of the sample. Another observation is that there is very slow rise in the gas density near the center of the sample, and this density is never found to be zero. This is likely because within the first few minutes to hours of gas injection high-permeability pathways and connected macropores are rapidly filled by free gas. However, sorption being a kinetically controlled process is much slower. Therefore, the majority of the gas migrates deep into the sample as a slow advancing front made up overwhelmingly of sorbed gas. This could indicate that advective flow ceases to play a major role fairly early in the course of the entire experiment.

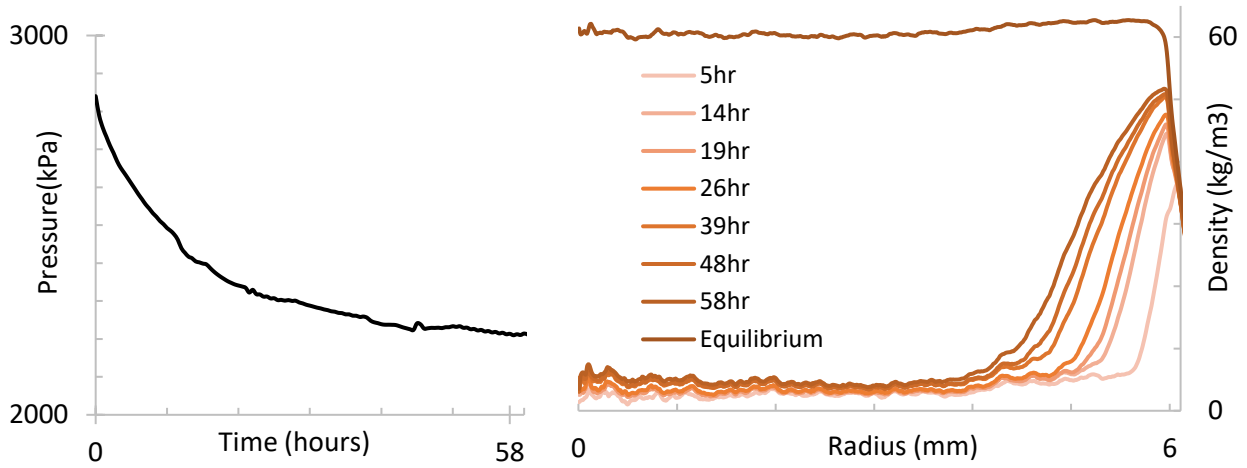

Figure 26: (left) Measured pressure fall-off after xenon injection. (right) Average density of xenon in the sample as a function of radius

4.2.2 Numerical Model

Mass transport of single-component gas in nanopores is a combination of free-gas viscous (Darcy) flow, Knudsen diffusion, and sorbed gas surface diffusion. The transport equations developed in this work are written for free and sorbed gas, and take into account adsorption kinetics and concentration-dependent surface diffusivity (Figure 27). The primary assumptions in the development are,

1. Single component (group of similar molecules) gas transport is studied, and thus ordinary diffusion is not considered.
2. Dissolved gas is ignored because the available experimental data was acquired in dry rock with no initial oil or water saturation.
3. The Langmuir model of monolayer gas adsorption is applied. However, in order to eliminate pore surface area from the formulation, the sorbed phase is represented in terms of mass per unit solid volume following Do (1998).
4. Isothermal conditions – Temperature dependence of diffusion/sorption is not considered.
5. The porous medium is considered homogenous.

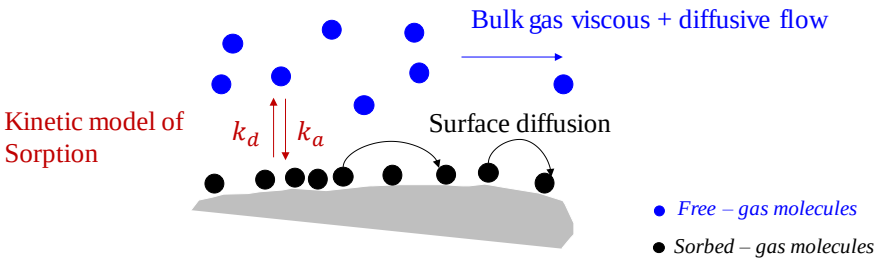

Figure 27: Gas transport mechanisms and effects considered in the model

4.2.2.1 Transport Equations for Free and Sorbed Gas

For a pure component system, concentration of free-phase gas is equal to its density (ρ_g),

$$C = \rho_g \tag{4.2}$$

Viscous flux of free gas is given by Darcy's law,

$$J_v = -\rho_g \frac{k}{\mu_g} \nabla p \tag{4.3}$$

where *k* is absolute permeability of the porous media, μ_g denotes gas viscosity.

Knudsen diffusion flux caused by gas molecules' collision with pore walls is given by Fick's first law as,

$$J_K = -D_K \nabla C \tag{4.4}$$

where D_k is the Knudsen diffusion diffusivity, C is the concentration of the free phase gas in mass per unit gas volume.

Combining equations 4.2 –4.4 with mass conservation principles for the entire porous media domain, the transport equation for free phase gas is given by,

$$\nabla \left[\left\{ D_{k,eff} + \frac{k}{\mu_g c_g} \right\} \nabla C \right] = \frac{\partial (\phi C)}{\partial t} - R_m \tag{4.5}$$

where ϕ is the porosity of the formation, and the fractional volume occupied by free-phase gas, $D_{k,eff}$ gives the effective Knudsen diffusivity based on the total cross-sectional area of the porous media, $c_g = \frac{1}{\rho_g}\frac{\partial \rho_g}{\partial p}$ is real gas compressibility.

Further, the free phase transport equation 4.5 can be expressed in a 'diffusion-like' format in which the combined viscous flow and Knudsen diffusion is characterized by a total effective diffusivity D_{eff} as,

$$\nabla\left(D_{eff}\nabla C\right) = \frac{\partial(\phi C)}{\partial t} - R_m \; ; \quad D_{eff} = D_{k,eff} + D_v \tag{4.6}$$

Where $D_v = \frac{k}{\mu_g c_g}$ denotes the viscous diffusivity. This expression provides a straightforward reference for the comparison between the contributions of viscous flow and Knudsen diffusion mechanisms in bulk gas transport in nanopores using diffusivities.

For sorbed phase transport, surface diffusion flux is given by,

$$J_s = -D_s \nabla C_s \tag{4.7}$$

where D_s is the surface diffusion coefficient, C_s is the concentration of the sorbed phase in mass per unit solid volume.

The governing transport equation for sorbed gas can be written in a form similar to 4.6,

$$\nabla[(1-\phi)D_s \nabla C_s] = \frac{\partial[(1-\phi)C_s]}{\partial t} + R_m \tag{4.8}$$

where $(1-\phi)$ is the non-porous fraction of the domain, and also represents the fractional cross-sectional area of sorbed phase since the solid volume is used to represent the sorbed concentration (Do 1998).

In equations 4.6 and 4.8, the second term on the right-hand-side (R_m) represents the mass transfer rate between the free phase and sorbed phase; this term is due to non-equilibrium adsorption conditions and is expressed in terms of kinetic models of sorption discussed in the next section.

4.2.2.2 Sorption Kinetics

Experimental studies have shown that the assumption of equilibrium adsorption for gas transport in porous media holds true only during rapid desorption and if there is significant diffusivity of the adsorbed-phase (Carman and Raal 1951; Do and Wang 1998; Siemons, Wolf, and Bruining 2007).

Lagergren's model (1898) originally derived for liquid-solid systems is usually recognized as the first equation that calculates adsorption rate under nonequilibrium conditions. The so-called Lagergren equation can be expressed in terms of concentration as,

$$\frac{dC_s}{dt} = k_L(C_e - C_s) \tag{4.9}$$

where C_e is the adsorbed phase concentration at equilibrium; C_s is the adsorbed phase concentration at a given transient intermediate state; and k_L is the adsorption constant.

Equation 4.9 is a first-order rate equation that is commonly referred to as the *linear* kinetic sorption model (Fathi and Akkutlu 2009) because sorption rate has a linear relationship with concentration C_s.

Langmuir kinetics has been widely applied to describe adsorption at solid-liquid interfaces (Li et al.,1994; Liu and Shen, 2008). It describes nonequilibrium sorption rate in terms of monolayer fractional coverage (θ) as the difference between adsorption rate ($r_a = k_a C(1-\theta)$ and desorption rate ($r_d = k_d\theta$),

$$\frac{d\theta}{dt} = r_a - r_d = k_a C(1-\theta) - k_d\theta \tag{4.10}$$

where and k_a and k_d are adsorption and desorption rate constants, respectively; and θ is the ratio of sorbed phase concentration at any time (C_s) to its maximum value (C_{ms}) as (Do, 1998),

$$\theta = \frac{C_s}{C_{ms}} \tag{4.11}$$

Combining equations 4.10 and 4.11, we can rewrite the nonequilibrium sorption rate in the mass rate form as,

$$r_s = [k_a C(C_{ms} - C_s) - k_d C_s] \tag{4.12}$$

Equation 4.12 is also called *nonlinear* kinetic model of sorption (Fathi and Akkutlu 2012), and will be used in this work considering its better consistency with experimental observations (Carman and Raal, 1951; Do and Wang, 1998; Siemons et al., 2007).

Invoking the principle of mass conservation, and based on representing sorbed phase in terms of solid volume, equation 4.12 is further rewritten for the porous medium as a whole,

$$R_m = (1-\phi)[k_a C(C_{ms} - C_s) - k_d C_s] = (1-\phi)[KC(C_{ms} - C_s) - C_s] \tag{4.13}$$

where R_m is the mass transfer rate between free and sorbed phases (RHS in equations 4.6 and 4.8); and $K = k_a/k_d$ is commonly referred to as the *equilibrium constant of adsorption*.

4.2.2.3 Concentration-dependent Surface Diffusivity

Carman and Raal (1951)'s experimental results have shown that surface diffusivity increases rapidly with loading before complete monolayer coverage. Ash et al. (1963) later found the surface diffusivity drops after the monolayer layer is exceeded and increases again during capillary condensation.

Based on our assumption of monolayer sorption, for the period prior to monolayer coverage we use the correlation for concentration dependency of surface diffusivity from the famous hopping model of surface diffusion (HIO model) of Higashi et al. (1963),

$$D_s = D_s^0 \frac{1}{1-\theta} \tag{4.14}$$

where θ is the surface fractional coverage defined in equation 4.11, and D_s^0 is the surface diffusivity at zero coverage that can be expressed as,

$$D_s^0 = D_{s\infty} \exp\left(-\frac{E_s}{RT}\right) \tag{4.15}$$

where E_s is the energy of activation needed for a hop and R is the Boltzmann constant.

Equations 4.14–4.15 show that under the assumptions of this study (isothermal, homogeneous porous media, monolayer sorption), D_s^0 is a constant value and thus D_s is only dependent on sorbed phase concentration. Combining equations 4.14 and 4.11, the final expression of surface diffusion coefficient to be used in the sorbed phase transport equation (4.8) is written as,

$$D_s = D_s^0 \frac{C_{ms}}{C_{ms} - C_s} \tag{4.16}$$

4.2.2.4 Model Initialization

The governing equations were solved using a commercial finite-element simulator (COMSOL Multiphysics®). The porous medium was approximated as a 2D circular disc of radius r = 6mm.

Initial conditions for the system of PDEs are,

$$C(r, t = 0) = C_{in}$$

$$C_s(r, t = 0) = 0$$

At the outer boundary ($r = r_b$ = 6mm), prescribed free gas concentration (density) for equation 4.6 was calculated from reported annular-space pressure shown in Figure 26(left). Pressure was mapped to density using an Equation of State proposed for Xenon by Beattie et al. (1951),

$$C(r - r_b, t) = \rho_g\big(p_b(t)\big)$$

Sorbed phase concentration at boundary r_b was assumed zero i.e. there is negligible sorption at the interface of the sample exposed to annular space,

$$C_s(r = r_b, t) = 0$$

The experimental data used for history matching between simulation and experiment were the propagation profiles of the total fluid density Figure 26(right). These were calculated from the reported phase concentrations from the simulator as the weight-averaged value between bulk and sorbed phases,

$$\rho_t = \phi C + (1 - \phi) C_s$$

The parameters used for history matching were diffusion coefficients (D_{eff} and D_s) that control the flux, and sorption rate coefficients (k_d and K) and maximum sorbed gas concentration (C_{ms}) that control the sorption rates. Porosity(ϕ) was considered constant and uniform, and the helium porosimetry derived value of 7% for this particular sample was applied. The initial estimates for parameter variables were obtained from literature although they were adjusted manually in order to achieve the best possible match. It is relevant to note here that although D_{eff}, in principle, incorporates the advective component of transport D_v, the latter is neither explicitly measured nor estimated from the model. However, if D_v were independently known, the model could be used to evaluate the relative contributions of the advective and diffusive components. However, in this case, this was not possible given that experimental data for D_v was not available.

4.3 Results and Discussion

The goal of history matching was to aid in the development and refinement of the model, and add physical complexity as needed in order to achieve a satisfactory match with the measured data. Some early versions of the model included explicit volumetric modeling of free-gas and adsorbed gas; linear kinetic model of sorption; non-linear kinetic model of sorption with constant surface diffusion etc. The first priority in model development was to qualitatively recreate the 'growing peaks' of gas density near the sample outer radius. This was achieved with the non-linear sorption model with constant surface diffusivity (Figure 28 to Figure 30). The next step was to quantitatively improve the match, which was achieved by incorporating concentration-dependent surface diffusivity in the model. The result of these two versions with non-linear sorption kinetics are discussed in this section. Since additional datasets were not available, blind predictions to validate the model on independent data was not possible.

Figure 28 to Figure 30 present the results from the first history matching attempt, in which *constant* surface diffusivity (D_s) was assumed. Figure 28 provides a qualitative demonstration of simulated ρ_t distribution evolution propagating into the sample as a radial front. Figure 29 shows detailed matches against density propagation profiles along the *r* direction. It can be seen that

the numerical model captures the growing peaks near the outer boundary observed from experimental data, which verifies the effect of sorption kinetics. Parameter estimation based on history matching is provided in Table 1. Based on the match results of density profiles shown in Figure 29, there is an indication that total gas transport behavior is influenced by nonlinear effects. This observation is based on the large discrepancies in the matches at later time steps (38, 48 and 58 hr). Figure 30 indicates that nonlinear surface diffusivity might be an important factor in explaining the discrepancies. This is because based on the comparison between free phase and sorbed phase densities, shown in Figure 30, in-situ conditions appear to be mainly a function of sorbed phase surface density.

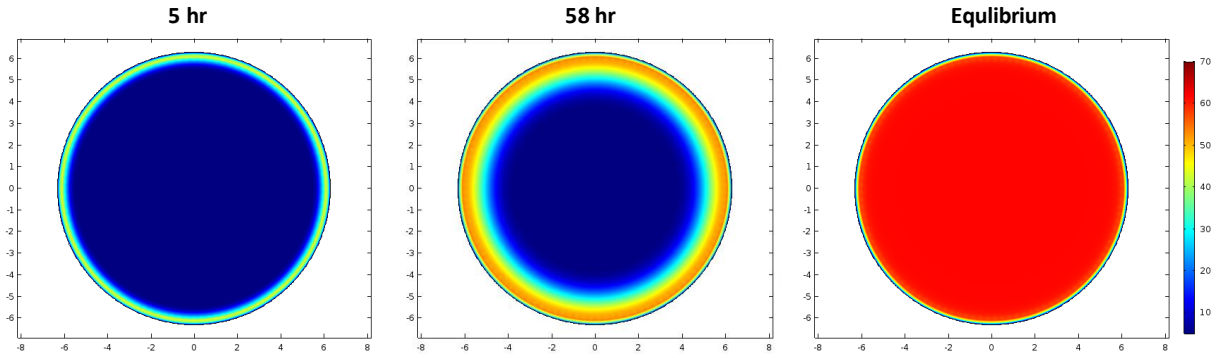

Figure 28: Total density maps showing propagation of xenon gas from the perimeter into the sample over time

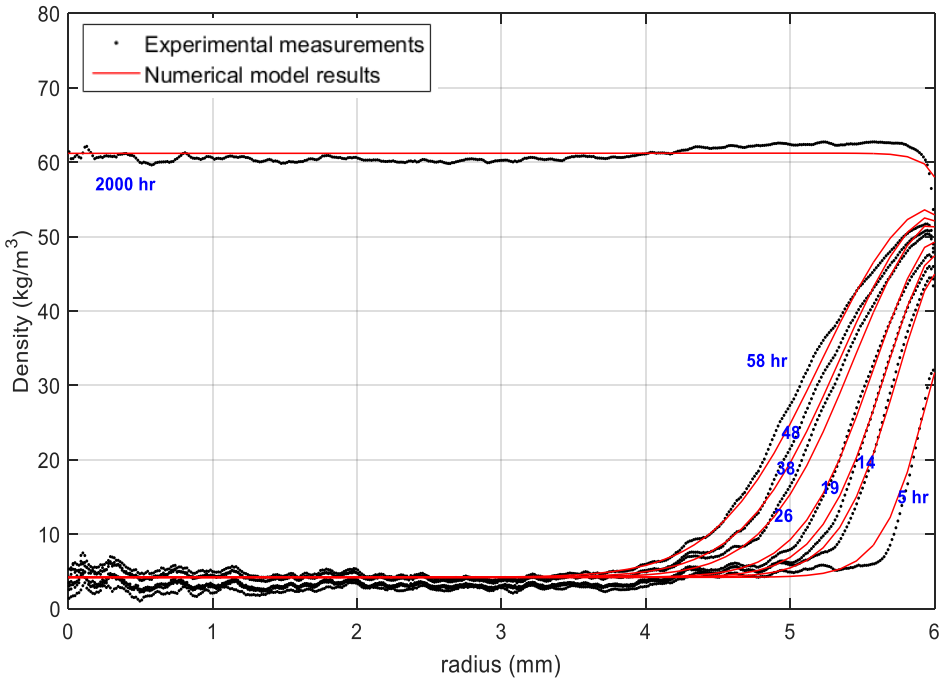

Figure 29: Matching results between numerical model and experimental data with *constant* surface diffusivity

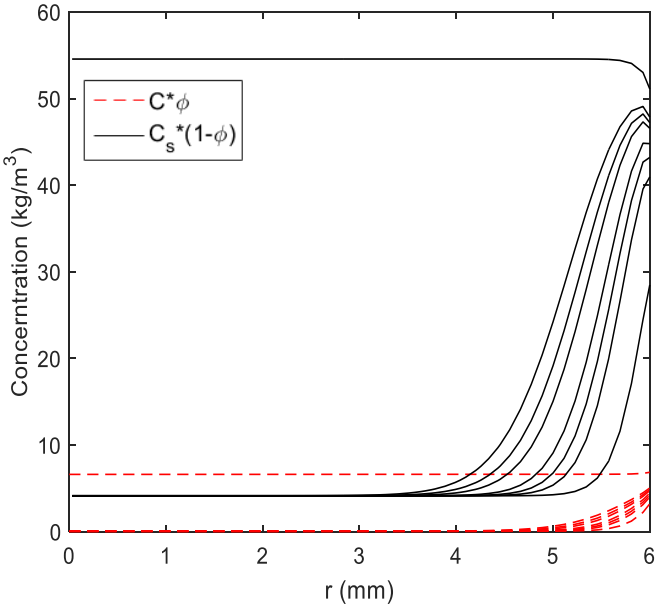

Figure 30: Simulated phase concentrations based on *constan*t surface diffusivity

Table 6: Parameter estimation based on *constant* surface diffusivity model

D_{eff}, cm^2/s	D_s, cm^2/s	C_{ms}, kg/m^3	K (m^3/kg)	k_d (1/s)
1.26×10^{-8}	1.25×10^{-8}	65	0.098	9.2×10^{-6}

Based on these observations, concentration-dependent surface diffusivity was added to the model along with the HIO equation (4.16). History matching results are shown in Figure 31. Comparisons between Figure 29 and Figure 31 shows clear improvement when nonlinear surface diffusion is considered. Parameter estimations are provided in Table 2. The surface diffusivity evolution is plotted in Figure 32(B), indicating that the constant surface diffusivity estimation given by Table 1 is an averaged value of the early-time evolution history of D_s. Comparing the rest of the estimations in Table 1 and 2, most of the parameters are extremely close; the slight difference between maximum sorbed concentration (C_{ms}) is because it is related to surface diffusivity calculation (equation 4.16) and thus must be re-adjusted with D_s.

In this example, estimated diffusion coefficients (D_{eff} and D_s) as well as desorption rate coefficient (k_f) are all found to be close to literature data obtained based on theoretical models or experimental measurements for nano-scale porous media (Karacan, 2003; Fathi and Akkutlu, 2012; Wu et al., 2016). The only exception is that the maximum sorbed phase concentration (C_{ms}) which appears to be anomalously small. It is because sorbed phase concentration C_s used in the numerical model is an 'effective' or 'equivalent' concentration distributed evenly in the solid volume, rather than the actual density of the monolayer of adsorbed molecules.

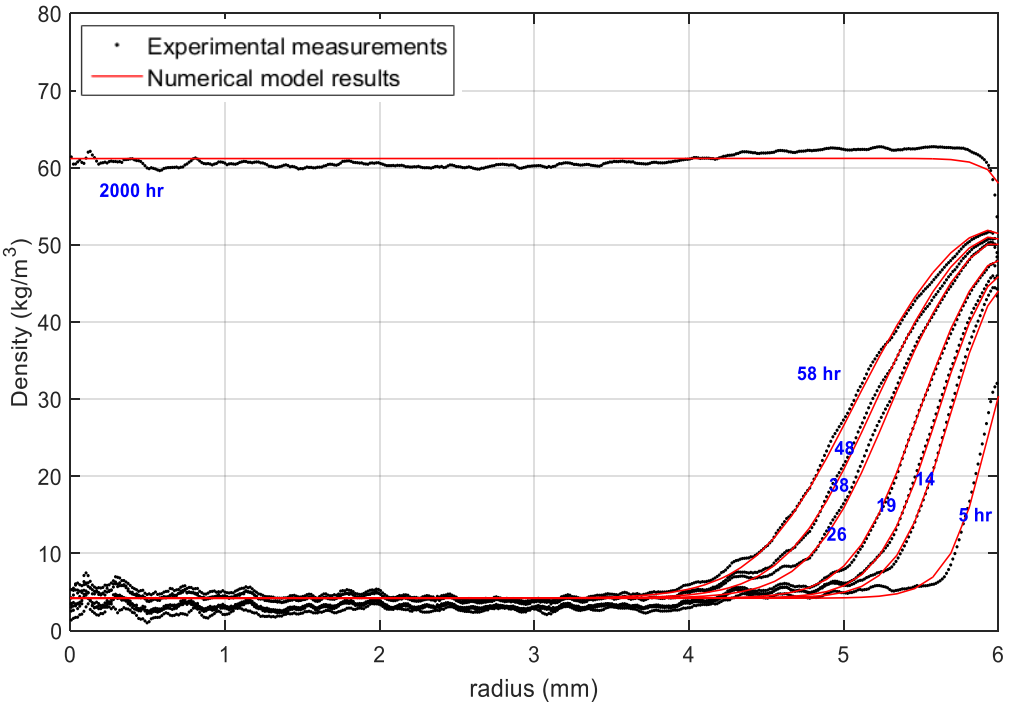

Figure 31: Matching results between numerical model and experimental data with *concentration-dependent* surface diffusivity

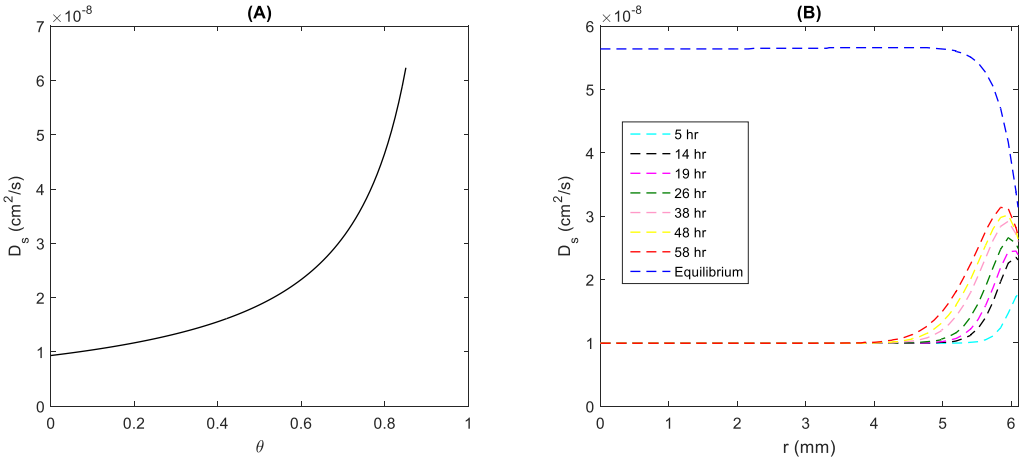

Figure 32: (A) surface diffusivity as function of coverage (HIO model); (B) surface diffusivity profiles from simulation results

Table 7: Parameter estimation based on *concertation-dependent* surface diffusivity model

D_{eff}, cm^2/s	D^0_s, cm^2/s	C_{ms}, kg/m^3	K (m^3/kg)	k_d (1/s)
1.26×10^{-8}	9.35×10^{-9}	74	0.095	9.2×10^{-6}

Although this model does not account for multilayer adsorption it satisfactorily reproduces the qualitative and quantitative trends observed in the measured data, and is therefore a good first step in representing the experiment. This is likely because the model currently only requires estimates of the maximum adsorbed content which is represented as C_{ms}. We could not currently find any way to independently estimate this parameter, and it has been used as a model tuning parameter. The next step in improving the model would be to incorporate fabric characterization data such as pore size distribution and surface area to further constrain and refine the model. This may require the introduction of added physical complexity such as an improved description of gas densification, PVT properties, or multilayer sorption mechanism. Independent data from other shale samples and further testing and validation of the model is also recommended. Such future experiments should also be designed to independently estimate static parameters such as C_{ms} in order to simplify the history matching process for dynamic data.

4.4 Conclusions

In this chapter, we discussed the formulation of a diffusion and non-equilibrium sorption kinetic based numerical model to capture bulk and microscale transport in shales. The model was validated against experimental data in the form of dynamic density profiles of in-situ pore fluid acquired on an organic-rich, nanoporous, ultra-tight Marcellus shale sample. The following inferences can be drawn based on these modeling efforts,

1) Gas transport in shale and can be modeled by accounting for effects of gas diffusion and gas adsorption/desorption.

2) Adsorption/desorption is a non-equilibrium process during fluid transport and can be effectively represented by the kinetic model of sorption.

3) Under current experimental conditions (room temperature, low pressure), surface diffusion is the dominant mechanism affecting transport and in-situ fluid conditions.

4) Surface diffusivity is shown to be concentration dependent and sorbed gas transport is thus a nonlinear phenomenon.

Concluding Remarks

The focus of this research project was to study the fundamentals of gas storage in shales and the implication of complex storage mechanisms on transport. Material was sourced from four different North American shales – the Marcellus, Haynesville, Mancos, and Bakken, giving us a compositionally and texturally diverse set of specimens for experiments. The storage behavior of several noble gases and hydrocarbon gases were measured, with helium being representative of a non-sorbing ideal gas. Results presented in chapter 1 indicated that gas densification, likely due to sorption, plays a significant role in overall gas storage at laboratory conditions. In chapter 2 we explored the storage data more closely along with additional experiments to find out whether the common representation of all excess gas storage as surface adsorption was indeed true, and considered alternatives like capillary condensation, induced-supercriticality, and phase behavior differences. This analysis revealed some anomalies in the data that may be better explained by non-adsorption fluid behavior. Detailed sample characterization presented in chapter 3 helped better contextualize the storage and fluid behaviors observed in chapters 1 and 2. Surface area data revealed that excess gas storage could be described as a multi-layer adsorption process, which is plausible, albeit conceptually tenuous for supercritical fluids. Statistical and image-based spatial correlations revealed that mineralogy is not correlated with storage behavior and organic content is weakly correlated with gas storage. However, pore sizes and surface area were found to be good indicators of storage. A numerical model was developed and presented in Chapter 4 that accounted for the often-ignored phenomena of diffusion, and adsorption-desorption kinetics. This model was shown to satisfactorily describe gas transport in the ultra-tight Marcellus Shale sample. This was the sample with the highest pore surface area and sorption for all gases. Perhaps unsurprisingly, the model revealed that surface diffusion was the predominant mechanism governing fluid transport in this sample.

The overall conclusion that emerges from this research is that free-gas constitutes a small portion of gas storage in nanoporous shales, and that gas storage behavior is much more complex in tight nanoporous structures than in conventional reservoir rocks. Shales with predominantly large

macropores behave more like conventional rocks despite high clay content. Gas densification, likely into adsorbed gas, is a very important storage mechanism that needs to be considered both for Gas-in-Place estimations, as well as for prediction of transport properties in nanoporous shales. Further research into alternative theories on the mechanism of gas densification such as induced-supercriticality, and of fluid behavior in nanoporous environments is also warranted.

Recommendations for Future Work

The results of this study indicate that when single component gas is injected into shales, far more can be stored than would be expected if the pore volume were to fill up with only free-gas. This indicates a densification of the gas injected into the pore space. The mechanism of this densification needs to be more carefully studied so that models of storage can be made more physically correct, which is important for accurate calculations of GIP and for predictions of transport behaviors. In particular, the distinction between densification due to surface adsorption vs. bulk phenomena such as induced supercriticality, or capillary condensation will greatly affect our expectations of storage and transport under various conditions of pressure, temperature, fluid type, and rock type and texture. It is possible that the observed densification is due simultaneously due to multiple mechanisms including sorption, and other mechanisms stemming from the confinement of fluid within nanopores. Materials with uniform and homogenous composition and a uniform nanopore sized pores would be ideal for isolating the contributions of competing densification mechanisms. Experiments with different types of gases, as well as at higher pressure-temperature conditions would also be useful to delineate the extent of densification at a broader set of conditions than those performed in this study.

The results of this study also indicate the lack of correlation between the observed densification and rock mineralogy. This contradicts our primary expectation that densification is due largely to adsorption, given that adsorption is a fluid-surface interaction effect and thus likely to be sensitive to solid-fluid compositions. The correlation between rock surface area as storage capacity has been clearly demonstrated in this study which warrants a deeper investigation into the role of nano-pore topology on adsorption. Molecular modeling studies or other experimental studies on controlled pore-size and composition materials could shed light on whether adsorption could be enhanced or depressed based on pore geometry and overall topology of the pore network. More detailed, composition specific characterization in conjunction with gas storage measurements could be used to evaluate the hypothesis that samples with mature

organic matter, and by extension - with more nanoporosity, would show higher gas uptake than samples with higher content of organic matter but one that is immature.

The fluid transport model developed in this work was a first step towards representing via a conceptual and numerical model the never-before-observed experimental behavior of temporally increasing near-boundary concentration of gas injected radially into a shale core. Although the model developed matches the experimental data well, independent experimental data should be acquired to validate the model. Furthermore, such future data should incorporate additional information such as pore size distributions, and independently measure maximum ultimate storage capacities. This will further constrain the model and help identify additional physical phenomena that may be missing from the current model.

References

- Alnoaimi, K. R., and A. R. Kovscek. 2013. “Experimental and Numerical Analysis of Gas Transport in Shale Including the Role of Sorption.” In . Society of Petroleum Engineers. https://doi.org/10.2118/166375-MS.
- Ambrose, Raymond Joseph, Robert Chad Hartman, Mery Diaz Campos, I. Yucel Akkutlu, and Carl Sondergeld. 2010. “New Pore-Scale Considerations for Shale Gas in Place Calculations.” In . Society of Petroleum Engineers. https://doi.org/10.2118/131772-MS.
- Ash R., Barrer Richard Maling, and Pope C. G. 1963. “Flow of Adsorbable Gases and Vapours in a Microporous Medium, I. Single Sorbates.” *Proceedings of the Royal Society of London. Series A. Mathematical and Physical Sciences* 271 (1344): 1–18. https://doi.org/10.1098/rspa.1963.0001.
- Beattie, James A., Roland J. Barriault, and James S. Brierley. 1951. “The Compressibility of Gaseous Xenon. I. An Equation of State for Xenon and the Weight of a Liter of Xenon.” *The Journal of Chemical Physics* 19 (10): 1219–21. https://doi.org/10.1063/1.1747999.
- Busch, Andreas, Sascha Alles, Yves Gensterblum, Dirk Prinz, David N. Dewhurst, Mark D. Raven, Helge Stanjek, and Bernhard M. Krooss. 2008. “Carbon Dioxide Storage Potential of Shales.” *International Journal of Greenhouse Gas Control* 2 (3): 297–308. https://doi.org/10.1016/j.ijggc.2008.03.003.
- Caravella, Alessio. 2016. “Dusty-Gas Model (DGM).” *Encyclopedia of Membranes*, 604–5. https://doi.org/10.1007/978-3-662-44324-8_1737.
- Carman, P. C., and F. A. Raal. 1951. “Diffusion and Flow of Gases and Vapours through Micropores III. Surface Diffusion Coefficients and Activation Energies.” *Proceedings of the Royal Society of London. Series A. Mathematical and Physical Sciences* 209 (1096): 38–58. https://doi.org/10.1098/rspa.1951.0186.
- Chalmers, Gareth R., R. Marc Bustin, and Ian M. Power. 2012. “Characterization of Gas Shale Pore Systems by Porosimetry, Pycnometry, Surface Area, and Field Emission Scanning Electron Microscopy/Transmission Electron Microscopy Image Analyses:

Examples from the Barnett, Woodford, Haynesville, Marcellus, and Doig Units." *AAPG Bulletin* 96 (6): 1099–1119. https://doi.org/10.1306/10171111052.

- Chen, Li, Lei Zhang, Qinjun Kang, Hari S. Viswanathan, Jun Yao, and Wenquan Tao. 2015. "Nanoscale Simulation of Shale Transport Properties Using the Lattice Boltzmann Method: Permeability and Diffusivity." *Scientific Reports* 5 (January): 8089. https://doi.org/10.1038/srep08089.
- Clarkson, C. R., B. Haghshenas, A. Ghanizadeh, F. Qanbari, J. D. Williams-Kovacs, N. Riazi, C. Debuhr, and H. J. Deglint. 2016. "Nanopores to Megafractures: Current Challenges and Methods for Shale Gas Reservoir and Hydraulic Fracture Characterization." *Journal of Natural Gas Science and Engineering* 31 (April): 612–57.
- Cole, D. R., A. A. Chialvo, G. Rother, L. Vlcek, and P. T. Cummings. 2010. "Supercritical Fluid Behavior at Nanoscale Interfaces: Implications for CO2 Sequestration in Geologic Formations." *Philosophical Magazine* 90 (17–18): 2339–63. https://doi.org/10.1080/14786430903559458.
- Cychosz, Katie A., and Matthias Thommes. 2018. "Progress in the Physisorption Characterization of Nanoporous Gas Storage Materials." *Engineering* 4 (4): 559–66. https://doi.org/10.1016/j.eng.2018.06.001.
- Do, D. D. 1998. *Adsorption Analysis: Equilibria And Kinetics*. Series on Chemical Engineering. London: Imperial College Press. http://ezaccess.libraries.psu.edu/login?url=http://search.ebscohost.com/login.aspx?direct=true&db=nlebk&AN=83649&site=ehost-live&scope=site.
- Do, D. D, and K Wang. 1998. "A New Model for the Description of Adsorption Kinetics in Heterogeneous Activated Carbon." *Carbon* 36 (10): 1539–54. https://doi.org/10.1016/S0008-6223(98)00145-6.
- Ertekin, T., and W. Sung. 1989. "Pressure Transient Analysis of Coal Seams in the Presence of Multi-Mechanistic Flow and Sorption Phenomena." In . Society of Petroleum Engineers. https://doi.org/10.2118/19102-MS.

- Ertekin, Turgay, Gregory A. King, and Fred C. Schwerer. 1986. “Dynamic Gas Slippage: A Unique Dual-Mechanism Approach to the Flow of Gas in Tight Formations.” *SPE Formation Evaluation* 1 (01): 43–52. https://doi.org/10.2118/12045-PA.
- Fathi, Ebrahim, and I. Yücel Akkutlu. 2009. “Matrix Heterogeneity Effects on Gas Transport and Adsorption in Coalbed and Shale Gas Reservoirs.” *Transport in Porous Media* 80 (2): 281. https://doi.org/10.1007/s11242-009-9359-4.
- Fathi, Ebrahim, and I. Yucel Akkutlu. 2012. “Mass Transport of Adsorbed-Phase in Stochastic Porous Medium with Fluctuating Porosity Field and Nonlinear Gas Adsorption Kinetics.” *Transport in Porous Media* 91 (1): 5–33. https://doi.org/10.1007/s11242-011-9830-x.
- Gensterblum, Yves, Amin Ghanizadeh, Robert J. Cuss, Alexandra Amann-Hildenbrand, Bernhard M. Krooss, Christopher R. Clarkson, John F. Harrington, and Mark D. Zoback. 2015. “Gas Transport and Storage Capacity in Shale Gas Reservoirs – A Review. Part A: Transport Processes.” *Journal of Unconventional Oil and Gas Resources* 12 (December): 87–122. https://doi.org/10.1016/j.juogr.2015.08.001.
- Ghosh, Kanka, and C. V. Krishnamurthy. 2018. “Structural Behavior of Supercritical Fluids under Confinement.” *Physical Review E* 97 (1): 012131. https://doi.org/10.1103/PhysRevE.97.012131.
- Gray, Peter G., and Duong D. Do. 1992. “A Graphical Method for Determining Pore and Surface Diffusivities in Adsorption Systems.” *Industrial & Engineering Chemistry Research* 31 (4): 1176–82. https://doi.org/10.1021/ie00004a030.
- Heller, Robert, and Mark Zoback. 2014. “Adsorption of Methane and Carbon Dioxide on Gas Shale and Pure Mineral Samples.” *Journal of Unconventional Oil and Gas Resources* 8 (Supplement C): 14–24. https://doi.org/10.1016/j.juogr.2014.06.001.
- Herdes, Carmelo, Camille Petit, Andres Mejía, and Erich A. Müller. 2018. “Combined Experimental, Theoretical, and Molecular Simulation Approach for the Description of the Fluid-Phase Behavior of Hydrocarbon Mixtures within Shale Rocks.” *Energy & Fuels* 32 (5): 5750–62. https://doi.org/10.1021/acs.energyfuels.8b00200.

- Higashi, K., H. Ito, and J. Oishi. 1963. “SURFACE DIFFUSION PHENOMENA IN GASEOUS DIFFUSION. I. SURFACE DIFFUSION OF PURE GAS.” *Nippon Genshiryoku Gakkaishi (Japan)* Vol: 5 (October). https://www.osti.gov/biblio/4129274-surface-diffusion-phenomena-gaseous-diffusion-surface-diffusion-pure-gas.
- Hubbert, M. K. 1957. “Darcy’s Law and the Field Equations of the Flow of Underground Fluids.” *International Association of Scientific Hydrology. Bulletin* 2 (1): 23–59. https://doi.org/10.1080/02626665709493062.
- Hwang, Sun-Tak, and Karl Kammermeyer. 1966. “Surface Diffusion in Microporous Media.” *The Canadian Journal of Chemical Engineering* 44 (2): 82–89. https://doi.org/10.1002/cjce.5450440206.
- Javadpour, F. 2009. “Nanopores and Apparent Permeability of Gas Flow in Mudrocks (Shales and Siltstone).” *Journal of Canadian Petroleum Technology* 48 (08): 16–21. https://doi.org/10.2118/09-08-16-DA.
- Jin, Zhehui, and Abbas Firoozabadi. 2016. “Thermodynamic Modeling of Phase Behavior in Shale Media.” *SPE Journal* 21 (01): 190–207. https://doi.org/10.2118/176015-PA.
- Kamari, Arash, Lei Li, and James J. Sheng. 2018. “Effects of Rock Pore Sizes on the PVT Properties of Oil and Gas-Condensates in Shale and Tight Reservoirs.” *Petroleum* 4 (2): 148–57. https://doi.org/10.1016/j.petlm.2017.06.002.
- Kang, S. M., E. Fathi, R. J. Ambrose, I. Y. Akkutlu, and R. F. Sigal. 2011. “Carbon Dioxide Storage Capacity of Organic-Rich Shales.” *Spe Journal* 16 (4): 842–55.
- Karacan, Özgen C. 2003. “An Effective Method for Resolving Spatial Distribution of Adsorption Kinetics in Heterogeneous Porous Media: Application for Carbon Dioxide Sequestration in Coal.” *Chemical Engineering Science* 58 (20): 4681–93. https://doi.org/10.1016/j.ces.2003.05.002.
- King, George Everette. 2010. “Thirty Years of Gas Shale Fracturing: What Have We Learned?” In . Society of Petroleum Engineers. https://doi.org/10.2118/133456-MS.
- Lagergren, S. 1898. “Zur Theorie Der Sogenannten Adsorption Geloster Stoffe.” *Kungliga Svenska Vetenskapsakademiens. Handlingar* 24: 1–39.

- Lane, H. S., A. T. Watson, and D. E. Lancaster. 1989. “Identifying and Estimating Desorption From Devonian Shale Gas Production Data.” In . Society of Petroleum Engineers. https://doi.org/10.2118/19794-MS.
- Lu, Xc, Fc Li, and At Watson. 1995. “Adsorption Studies of Natural-Gas Storage in Devonian Shales.” *Spe Formation Evaluation* 10 (2): 109–13.
- Luo, Sheng, Jodie L. Lutkenhaus, and Hadi Nasrabadi. 2016. “Confinement-Induced Supercriticality and Phase Equilibria of Hydrocarbons in Nanopores.” *Langmuir* 32 (44): 11506–13. https://doi.org/10.1021/acs.langmuir.6b03177.
- Mason, E. A., and A. P. Malinauskas. 1983. *Gas Transport in Porous Media: The Dusty-Gas Model*. Elsevier.
- Morishige, K., H. Fujii, M. Uga, and D. Kinukawa. 1997. “Capillary Critical Point of Argon, Nitrogen, Oxygen, Ethylene, and Carbon Dioxide in MCM-41.” *Langmuir* 13 (13): 3494–98. https://doi.org/10.1021/la970079u.
- Nojabaei, Bahareh, Russell T. Johns, and Lifu Chu. 2013. “Effect of Capillary Pressure on Phase Behavior in Tight Rocks and Shales.” *SPE Reservoir Evaluation & Engineering* 16 (03): 281–89. https://doi.org/10.2118/159258-PA.
- Pan, Zhejun, and Luke D. Connell. 2015. “Reservoir Simulation of Free and Adsorbed Gas Production from Shale.” *Journal of Natural Gas Science and Engineering* 22 (January): 359–70. https://doi.org/10.1016/j.jngse.2014.12.013.
- Parsa, E., X. Yin, and E. Ozkan. 2015. “Direct Observation of the Impact of Nanopore Confinement on Petroleum Gas Condensation.” In . Society of Petroleum Engineers. https://doi.org/10.2118/175118-MS.
- Pathak, Manas, Hyukmin Kweon, Palash Panja, Raul Velasco, and Milind D. Deo. 2017. “Suppression in the Bubble Points of Oils in Shales Combined Effect of Presence of Organic Matter and Confinement.” In . Society of Petroleum Engineers. https://doi.org/10.2118/185080-MS.
- Perez, Felipe, and Deepak Devegowda. 2017. “Estimation of Adsorbed-Phase Density of Methane in Realistic Overmature Kerogen Models Using Molecular Simulations for

Accurate Gas in Place Calculations." *Journal of Natural Gas Science and Engineering* 46 (Supplement C): 865–72. https://doi.org/10.1016/j.jngse.2017.08.008.

- Ross, Daniel J. K., and R. Marc Bustin. 2009. "The Importance of Shale Composition and Pore Structure upon Gas Storage Potential of Shale Gas Reservoirs." *Marine and Petroleum Geology* 26 (6): 916–27. https://doi.org/10.1016/j.marpetgeo.2008.06.004.
- Rouquerol, J., D. Avnir, Cw Fairbridge, Dh Everett, Jh Haynes, N. Pernicone, Jdf Ramsay, Ksw Sing, and Kk Unger. 1994. "Recommendations for the Characterization of Porous Solids." *Pure and Applied Chemistry* 66 (8): 1739–58. https://doi.org/10.1351/pac199466081739.
- Rouquerol, Jean, Gino V. Baron, Renaud Denoyel, Herbert Giesche, Johan Groen, Peter Klobes, Pierre Levitz, et al. 2012. "The Characterization of Macroporous Solids: An Overview of the Methodology." *Microporous and Mesoporous Materials*, Special Issue: Characterisation of Porous Solids IX, 154 (May): 2–6. https://doi.org/10.1016/j.micromeso.2011.09.031.
- Schettler, P. D. Jr, and C. R. Parmely. 1991. "Contributions to Total Storage Capacity in Devonian Shales." In . Society of Petroleum Engineers. https://doi.org/10.2118/23422-MS.
- Seales, Maxian B., Turgay Ertekin, and John Yilin Wang. 2017. "Recovery Efficiency in Hydraulically Fractured Shale Gas Reservoirs." *Journal of Energy Resources Technology-Transactions of the Asme* 139 (4): 042901. https://doi.org/10.1115/1.4036043.
- Shen, W., L. Zheng, C. M. Oldenburg, A. Cihan, J. Wan, and T. K. Tokunaga. 2018. "Methane Diffusion and Adsorption in Shale Rocks: A Numerical Study Using the Dusty Gas Model in TOUGH2/EOS7C-ECBM" 123 (3): 521–31. https://doi.org/10.1007/s11242-017-0985-y.
- Siemons, Nikolai, Karl-Heinz A. A. Wolf, and Johannes Bruining. 2007. "Interpretation of Carbon Dioxide Diffusion Behavior in Coals." *International Journal of Coal Geology* 72 (3): 315–24. https://doi.org/10.1016/j.coal.2007.04.004.
- Sing, K. S. W., D. H. Everett, R. A. W. Haul, L. Moscou, R. A. Pierotti, J. Rouquérol, and T. Siemieniewska. 1985. "Reporting Physisorption Data for Gas/Solid Systems With Special

Reference to the Determination of Surface Area and Porosity." *Pure and Applied Chemistry* 57 (603). https://doi.org/10.1351/pac198557040603.

- Sing, K. S. W., and Ruth T. Williams. 2004. "Physisorption Hysteresis Loops and the Characterization of Nanoporous Materials." *Adsorption Science & Technology* 22 (10): 773–82. https://doi.org/10.1260/0263617053499032.
- Sun, Jianmeng, Xu Dong, Jinjie Wang, Douglas R. Schmitt, Chunlu Xu, Tariq Mohammed, and Dewen Chen. 2016. "Measurement of Total Porosity for Gas Shales by Gas Injection Porosimetry (GIP) Method." *Fuel* 186 (December): 694–707. https://doi.org/10.1016/j.fuel.2016.09.010.
- Thimons, Edward D., and Fred N. Kissell. 1973. "Diffusion of Methane through Coal." *Fuel* 52 (4): 274–80. https://doi.org/10.1016/0016-2361(73)90057-4.
- Thommes, Matthias, and Gerhard H. Findenegg. 1994. "Pore Condensation and Critical-Point Shift of a Fluid in Controlled-Pore Glass." *Langmuir* 10 (11): 4270–77. https://doi.org/10.1021/la00023a058.
- Vega, Bolivia, Abhishek Dutta, and Anthony R. Kovscek. 2013. "CT Imaging of Low-Permeability, Dual-Porosity Systems Using High X-Ray Contrast Gas." *Transport in Porous Media* 101 (1): 81–97. https://doi.org/10.1007/s11242-013-0232-0.
- Wang, Junjian, Li Chen, Qinjun Kang, and Sheik S. Rahman. 2016. "Apparent Permeability Prediction of Organic Shale with Generalized Lattice Boltzmann Model Considering Surface Diffusion Effect." *Fuel* 181 (October): 478–90. https://doi.org/10.1016/j.fuel.2016.05.032.
- Wang, Lei, Elham Parsa, Yuefeng Gao, Jeong Tae Ok, Keith Neeves, Xiaolong Yin, and Erdal Ozkan. 2014. "Experimental Study and Modeling of the Effect of Nanoconfinement on Hydrocarbon Phase Behavior in Unconventional Reservoirs." In . Society of Petroleum Engineers. https://doi.org/10.2118/169581-MS.
- Wang, Lei, Shihao Wang, Ronglei Zhang, Cong Wang, Yi Xiong, Xishen Zheng, Shangru Li, Kai Jin, and Zhenhua Rui. 2017. "Review of Multi-Scale and Multi-Physical Simulation

Technologies for Shale and Tight Gas Reservoirs." *Journal of Natural Gas Science and Engineering* 37 (January): 560–78. https://doi.org/10.1016/j.jngse.2016.11.051.

- Wang, Yang, Yanming Zhu, Shimin Liu, and Rui Zhang. 2016. "Pore Characterization and Its Impact on Methane Adsorption Capacity for Organic-Rich Marine Shales." *Fuel* 181 (October): 227–37. https://doi.org/10.1016/j.fuel.2016.04.082.
- Webb, Paul A., and Clyde Orr. 1997. *Analytical Methods in Fine Particle Technology*. Micromeritics Instrument Corporation.
- Wellington, Sl, and Hj Vinegar. 1987. "X-Ray Computerized-Tomography." *Journal of Petroleum Technology* 39 (8): 885–98. https://doi.org/10.2118/16983-PA.
- Wu, Keliu, Xiangfang Li, Chenchen Wang, Wei Yu, and Zhangxin Chen. 2015. "Model for Surface Diffusion of Adsorbed Gas in Nanopores of Shale Gas Reservoirs." *Industrial & Engineering Chemistry Research* 54 (12): 3225–36. https://doi.org/10.1021/ie504030v.
- Xiong, Wei, Luo Zuo, Litao Luo, Zhiming Hu, and Yaxing Cui. 2016. "Methane Adsorption on Shale under High Temperature and High Pressure of Reservoir Condition: Experiments and Supercritical Adsorption Modeling." *Adsorption Science & Technology* 34 (2–3): 193–211. https://doi.org/10.1177/0263617415623425.
- Yang, Yunlai, and Andrew C. Aplin. 2007. "Permeability and Petrophysical Properties of 30 Natural Mudstones." *Journal of Geophysical Research-Solid Earth* 112 (B3): B03206. https://doi.org/10.1029/2005JB004243.

Appendix A: X-ray CT Calibration

For the purposes of this research the CT numbers of a given material was the same as the linear attenuation (μ) of a material,

$$\mu = -\frac{1}{t} \cdot \log_e \left(\frac{I}{I_0}\right) \tag{A.1}$$

where, μ is the linear attenuation coefficient of the material; I is the intensity of transmitted X-rays, I_0 is the intensity of the incident X-rays, t is the sample thickness.

At prevailing experimental X-ray energies, linear attenuation is a function of Compton scatter and the photoelectric effect,

$$\mu = \rho \cdot \left(\alpha \cdot \frac{Z^k}{E^l} + \beta\right) \tag{A.2}$$

Where, Z is material atomic number, E is X-ray energy, $k \approx 3;\ l \approx 3$, α and β are constants.

For a X-ray of constant beam energy, i.e., constant E, equation A.2 can be approximated as,

$$\frac{\mu}{\rho} = a + b * Z^3 \tag{A.3}$$

Where, $a = \beta, b = \frac{\alpha}{E^l}$

Equation A.3 is re-arranged form of equation 2.3.

The coefficients *a* and *b* were calibrated using CT measurements of standard materials at 200keV as shown in Figure 33. The calibrated values were,

$a = 3.7 * 10^{-6}$

$b = 0.024$

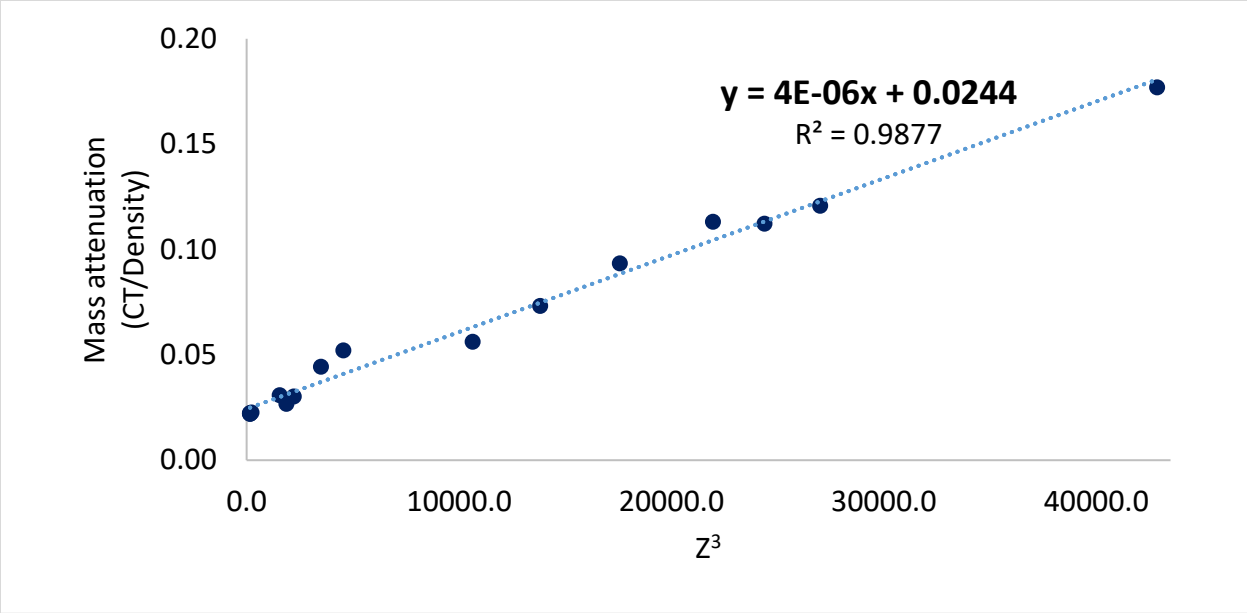

Figure 33: Measured data on standard materials to calibrate equation 2.3

VITA

Nirjhor Chakraborty

Bio
Born: India, June 14, 1991
Professional Profile: https://www.linkedin.com/in/nirjhorchakraborty

Degrees
Bachelor of Technology, 2013 (Petroleum Engineering)
Rajiv Gandhi Institute of Petroleum Technology, Rae Bareli (now Jais), India

Master of Science, 2015 (Petroleum and Natural Gas Engineering)
The Pennsylvania State University

Doctor of Philosophy, 2019 (Energy and Mineral Engineering)
The Pennsylvania State University

Work Experience
Field Intern at Well Stimulation Services, Summer 2012
Oil and Natural Gas Corporation, India

Graduate Assistant (Research and Teaching), January 2014 – May 2019
The Pennsylvania State University

Petrophysicist Intern, Summer 2017 and 2018
BP America

Research Interests
Micro and nano-fluidics, shale gas, high resolution and non-destructive imaging systems, quantitative image analysis, image-based modeling and simulation methods

Awards
- Second Place –SPE International Student Paper Contest - Master's Division, ATCE, Houston 2015
    - First Place – North-Eastern North America Region
- Second Place – Petrobowl, ATCE, Dubai 2016
- Third Place - SPE Student Paper Contest – Ph.D. Division, North-Eastern North America Region, 2018
- Second Place - SPE Student Paper Contest – Ph.D. Division, North-Eastern North America Region, 2019